Titre: Title:	Investigation of the Retinal Biomarkers of Alzheimer's Disease and Atherosclerosis Using Hyperspectral Images
Auteur: Author:	Sayed Mehran Sharafi
Date:	2019
Type:	Mémoire ou thèse / Dissertation or Thesis
Référence: Citation:	Sharafi, S. M. (2019). Investigation of the Retinal Biomarkers of Alzheimer's Disease and Atherosclerosis Using Hyperspectral Images [Thèse de doctorat, Polytechnique Montréal]. PolyPublie. https://publications.polymtl.ca/4041/

URL de PolyPublie: PolyPublie URL:	https://publications.polymtl.ca/4041/
Directeurs de recherche: Advisors:	Frédéric Lesage
Programme: Program:	Génie biomédical

POLYTECHNIQUE MONTRÉAL

affiliée à l'Université de Montréal

Investigation of the Retinal Biomarkers of Alzheimer's Disease and Atherosclerosis Using Hyperspectral Images

SAYED MEHRAN SHARAFI

Institut de génie biomédical

Thèse présentée en vue de l'obtention du diplôme de *Philosophiae Doctor*

Génie biomédical

Août 2019

POLYTECHNIQUE MONTRÉAL

affiliée à l'Université de Montréal

Cette thèse intitulée :

Investigation of the Retinal Biomarkers of Alzheimer's Disease and Atherosclerosis Using Hyperspectral Images

présentée par **Sayed Mehran SHARAFI**

en vue de l'obtention du diplôme de *Philosophiae Doctor*

a été dûment acceptée par le jury d'examen constitué de :

Mathieu DEHAES, président

Frédéric LESAGE, membre et directeur de recherche

Elvire Vaucher, membre

Hervé Lombaert, membre externe

DEDICATION

To my darling son, Amirhassan,

whose affection and companionship has given happiness and hope to me to get things done in a city that is far from our back home.

This dissertation is also dedicated to the memory of my mother,

for her endless love, prayers, and sacrifices for success in my life.

ACKNOWLEDGEMENTS

This thesis was carried out at the Institute of Biomedical Engineering of the department of Electrical Engineering at Polytechnique Montreal, from 2016 to 2019. It was financed by the Consortium Québécois sur la Découverte du Médicament—CQDM and Natural Sciences and Engineering Research Council of Canada —NSERC.

I would like to express my deep gratitude to my research supervisor, Prof. Frédéric Lesage, for providing continued support throughout my PhD study. I am very grateful for his patience, motivation, and immense knowledge. His guidance helped me in all the time of research as well as writing of this thesis. I am grateful to Prof. Lesage for all of the opportunities I was given to conduct my research. I could not have imagined having a better supervisor and mentor for my PhD study. Besides my research supervisor, I would like to thank the rest of my thesis committee: Prof. Mathieu Dehaes, Prof. Elvire Vaucher, and Prof. Hervé Lombaert, for their insightful comments and encouragement.

I am grateful to all down at Optina Diagnostics for providing required resources for the research with a special mention to Dr. Jean-Philippe Sylvestre for his support that helped me improve the quality of the work.

My sincere thanks also go to all professors at Polytechnique Montreal and McGill University who created an amazing space for learning and enriching my knowledge on biomedical engineering with special gratitude to Prof. Nikola Stikov and Prof. Louis Collins.

I am also grateful to the university staffs at Polytechnique Montreal for their support and assistance throughout my PhD study.

I would like to acknowledge my colleagues at Molecular and Optical Imaging Laboratory — LIOM— at Polytechnique Montreal for creating a cordial working environment and helping me along the way.

I am thankful to all of my friends who provided me with moral and emotional support throughout this journey and my life in general.

And finally, last but by no means least, a very special word of thanks goes for my family particularly: my father who helped me in all things great and small, my beloved wife who has been

supportive for me and listened to the woes and joys I felt through the process, my lovely son Amirhassan who is the pride and joy of my life, my dear sisters, Elham, Ala, and Maryam who have always been a major source of support and encouragement, and my sweet niece Bahar and baby nephew Parham whose laughter and playfulness has always enlivened my spirits. I thank God for enlightening my life with your presence. This would not have been possible without your support.

RÉSUMÉ

Le fait que l'œil puisse être visualisé de manière non invasive ouvre des possibilités de mesure de biomarqueurs pour le diagnostic de conditions à long terme. Selon de nombreuses études, plusieurs maladies cardiovasculaires et neurodégénératives telles que la maladie d'Alzheimer (AD) et l'athérosclérose (ATH) se manifestent dans la rétine sous forme de modifications morphologiques pathologiques et / ou vasculaires. Des méthodes d'imagerie oculaire en deux dimensions et des techniques de tomographie par cohérence optique (OCT) en trois dimensions ont été développées pour fournir des descriptions des structures rétiniennes. Cependant, les images acquises par ces techniques permettent principalement de mesurer les caractéristiques spatiales et pas la variance relative de l'intensité des pixels sur différentes longueurs d'onde, de sorte que d'importantes caractéristiques liées aux tissus peuvent encore rester à découvrir.

Dans cette étude, une caméra rétinienne métabolique hyperspectrale (MHRC) a été utilisée pour permettre l'acquisition d'une série d'images rétiniennes obtenues à des longueurs d'onde spécifiques couvrant le spectre du visible au proche infrarouge (NIR). Dans cette technique, le facteur de transmission, l'absorption et la diffusion de la lumière sont reflétés dans le spectre de la lumière émise par le tissu. Par conséquent, non seulement les caractéristiques spatiales communes mais également les « signatures spectrales » de biomolécules pourraient être révélées. Cela aide à trouver une plus grande variété de caractéristiques spatiales / spectrales pour une investigation plus précise des biomarqueurs rétiniens des maladies.

En ce qui concerne les coûts et les limites associés aux diagnostics actuels de l'AD et de l'ATH, le but de cette thèse était d'analyser le contenu en informations d'images rétiniennes hyperspectrales riches en données dans le but de caractériser des informations discriminantes cachées liées aux tissus afin d'identifier des biomarqueurs possibles de ces deux maladies. À cette fin, une combinaison de caractéristiques vasculaires et de mesures de textures spatiales-spectrales ont été extraites de différentes régions anatomiques de la rétine.

Dans le contexte de la maladie d'Alzheimer, des images rétiniennes de 20 cas présentant une altération cognitive et de 26 cas normaux cognitivement ont été acquises à l'aide de la caméra MHRC. Le statut amyloïde cérébral a été déterminé à partir de lectures binaires effectuées par un panel de 3 experts noteurs ayant participé à des études de TEP au 18F-Florbetaben.

Des caractéristiques de l'image rétinienne ont été calculées, notamment la tortuosité et le diamètre des vaisseaux, ainsi que les mesures de textures spatiales-spectrales sur les artérioles, les veinules et le tissu environnant. Les veinules rétiniennes des sujets amyloïdes positifs (Aβ +) ont présenté une tortuosité moyenne plus élevée par rapport aux sujets amyloïdes négatifs (Aβ-). Le diamètre artériolaire des sujets Aβ + s'est avéré supérieur à celui des sujets Aβ- dans une zone adjacente à la tête du nerf optique. De plus, une différence significative entre les mesures de texture construites sur les artérioles rétiniennes et leurs régions adjacentes a été observée chez les sujets Aβ + par rapport aux Aβ-.

Dans le contexte de l'ATH, 60 images rétiniennes de 30 ATH probables sur le plan clinique et 30 cas de contrôle ont été acquises. Les critères d'inclusion pour les sujets souffrant d'ATH comprenaient: l'infarctus du myocarde; angiographie coronaire montrant au moins une sténose coronaire (plus de 50%); et / ou une angioplastie coronaire; et /ou pontage coronaire.

Les artérioles rétiniennes des sujets ATH ont montré un rétrécissement significatif par rapport aux sujets témoins. En outre, une différence significative entre les mesures de textures d'images prises sur les artérioles et les veinules rétiniennes et leurs régions adjacentes a été trouvée entre les sujets ATH et les sujets témoins.

Nos études transversales ont montré que l'analyse hyperspectrale des images rétiniennes pouvait discerner avec une précision acceptable l'AD et l'ATH des sujets témoins correspondants.

ABSTRACT

The fact that eye can be visualized non-invasively, opens up possibilities to measure biomarkers for diagnosis of long-term conditions. A significant body of literature has demonstrated that many of the neurodegenerative and cardiovascular diseases such as Alzheimer's disease (AD) and atherosclerosis (ATH) manifest themselves in retina as pathological and/or vasculature morphological changes. Methods for two-dimensional fundus imaging and techniques for three-dimensional optical coherence tomography (OCT) have been developed to provide descriptions of retinal structures. However, images acquired by these techniques mostly allow for measuring the spatial characteristics of the tissue and lack of the relative variances across differing wavelengths, thus important spectral features may remain uncovered.

In this study, a Metabolic Hyperspectral Retinal Camera (MHRC) was used that permits the acquisition of a series of retinal images obtained at specific wavelengths covering the visible and near infrared (NIR) spectrum. In this technique, light transmittance, absorption, and scatter are reflected in the spectrum of light emitted from the tissue. Use of MHRC in this study was aimed to extract not only the common spatial features but also "spectral signatures" of biomolecules in retinal tissue.

Regarding the costs and limitations of the current diagnostic methods for AD and ATH, the purpose of this thesis was to analyze the information content of data-rich hyperspectral retinal images to characterize tissue-related discriminatory information to identify possible biomarkers of Alzheimer's disease and atherosclerosis. To this end, a combination of vascular features and spatial/spectral texture measures were extracted from different anatomical regions of the retina.

In the context of AD, retinal images from 20 cognitively impaired and 26 cognitively unimpaired cases were acquired using MHRC. The cerebral amyloid status was determined from binary reads by a panel of three expert raters on 18F-Florbetaben PET studies. Our approach did not aim to visualize directly Aβ deposits in the retina but rather to determine a likely amyloid status based on sets of retinal image features highly correlated with the cerebral amyloid status.

Retinal image features were calculated including vessels' tortuosity and diameter. Spatial/spectral texture measures over arterioles, venules, and tissue around were also extracted. Retinal venules of amyloid positive subjects (Aβ+) showed a higher mean tortuosity compared to the amyloid

negative (Aβ-) subjects. Arteriolar diameter of Aβ+ subjects was found to be higher than the Aβ- subjects in a zone adjacent to the optical nerve head. Furthermore, a significant difference between spatial/spectral texture measures built over retinal arterioles and surrounding tissues were observed in Aβ+ subjects when compared to the Aβ-.

In the context of ATH, 60 retinal images from 30 clinically probable ATH and 30 control cases were acquired. Inclusion criteria for subjects suffering from ATH included: myocardial infarction; coronary angiography showing at least one coronary stenosis (more than 50%); and/or coronary angioplasty; and/or coronary bypass.

Retinal arterioles of ATH subjects showed a significant narrowing when compared to control subjects. Moreover, a significant difference between image texture measures taken over retinal arterioles and retinal venules and their adjacent regions was observed between ATH subjects and control subjects.

Our cross-sectional studies have shown that hyperspectral retinal image analysis could be used to discriminate AD and ATH from corresponding control subjects based on a non-invasive eye scan.

TABLE OF CONTENTS

LIST OF TABLES

LIST OF FIGURES

LIST OF SYMBOLS AND ABBREVIATIONS

2D	Two-dimensional
3D	Three-dimensional
AD	Alzheimer's disease
AOC	Arc over chord
ARIC	Atherosclerosis risk in communities study
ASM	Angular second moment
ATH	Atherosclerosis
AV	Arteriolo venular
CNS	Central nervous system
CRAE	Central retinal arteriolar equivalent caliber
CRVE	Central retinal venular equivalent caliber
CHT	Circle Hough transform
CVD	Cardiovascular diseases
DM	Diabetes mellitus
FOV	Field of view
GCL	Ganglion cell layer
GLCM	Grey level co-occurrence matrix
GUI	Graphical user interface
HSI	Hyperspectral imaging
IMT	Intima-media thickness
IPL	Plexiform layer
IVUS-VH	Virtual-histology intravascular ultrasound
LDA	Linear discriminant analysis

LV	Left ventricle
MCI	Mild cognitive impairment
MESA	Multi-ethnic study of atherosclerosis
MHRC	Metabolic hyperspectral retinal camera
MRI	Magnetic resonance imaging
OCT	Optical coherent tomography
OCTA	Optical coherence tomography angiography
ONH	Optical nerve head
PCA	Principal component analysis
PET	Positron emission tomography
QDA	Quadratic discriminant analysis
RA	Rheumatoid arthritis
RGB	Red-green-blue
RGC	Retinal ganglion cell
RNFL	Retinal nerve fiber layer
SD-OCT	Spectral-domain optical coherence tomography
SFS	Sequential feature selection
SIVA	Singapore I vessel assessment
SLO	Scanning laser ophthalmoscopy
SVM	Support vector machine
TDR	Trunk diameter ratio
TLS	Tunable laser source

LIST OF APPENDICES

CHAPTER 1 INTRODUCTION

1.1 Retina and retinal manifestations of diseases

The light sensitive inner layer of the eye, the retina (Figure 1.1) is an extension of the central nervous system (CNS). The retina's role is to enable the conversion of incoming light into a neural signal that is suitable for further processing in the visual cortex. Since retinal blood vessels are part of the brain vasculature, they also share anatomical features and respond similarly to neurovascular diseases (Patton et al., 2007). Retinal ganglion cells (RGC) project axons through the optic nerve to the brain and therefore, a central hypothesis of this thesis is that retinal investigations can be exploited to explore neuronal degenerative disorders (London, Benhar, & Schwartz, 2013). Clinical observations of fundus features have, over time, provided evidence that long-term conditions such as diabetes mellitus (N. Cheung, Mitchell, & Wong, 2010; Heitmar, Lip, Ryder, & Blann, 2017a), stroke (Baker, Hand, Wang, & Wong, 2008; Chandra et al., 2018; McGeechan et al., 2009), hypertension (Sharrett et al., 1999; T. Wong & Mitchell, 2007) and cardiovascular diseases (CVD) (Flammer et al., 2013; Heitmar et al., 2017a; Liew & Wang, 2011; Yang et al., 2016) also have manifestations in the retina.

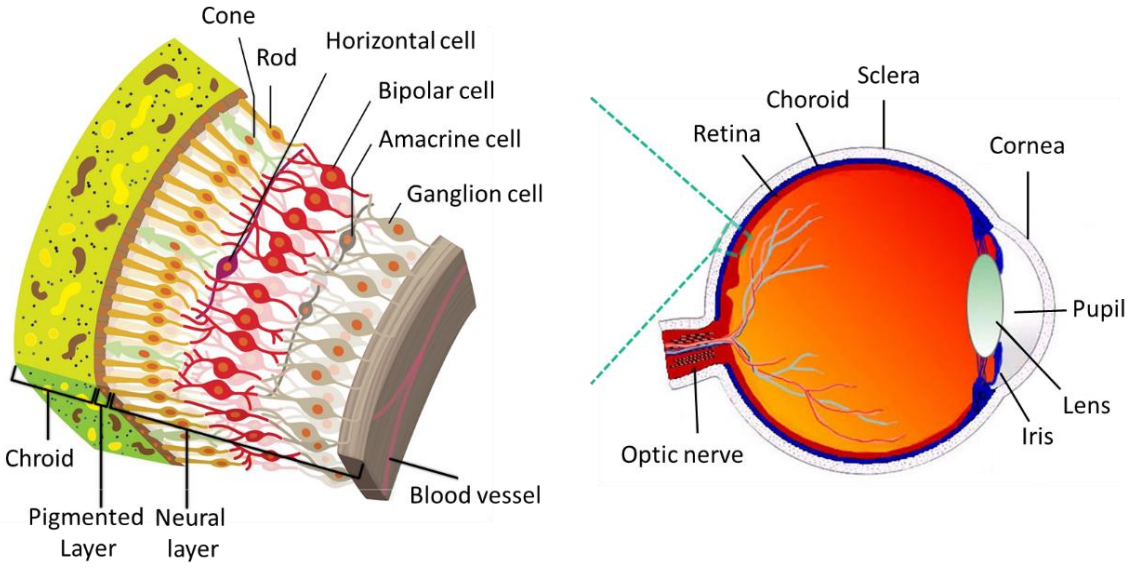

Figure 1.1 Illustration of retinal layers and anatomy of eye — Modified from (Kolb, 2003a; Mookiah et al., 2015)

Consequently, retinal imaging provides the opportunity of using a minimally invasive imaging method to examine pathological features through the transparent medium of the eye. In subsequent sections, we introduce two increasingly prevalent chronic diseases that were investigated in this work: Alzheimer's disease (AD) and atherosclerosis (ATH). This thesis was focused on identifying retinal biomarkers of these two diseases with the goal of adding supportive information to their diagnostic workflows.

1.1.1 Alzheimer's disease

Alzheimer's disease (AD) is a slowly evolving neurodegenerative disorder affecting the growing aging population. Clinically, AD patients suffer a progressive decline in memory and cognitive functions as well as social functioning (Javaid, Brenton, Guo, & Cordeiro, 2016). Pathologically, AD is characterized by the deposition of extracellular plaques composed of amyloid ß (Aß) and intraneuronal tangles, resulting from intracellular aggregates of hyperphosphorylated tau protein detected in the brain (Bloom, 2014). Deposition of Aß leads to cross-sectional synaptic network dysfunction, progressive brain atrophy, and longitudinal cognitive decline (Jagust, 2016).

A major issue with diagnosis is that so far, cerebral Aß plaques and protein tau tangles are only detectable in postmortem histopathology of AD brains. In vivo, cognitive testing is still regarded as the standard tool to diagnose AD but cognitive decline occurs late in the disease, years after Aß plaques start to accumulate. Beyond cognitive assessments occurring at later stages of the disease progression, positron emission tomography (PET) can be used to measure Aβ burden in the brain. PET allows for the three-dimensional mapping of administered positron-emitting radiopharmaceuticals such as Florbetaben. Florbetaben is a fluorine-18 (18F)-labeled stilbene derivative developed as a PET tracer for visualizing Aß plaques in the AD brain and therefore can yield a diagnosis of Alzheimer (Sabri, Seibyl, Rowe, & Barthel, 2015). However, costs, availability limitations, and exposure to radioactive isotopes restrain use of PET for population screening (Blennow, Mattsson, Schöll, Hansson, & Zetterberg, 2015; Khan & Alkon, 2015).

1.1.2 Atherosclerosis

Atherosclerosis (ATH) is a disease in which plaques (including cholesterol) accumulate in the inner most layer of the artery wall (the 'tunica intima'), and trigger an inflammatory response. The failure

to decrease lipid accumulation and improve clearing of apoptotic cells, leads to macrophage accumulation within the artery wall and ultimately narrowing the lumen of the artery restricting blood flow (Bories & Leitinger, 2017). Atherosclerosis can remain asymptomatic for decades and does not produce symptoms until sufficient narrowing or closure of an artery, due to clots, occurs when the patient experiences other cardiovascular disorders such as a stroke or heart attack (Publishing, n.d.). Beyond the late stage diagnosis methods that are focused on severe narrowing of arteries (e.g. angiography, and stress testing), current diagnosis relies on exploring characteristics of the arterial wall by measuring carotid intima-media thickness (IMT) and arterial stiffness (Lorenz, Markus, Bots, Rosvall, & Sitzer, 2007; Mitchell et al., 2010; Nambi et al., 2012; Niu et al., 2014). The carotid IMT is measured from ultrasound B-mode images by detecting the lumen-intima and media-adventitia interfaces over an artery segment (Niu et al., 2014; Tedeschi-Reiner, Strozzi, Skoric, & Reiner, 2005a). Arterial stiffness is mostly estimated by measuring the diameter change during the cardiac cycle from B-mode echo-tracking images (Sharrett et al., 1999).

1.2 Retinal imaging

The history of retinal imaging backs to more than a century and it is now an important element of the clinical care and screening of patients with retinal disorders and also systemic diseases. Current retinal imaging systems can be divided into two categories: Optical Coherent Tomography (OCT) and fundus imaging (Abràmoff, Garvin, & Sonka, 2010).

1.2.1 Optical coherent tomography (OCT)

OCT is used to estimate the depth at which a specific backscatter originated by measuring its propagation time or exploits frequency domain signals to infer depth backscattering. Since different tissues have different refractive indices, the backscatter from deeper tissues can be differentiated from backscatter originating at more superficial tissues by measuring each backscatter at the sensor. As the total retinal thickness is about 400 μm, the differences in indices are very small and can only be measured through interferometry (Abràmoff et al., 2010; Huang et al., 1991). OCT employs low-coherent light interferometry, also called white light interferometry. Most of the retinal layers can be seen on OCT images. Accordingly, it has been widely used in the diagnosis of diabetic retinopathy (G. Liu, Xu, & Wang, 2018), macular degeneration (Mantel, 2017), and inflammatory

retinal diseases (Vaudaux, 2017). OCT is also widely used in vitreo-retinal surgery (Kitaoka, Hara, Matsumoto, & Tsuiki, 2017).

1.2.2 Fundus imaging

Fundus imaging is defined as the process by which a two dimensional representation of the retinal tissues projected onto the imaging plane is obtained using reflected light. Thus, any process which results in a 2-D image, where the image intensities represent the amount of a reflected quantity of light, is termed fundus imaging (consequently, OCT is not considered as fundus imaging). Table 1.1 describes modalities/techniques belong to the broad category of fundus imaging (Abràmoff et al., 2010).

Table 1.1 Fundus imaging modalities/techniques and associated descriptions of image intensity (Abràmoff et al., 2010)

Fundus imaging modalities/techniques	**Image intensity**
Fundus photography	the amount of reflected light of a specific waveband
Color fundus photography	the amount of reflected Red, Green, and Blue wavebands, as determined by the spectral sensitivity of the sensor
Stereo fundus photography	the amount of reflected light from two or more different view angles for depth resolution
Hyper-spectral imaging	the amount of reflected light of multiple wavelength bands
Scanning laser ophthalmoscopy (SLO)	the amount of reflected single wavelength laser light obtained in a time sequence
Adaptive optics SLO	the amount of reflected laser light optically corrected by modeling the aberrations in its wavefront
Fluorescein angiography and indocyanine angiography	the amounts of emitted photons from the fluorescein or indocyanine green fluorophore that was injected into the subject's circulation

In this study, we used hyper-spectral retinal imaging (HSI) platform developed by Optina Diagnostics (“Optina Diagnostics,” n.d.) to acquire retinal images with the goal of identifying novel AD and ATH biomarkers. Taking advantages of HSI, a spectrum can be obtained for each pixel of the image. Thus, not only the anatomical structures can be observed (similar to conventional fundus imaging), but also spectral signatures can be extracted to localize and quantify specific

biomolecules in the retina. In Chapter 3, detailed explanation about this novel imaging platform will be provided.

1.3 Problem Statement

Early detection of Alzheimer's disease: Alzheimer is currently diagnosed by the post-mortem observation of Aβ plaques, and protein tau tangles which excludes this approach to be considered as a diagnostic tool during the lifetime in AD patients. Clinical testing on the other hand, lacks accuracy to establish a reliable AD diagnosis both at mild cognitive impairment (MCI) stages and even at the dementia stages of the disease (Beach, Monsell, Phillips, & Kukull, 2012; Doraiswamy et al., 2014). As mentioned earlier, Aβ plaque tracers for PET imaging are currently available to confirm the presence of this hallmark and therefore the diagnosis of AD, but the expenses and nature (radioactive) of this label makes it unlikely to be a cost effective screening tool for diagnosis of AD. This notion, has prompted incorporating other biomarkers as add-on to AD diagnostic process (Dubois et al., 2014; McKhann et al., 2011).

Due to the closed interconnection between retina and brain it is not surprising that neurodegeneration caused by AD extends into the retina. Many studies in the literature have shown evidence that changes in retinal vasculature (C. Y. Cheung et al., 2014; de Jong et al., 2011; S. Frost et al., 2013; Patton et al., 2005, 2007; Querques et al., 2019; Williams et al., 2015) , retinal nerve fiber layer (Ascaso et al., 2014; Berisha, Feke, Trempe, McMeel, & Schepens, 2007; C. Y. Cheung et al., 2015; Kesler, Vakhapova, Korczyn, Naftaliev, & Neudorfer, 2011; Kirbas, Turkyilmaz, Anlar, Tufekci, & Durmus, 2013; Querques et al., 2019), retinal ganglion cells (RGC) (Kesler et al., 2011; Kolb, 2003b; B. Liu et al., 2009; Querques et al., 2019), and deposition of Aß in retina (Ratnayaka, Serpell, & Lotery, 2015; Williams et al., 2015), identifiable on fundus imaging may provide markers of AD. These relationships motivated us to investigate retinal images focusing on vessels and adjacent tissue regions with the aim of finding AD biomarkers. This study was conducted using a novel hyper-spectral retinal imaging device which was anticipated to provide increase information content when compared to previous work.

Early detection of atherosclerosis: Atherosclerosis is the most common cause of cardiovascular disease. Despite the growing importance of atherosclerosis and its implications for public health, there is a lack of studies toward early detection of subclinical atherosclerosis in asymptomatic

subjects. Current diagnostics rely on blood tests, imaging to identify severe narrowing of the arteries, e.g. angiography, and stress testing. However, except for blood tests, these methods are focused on severe narrowing of arteries, not the underlying atherosclerosis disease (Publishing, n.d.). On the other hand, diagnostic methods based on measuring arterial characteristics (e.g. Carotid IMT, arterial stiffness, pulse wave velocity, arterial compliance and distensibility, and the elastic modulus of the vessel wall (Lorenz et al., 2007; Mitchell et al., 2010; Nambi et al., 2012; Ren, Cai, Liang, Li, & Sun, 2015) in addition to cost, are highly operator-dependent and time-consuming (Niu et al., 2014). Thus, a quantitative method for early detection of asymptomatic subjects remains confounded in many ways. Reviewing subsequent and more recent literature, cardiovascular diseases, and more specifically atherosclerosis, have manifestations in retinal arterioles and venules (Adzhemian et al., 2016, p. 1; Anyfanti et al., 2017; Chandra et al., 2018; N. Cheung et al., 2007, 2007; Chiu et al., 2018, 2018; Couper et al., 2002; Heitmar et al., 2017a; Kovarnik et al., 2016; McGeechan et al., 2009; Peña et al., 2018, p. 1; Seidelmann et al., 2016; Sharrett et al., 1999; Tedeschi-Reiner et al., 2005a; Wang et al., 2008; T. Y. Wong et al., 2007). Low cost, wide availability, and less-invasive assessments are the advantages of using retinal imaging as a possible method of finding signs of atherosclerosis at its early stages (Chiu et al., 2018). As the second part of the research, in this thesis, spatial and spectral image features of retinal vasculature and adjacent tissue in a cohort of ATH positive and age-matched control subjects were investigated with the goal of identifying biomarkers of ATH and their prediction ability.

1.4 Objectives, hypotheses and research work overview

The general objective of this Ph.D. project is to (1) Investigate image features of retinal vasculature and adjacent tissue in a cohort of AD positive and control subjects with the goal of identifying biomarkers of AD; (2) Confirm the usefulness of extracted retinal features for identifying biomarkers of a separate disease, ATH, and develop algorithms to discern between ATH and healthy control participants.

Specific objectives are stated below with corresponding hypotheses:

Objective 1: Based on data accumulated using a hyper-spectral imaging device, find retinal biomarkers of subjects with positive cerebral amyloid status and investigate the prediction ability of the biomarkers.

Hypothesis1-1: Image analysis of vasculature and hyperspectral features of retinal tissues yields measures to predict cerebral amyloid status

- Article 1: **Sayed Mehran Sharafi**, Jean-Philippe Sylvestre, Claudia Chevrefils, Jean-Paul Soucy, Sylvain Beaulieu, Tharick A Pascoal, Jean Daniel Arbour, Marc-André Rhéaume, Alain Robillard, Céline Chayer, Pedro Rosa-Neto, Sulantha S. Mathotaarachchi, Ziad S. Nasreddine, Serge Gauthier, Frédéric Lesage ; Vascular retinal biomarkers improves the detection of the likely cerebral amyloid status from hyperspectral retinal images; accepted for publication in the journal of Alzheimer's & Dementia: Translational Research & Clinical Interventions (TRCI)

Objective 2: Find ocular biomarkers of atherosclerosis subjects using hyper-spectral retinal images and evaluate their prediction ability

Hypothesis 2-1: Retinal vasculature and texture features yields measures to discriminate atherosclerosis subjects and healthy control subjects.

- Article 2: **Sayed Mehran Sharafi**, Jean-Philippe Sylvestre, Claudia Chevrefils, Jean-Claude Tardif, Marc-André Rhéaume, Jean Daniel Arbour , Frédéric Lesage; Hyperspectral retinal biomarkers of atherosclerosis; submitted to the journal of Biomedical Optics Express on July 2019
- **Sayed Mehran Sharafi**, Jean-Philippe Sylvestre, Claudia Chevrefils, Jean-Paul Soucy, Frédéric Lesage, Correlation between PET-derived cerebral amyloid status and retinal image features using a hyperspectral fundus camera, Clinical and Translational Neurophotonics, SPIE photonics west BIOS, San Francisco, California, United States, Febuary 2019

  J.-P. Soucy, C. Chevrefils, J.-P. Sylvestre, S. Beaulieu, T. A. Pascoal, **S. M. Sharafi**, J.-D. Arbour, M.-A. Rhéaume, A. Robillard, C. Chayer, P. Rosa-neto, S. S. Mathotaarachchi, Z. S. Nasreddine, S. Gauthier, F. Lesage, Validation of a hyperspectral retinal imaging method to predict cerebral amyloid PET status. In: 2018 Neuroscience Meeting Planner. San Diego, CA: Society for Neuroscience; 2018

This thesis is organized as follows: Chapter 2 provides a brief literature review on studies conducted to find retinal biomarkers of AD and ATH; Chapter 3 describes the methods and technologies developed for this study in details. In chapter 4 and chapter 5, two papers are included to address the two individual objectives; General discussion and conclusion are provided in chapters 6 and 7 respectively.

CHAPTER 2 LITERATURE REVIEW

The retina is a unique part of the body that allows observation of blood vessels and studying the CNS *in vivo* with non-invasive imaging (London et al., 2013). An increasing number of studies have found that changes to the retinal vasculature and other tissues can occur in some chronic diseases years before their clinical signs become apparent (Baker et al., 2008; N. Cheung et al., 2010; Heitmar et al., 2017a; Liew & Wang, 2011; Patton et al., 2005; Tedeschi-Reiner et al., 2005a; T. Wong & Mitchell, 2007). Thus, studying the retina may provide clinicians with early indicators of long-term illnesses and chronic conditions.

The focus of this PhD thesis is the investigation of ocular biomarkers of Alzheimer's disease and atherosclerosis. In this chapter, a literature review on retinal manifestation of these two conditions will be given.

2.1 Manifestations of Alzheimer's disease in retina

The most commonly reported pathological changes in the retina of AD patients includes: retinal nerve fiber layer (RNFL) thinning (Ascaso et al., 2014; Kesler et al., 2011; Kirbas et al., 2013; Querques et al., 2019), retinal ganglion cell layer (GCL) degeneration (C. Y. Cheung et al., 2015; Querques et al., 2019), Aβ deposition in the retina (Campbell et al., 2015; Koronyo-Hamaoui et al., 2011; More & Vince, 2015), and functional and morphological changes of the retinal vessels (C. Y. Cheung et al., 2014; de Jong et al., 2011; S. Frost et al., 2013; Patton et al., 2005, 2007; Querques et al., 2019; Williams et al., 2015). Following we discuss each of the mentioned hallmarks in detail.

2.1.1 RNFL and GCL changes

The innermost cellular layer of the retina—the GCL layer— (Figure1.1), projects its axons across the RNFL through the optic nerve to the brain. The RNFL has unmyelinated axons that directly synapse into the CNS making the eye an excellent site for screening neurodegeneration. In a very recent study, Querques et al. (Querques et al., 2019) used OCT and optical coherence tomography angiography (OCTA) to quantitatively investigate anatomical metrics in the retina of AD and MCI subjects, including thicknesses of the RNFL, the GCL inner plexiform layer (IPL), and the ganglion cell complex (GCC - resulted as GCL +IPL) using dynamic vessel analyzer and optical coherence

tomography. They reported that the central thickness (the average thickness in the 1-mm diameter ring centered at the fovea) of the RNFL significantly decreased in both AD and MCI subjects. They also found that the average GCL thickness at central and temporal sectors are significantly thinner in AD and MCI subjects than in healthy controls. In (Ascaso et al., 2014) Ascaso et al. used OCT to measure circumpapillary RNFL thickness in μm. Through an analysis of variance, they showed that RNFL was thinner in MCI patients compared with controls, and it was also thinner in AD patients compared with MCI patients and controls. Using spectral-domain optical coherence tomography (SD-OCT), Cheung et al. (C. Y. Cheung et al., 2015) showed that compared with control subjects, patients with AD had significantly reduced GC-IPL thicknesses in all six sectors (superior, superonasal, inferonasal, inferior, inferotemporal, and superotemporal). They also showed that RNFL thickness was significantly reduced in the superior quadrant (–6.04 μm, $p = 0.039$) of AD patients compared to healthy control subjects. Kirbas et al. (Kirbas et al., 2013) using SD-OCT found that the average RNFL thickness was significantly reduced in AD patients than in controls (65 ± 6.2 μm vs 75 ± 3.8μm; $P = 0.001$). In (Kesler et al., 2011), Kesler et al. using OCT showed that there was a significant decrease in RNFL thickness in both AD and MCI compared to the control group, particularly in the inferior quadrants of the optic nerve head, while the superior quadrants were significantly thinner only in AD.

2.1.2 Aβ deposition in retina

Koronyo-Hamaoui et al. (Koronyo-Hamaoui et al., 2011) identified retinal Aβ plaques in postmortem eyes from AD patients (n=8) and in suspected early stage cases (n = 5), while they were undetectable in age-matched non-AD individuals (n = 5). Moreover, in an animal experiment following systemic administration of curcumin (a safe plaque labeling fluorochrome), they detected retinal Aβ plaques in $APP_{SWE}/PS1_{\Delta E9}$ transgenic mice (AD-Tg; n = 18) but not in non-Tg WT mice (n = 10). Aβ plaques in the retina of both human and mice AD subjects were reported to be found in abluminal (around) and intraluminal (inside vessels) positions.

In (Campbell et al., 2015) Campbell et al. performed polarimetry on amyloid deposits in human postmortem retinas of subjects with a diagnosis of AD. They found that polarization imaging provide contrast for amyloid deposits against the surrounding retina of AD subjects.

More & Vince (More & Vince, 2015) used a hyper-spectral endoscopy system, captured scattering of light of visible near-infrared wavelengths (400−1000 nm) within each pixel of the microscopic view field, and then assembled a scattering intensity pattern database that provided spectral "signatures" of Aβ1−42 peptide. Comparison of unknown samples against this database enabled them to detect amyloid aggregate in the retina of AD mice models.

Koronyo et al.(2017) in a comprehensive study using different imaging techniques on live human subjects, post mortem retinal tissues and animal models found correlation between retinal Aβ plaque burden and cerebral Aβ plaques. They showed that retinal Aß deposits are apparent inside blood vessels, perivascular areas, and along the vessel walls mostly at retinal superior temporal and inferior-nasal quadrants. They used oral administration of curcumin to the subjects to increase retinal fluorescent intensities of Aβ plaques.

2.1.3 Vasculature changes

Large population studies suggest that retinal vascular abnormalities are prevalent in AD patients (Figure 2.1 illustrates examples of retinal vessels' characteristics and vasculature abnormalities in patients with Alzheimer's disease).

In (Berisha et al., 2007), Berisha et al. used a laser Doppler imaging device, in a small cohort showed that retinal venules in AD subjects are significantly narrower than healthy controls. They also reported that venous blood flow was significantly reduced in AD compared with healthy controls. Frost et al. in (S. Frost et al., 2013), using retinal color photography, reported that that the venular branching asymmetry and arteriolar length-to-diameter ratios were higher in healthy individuals with high plaque burden, as measured by PET imaging using PiB. Using fundus photography and automated vessel segmentation software, Cheung et al. (C. Y. Cheung et al., 2014) showed a reduction in retinal vessel caliber and also reduction in the global branching pattern of the retinal vascular tree (known as the fractal dimension). They also reported increase in tortuosity of retinal vessels. Feke et al. (Feke, Hyman, Stern, & Pasquale, 2015), using a laser Doppler imaging device, showed that significant differences in venous blood flow helped to discern AD from MCI and control subjects .

In (Williams et al., 2015), Williams et al. investigated retinal vascular parameters from the retinal photographs of 213 AD participants and 294 cognitively normal controls. They reported that mean Central Retinal Arteriolar Equivalent Caliber (CRAE) of AD patients were higher than the control subjects but no significant difference in Central Retinal Venular Equivalent Caliber (CRVE) was reported. They also showed that fractal dimension of vessels in AD patients was significantly lower than controls. Moreover, retinal arteriolar tortuosity of AD subjects was reported to be significantly less than the control subjects. Querques et al. in (Querques et al., 2019) using OCTA showed that none of the static vascular parameters including arteriolar-venular ratio (AVR), CRAE, and CRVE are significantly different between AD and healthy control subjects. However, they reported that CRAE and CRVE were correlated with the burden of phosphorylated-tau protein—one of the AD biomarkers — in cerebrospinal fluid (CFS).

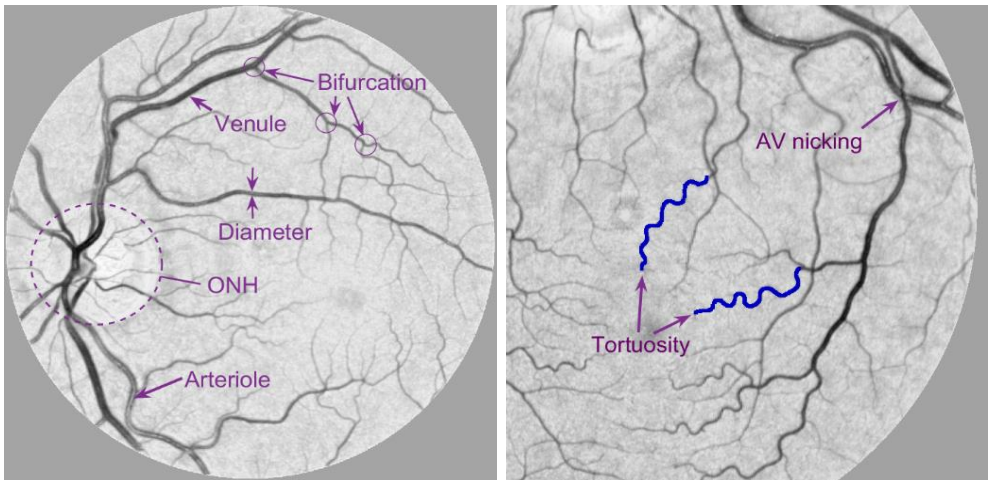

Figure 2.1 Retinal vasculature characteristics (left); Tortuous venule segments and arteriovenular nicking (AV nicking) in a patient with Alzheimer's disease (right)

Table 2.1 summarizes the studies conducted on the investigation of retinal biomarkers of AD along with their attributes including, number of participants, imaging modality/technique site of investigation, and biomarkers found.

Table 2.1 Comparison of studied conducted on retinal biomarkers of AD

Study	Cohort	AD diagnostic method(s)	Imaging technique(s)	Image processing tool(s)	Retinal site(s) investigated	Biomarker(s) found
Berisha et al. 2007	9 AD 8 CT	Cognitive tests	OCT; Laser Doppler imaging		Vasculature(statics and dynamics); RNFL	Specific pattern of RNFL loss, narrow venules, and decreased retinal blood flow in venules of AD subjects
Koronyo-Hamaoui et al. 2011	8 AD, 5 MCI, 5 CT (postmortem); Mice study	Cognitive tests	HSI; Fluorescence microscopy	Custom-built software	Whole retina	Aβ plaques in retina of both human and mice AD subjects reported to be found in abluminal (around) and intraluminal (inside vessels) positions.
Kesler et al. 2011	30 AD, 24 MCI, 24 CT	Cognitive tests	OCT		RNFL	significant decrease in RNFL thickness in AD and MCI groups compared to the control group, particularly in the inferior quadrants of the optic nerve head
Frost et al. 2013	25 AD 123 CT	PET-PiB, Cognitive test	Digital Retinal color photography	SIVA Software	Static vasculature parameters	Higher venular branching asymmetry and AVR in PiB+ AD subjects and healthy individuals with high plaque burden; Less tortuous vessels in AD subjects
Kirbas et al.2013	40 AD, 80 CT	Cognitive tests	OCT		RNFL	RNFL thinning in the superior quadrant of the AD patients
Cheung et al. 2014	136AD	Cognitive tests; CT/MRI	Retinal photography	SIVA software	Static vasculature parameters	reduction in retinal vessel caliber, reduction in fractal dimension, and increase in retinal vessels tortuosity in AD subjects
Ascaso et al. 2014	18 AD, 21 MCI, 41 CT	Cognitive tests	OCT	OCT device built-in software;	RNFL	RNFL thinning in MCI patients compared with controls, RNFL thinning in AD patients compared with MCI patients and controls
Williams et al. 2015	213 AD 294 CT	Cognitive tests	Retinal photography	SIVA software	Static vasculature parameters	Higher CRAE of AD patients compared to the control subjects but no significant difference in CRVE; Significantly lower fractal dimension of vessels in AD patients than controls; Lower retinal arteriolar tortuosity of AD subjects in comparison with the control subjects

Feke et al. 2015	10 AD 21 MCI 21 CT	Cognitive tests	Retinal laser Doppler flowmetry; OCT		Vasculature (statics and dynamics); RNFL	Narrower blood column diameter in AD compared to MCI and controls lower blood speed in both AD and MCI in comparison with controls; No differences in RNFL thickness between the groups,
More & Vince 2015	8 mice models		Hyperspectral endoscopy		Whole retina	Amyloid aggregate in retina of AD mice models
Campbell et al. 2015	Small cohort (postmortem)	Cognitive tests	Fluorescence microscopy; Polarimetery		Whole retina	AB deposition in neural layers of the retina, close to the anterior surface of the retina of AD subjects
Cheung et al. 2015	100 AD, 41 MCI, 123 CT	Cognitive tests	SD-OCT		RNFL	RNFL thinning in superior quadrant of AD patients compared to MCI
					GCL-IPL	GC-IPL thinning in AD compared to controls
					Macula	Higher macular volume in MCI patients compared to AD patients and controls;
Koronyo et al. 2017	23 AD and controls; Postmortem /live; Mice models	Cognitive test, Neuropathology	Ophtalmoloscope; Fluorescence microscopy; OCT; Transmission electron microscopy	Custom software and OCT built-in	GCL; Retinal pigmented epithelium	AB deposition inside blood vessels, perivascular, and along the vessel walls mostly at retinal superior temporal and inferior-nasal quadrants.
Querques et al., 2019	12 AD, 12 MCI, 32 CT	Dementia assessments, PET, quantification of CSF Aβ, tau protein, and phosphorylated tau protein	OCT, OCTA	OCT device built-in software; ImageJ	Vasculature(statics and dynamics)	No change in CRAE and CRVE in AD or MCI, but correlation between CRAE and phosphorylated tau protein in CSF; Decrease in arterial dilation in AD group.
					RNFL	Central thinning of RNFL in both AD and MCI
					GCL	GCL degeneration at central and temporal sectors in both AD and MCI
					IPL	Average GCL thickness at temporal sectors are significantly thinner in AD and MCI subjects than the healthy controls.
					Macula	Significant decrease in macular volume in AD and MCI

Despite the effectiveness of PET imaging and CSF molecules, their widespread implementation for AD diagnosis remains a challenge. On the other hand, retinal biomarkers for AD have their own limitations. Many of the retinal biomarkers reviewed in this section overlap with ocular and systemic diseases. Even the ocular biomarkers holding the most promise to be specific for AD pathophysiology, such as the Aß-related retina changes, have drawbacks because of the lack of a correlation between Aβ plaques in AD brains and the extent of cognitive decline in AD patients remain confounded (Ratnayaka et al., 2015). Therefore, using enhanced imaging techniques to extract an array of functional and structural retinal characteristics may improve detection of retinal biomarkers specific for AD.

Currently, the majority of retinal imaging modalities such as fundus cameras and OCT were limited to spatial aspects and did not reveal spectral tissue absorbance values. However, hyperspectral imaging in addition to common spatial features, determines the spectral absorption characteristics for multiple narrow spectral bandwidths from the UV to infrared spectrum. This facilitates the use of spectral/spatial combination of features for better characterization of AD related pathological changes in retina. Moreover, a range of other neurological and vascular diseases may also stand to benefit from that technologies.

2.2 Manifestations of cardiovascular diseases in retina

The vasculature of the eye shares many features with the vasculature of the heart and is often exposed to the same influences (Flammer et al., 2013). Thus, it is not surprising that retinal vascular changes, identifiable on fundus imaging provide markers of cardiovascular disease. Since the majority of the studies used the Atherosclerosis Risk in Communities (ARIC) database, as the first step to review the literature of retinal biomarkers of atherosclerosis, we briefly introduce ARIC study.

Atherosclerosis Risk in Communities Study (ARIC)

ARIC study (1989) is a prospective investigation of factors related to atherosclerosis and the incidence of coronary heart disease in cohort of 15,792 males and females aged 45-64 years. It was conducted at baseline selected using probability sampling from four United States communities (Forsyth County NC, Jackson MS, suburban Minneapolis MN, and Washington County MD).

Atherosclerosis was assessed by using carotid artery ultrasound imaging. Of those examined at baseline, 14,368 (93 percent of the survivors) returned for a second examination 3 years later (in 1990-1992), and 12,887 (86 percent of the survivors) returned for a third examination 6 years later (in 1993-1995). For addition of an assessment of arterioles to the assessment of large-artery diseases, retinal photography was performed at the third clinic examination, when the participants were aged 50-71 years. Briefly, a 45-degree non-mydriatic retinal photograph was taken of one eye, which was selected at random. The photograph was centered on the optic disk and macula.

Retinal changes associated with cardiovascular disease are categorized as structural and functional changes (Flammer et al., 2013). In this section, a detailed review and comparison among studies conducted on these two categories will be given.

2.2.1 Structural changes

Structural retinal changes reported as early indicators of coronary artery disease include: focal arteriolar narrowing, dilatation of venules, arterio-venous (AV) nicking, decrease in AVR, haemorrhage, micro-aneurysm, cotton wool spot (Liew & Wang, 2011), increase wall-to-lumen ratio of retinal arterioles (Ritt Martin & Schmieder Roland E., 2009) , suboptimal microvascular branching (very dense or very sparse vessel network)(Liew et al., 2011).

Sharrett et al. (1999) in a study on ARIC datasets reported that generalized narrowing of smaller arterioles is strongly and monotonically related to current blood pressure in men and women. They also showed that AV nicking is also related to both current and previous blood pressures. Moreover, AVR adjusted for age, race, and current cigarette smoking, is inversely correlated with blood pressure but correlates with trunk diameter ratio (TDR) —the ratio of the observed trunk diameter to the diameter of its two measured branches. They concluded that reduced AVR with larger TDRs indicate generalized narrowing, particularly in the more peripheral arterioles located approximately in region from 0 to0.5 ONH diameters away from the ONH margin (i.e. zone A of retina).

Couper et al. (Couper et al., 2002) using ARIC showed the association of retinal arteriolar narrowing with cardiovascular disease. Tedeschi-Reiner et al. (2005b) using direct ophthalmoscopy in 109 patients, aged 40 to 80 years, showed strong correlation between retinal vessel atherosclerosis (characterized by thickening of the arterial wall and lipid deposition in the

intima) with the extent and severity of coronary artery disease diagnosed by coronary angiogram. Wang et al. (2008) , using retinal photography on a cohort of 212 men and women aged 45 to 84 years showed that narrower retinal arterioles were associated with lower hyperemic myocardial blood flow and perfusion reserve in asymptomatic adults.

Cheung et al. (2007), in a research conducted on the Multi-Ethnic Study of Atherosclerosis (MESA) —a prospective cohort study of 6814 men and women ages 45 to 84 years without a history of clinical cardiovascular disease, sampled from 6 U.S. communities (Bild et al., 2002)— reported that narrower retinal arteriolar caliber was associated with concentric remodeling determined by the ratio of left ventricular mass to end-diastolic volume (M/V ratio). Wong et al. (2007), using fundus photography of MESA study after adjustment of the cohort for age, gender, race/ethnicity, blood pressure, diabetes, lipid profile, smoking, and other risk factors, showed that retinopathy was associated with having a moderate-to-severe coronary artery calcification (CAC) score. However, they reported no association between retinal vascular caliber and CAC score.

McGeechan et al. (2009), combining individual data from 6 cohort studies from Medline (National Library of Medicine, Bethesda, Maryland) and EMBASE (Elsevier B.V., Amsterdam, the Netherlands) databases, conducted a study on the association of retinal vessels caliber with stroke events. They showed that the wider retinal venular caliber could predict stroke. However, the caliber of retinal arterioles was not associated with stroke. Kovarnik et al. (2016), in a study on 32 patients used Virtual-histology Intravascular Ultrasound (IVUS-VH) for assessing the relationship between plaque features in borderline coronary stenosis and the thicknesses of retinal layers (imaged by OCT). They showed that plaque indices obtained by IVUS-VH (which exhibit relationships with future coronary events), correlate with indices of retinal layer thicknesses. Adzhemain et al. (2016), investigated retina of 55 atherosclerosis patients and 25 age-matched control subjects with retinal photography. They reported that mean retinal venular caliber was significantly wider in patients with atherosclerosis than in control group but no changes in retinal arteriolar caliber of the patients were reported.

Yang et al. (2016), in a study including a sub-population of Kailuan study (consisting of 101,510 employees and retirees of a coal mining industry), showed that thinner retinal artery diameter was significantly, however weakly, associated with increased common carotid artery IMT, thus indicator for an atherosclerotic carotid artery pathology. Anyfanti et al. (2017), investigated retinal

vessel morphology in a cohort consisted of 87 rheumatoid arthritis (RA) patients and 46 control subjects in regard to systemic inflammation, subclinical atherosclerosis, and cardiovascular risk. They assessed subclinical atherosclerosis with carotid IMT, and 10-year risk of general cardiovascular disease. They showed that, both CRAE and AVR were decreased in RA patients compared to controls. Moreover, they reported that in RA patients, CRAE and AVR were inversely associated with carotid IMT. They also showed that, CRAE was correlated with cardiovascular risk score. They concluded that retinal arteriolar narrowing might be an indicator of cardiovascular risk prediction in RA. Heitmar et al. (2017a) in a study conducted on a cohort consisted of 116 patients (36 diabetes mellitus—DM—patients only, 43 CVD only and 37 CVD and DM subjects), investigated both static and dynamic retinal vascular parameters. They showed that there is no significant difference in CRAE, CRVE and AVR among these groups.

Peña et al.(2018), investigated retinal vascular geometry of 90 adolescents with type 1 diabetes from retinal photographs. They measured carotid and aortic IMT using ultrasound. They reported a significant associations between thicker carotid IMT and wider retinal arteriolar and venular calibers. Moreover, they showed that increased mean aortic IMT was associated with increased arteriolar tortuosity. They concluded that retinal microvascular changes in adolescents with type 1 diabetes could be associated with early changes of atherosclerosis. Chandra et al. (2018), in a study based on ARIC but on the subjects underwent echocardiography between 2011-2013, showed that narrower retinal arterioles and wider retinal venules were significantly associated with greater left ventricle (LV) mass and worse diastolic indices.

2.2.2 Functional changes

Structural vascular change is usually a consequent of endothelial dysfunction. An impaired endothelial function is a well-known characteristic of CVD and specifically atherosclerosis (Bonetti, Lerman, & Lerman, 2003; Flammer et al., 2013). A growing body of literature has examined flicker light-induced vasodilation of the retinal vessels and reported dynamic changes in vascular endothelium of patients with CVD risk factors (Adzhemian et al., 2016; Delles et al., 2004; Heitmar, Lip, Ryder, & Blann, 2017b; Kotliar et al., 2011; Mandecka et al., 2007; Reimann et al., 2009).

Because of the focus of this thesis on structural changes in retinal vasculature and tissues around as a sign of atherosclerosis, here we made a comparison between studies addressing this part of the literature. Table 2.2 summarizes the studies mentioned in section “structural changes”.

Table 2.2 Comparison of studies conducted on retinal vasculature changes associated with cardiovascular diseases and risk factors

Study	**Cohort**	**CVD event /risk factor**	**Diagnostic method(s)**	**Retinal imaging technique(s)**	**Biomarker(s) reported**
Sharrett et al. (1999)	ARIC	Blood pressure	carotid artery ultrasound imaging	Retinal photography	Narrowing arterioles is related to blood pressure; AV nicking is related to blood pressures; AVR is inversely correlated with blood pressure but correlates with trunk diameter ratio
Couper et al., 2002	ARIC	Stroke	carotid artery ultrasound imaging	Retinal photography	Retinal arteriolar narrowing
Tedeschi-Reiner et al. (2005b)	109 patients, aged 40 to 80 years	Atherosclerosis; coronary artery disease	Gensini score; coronary angiograms	Ophthalmoscopy	Correlation between retinal vessel atherosclerosis with coronary artery disease
Wang et al. (2008)	212 aged 45 to 84	Hyperemic myocardial blood flow; Perfusion reserve	Myocardial blood flow measured using MRI	Retinal photography	Narrower retinal arterioles were associated with lower hyperemic myocardial blood flow and perfusion reserve in asymptomatic adults
Cheung et al. (2007)	MESA	Concentric remodeling	Cardiac MRI; M/V ratio	Fundus photography	Narrower retinal arteriolar caliber
Wong et al. (2007)	MESA	Coronary artery calcification (CAC)	Cardiac computed tomography	Retinal photography	retinopathy and AV nicking were associated with higher CAC scores
McGeechan et al. (2009)	A review on Medline and EMBASE	Stroke	Miscellaneous methods	Retinal photography	wider retinal venular caliber could predict stroke
Kovarnik et al. (2016),	32 patients	Borderline coronary stenosis	IVUS-VH	OCT	plaque indices obtained by IVUS-VH correlate with retinal layer thicknesses
Adzhemain et al. (2016)	55 ATH; 25 control	Atherosclerosis	Ultrasonography of carotid arteries	Retinal photography	Wider retinal venular caliber in patients with atherosclerosis

Seidelmann et al 2016	ARIC	Coronary heart disease events; Ischemic strokes; Heart failure events; Death		Fundus photography	Narrower retinal arterioles and wider retinal venules are associated with negative cardiovascular outcomes
Yang et al. (2016)	A sub-population of Kailuan study	Atherosclerotic carotid artery pathology	carotid IMT	Fundus photography; OCT	Thinner retinal artery diameter was associated with increased common carotid artery IMT.
Anyfanti et al. (2017)	87 rheumatoid arthritis (RA) patients and 46 control subjects	Systemic inflammation; Subclinical atherosclerosis; Cardiovascular risk	carotid IMT; 10-year risk of general cardiovascular disease	Nonmydriatic digital fundus photography	CRAE and AVR were decreased in RA patients ; CRAE and AVR were inversely associated with carotid IMT in RA patients; CRAE was correlated with cardiovascular risk score
Heitmar et al. (2017)	36 diabetes mellitus (DM)patients only; 43 CVD only; 37 CVD and DM subjects	Diabetes mellitus; miscellaneous CVD event/risk factors	Miscellaneous diagnostic methods	monochromatic (red-free) fundus images; flicker light provocation	No significant difference in CRAE, CRVE and AVR between these groups; Difference in reaction pattern and lack of arterial constriction in DM
Peña et al.(2018),	90 adolescents with type 1 diabetes	Atherosclerosis; Diabetes	Carotid and aortic IMT	Retinal photography	associations between thicker carotid IMT and wider retinal arteriolar and venular calibers; increased mean aortic IMT was associated with increased arteriolar tortuosity
Chandra et al. (2018),	ARIC	Coronary heart disease; Stroke	Echocardiography	Retinal photography	Narrower retinal arterioles and wider retinal venules were associated with greater LV mass and worse diastolic indices

Retinal imaging provides a low cost, widely available, and non-invasive method for finding signs of systemic diseases at their early stages. An increasing number of studies have found that many systemic diseases including Alzheimer's disease and atherosclerosis can cause geometrical or pathological changes in the retina (Tables 2.1 and 2.2). According to the literature reviewed in this chapter, changes in the vasculature morphology and neural layers of retina are the most common signs of both AD and ATH. These relationships and known plaque accumulation close to vessels walls in the mentioned diseases, motivates the investigation of retinal images focusing on vessels and adjacent tissue regions for finding possible biomarkers.

The majority (if not all) of the studies conducted in this research area so far, have used monochromic or RGB imaging that mostly allow for investigating spatial features of retinal images and thus finding "spatial hallmarks". Spatial features of an object are characterized by gray levels of its pixels, their joint probability distributions, spatial distribution etc. all defined in a two-dimensional space. Having enough spatial image resolution, retinal vasculature parameters i.e. CRAE, CRVE, AVR, tortuosity, fractional dimension, and AV nicking could be measured by well-known image analysis techniques. However, by using 2D or 3D intensity images, still important tissue-related characteristics may remain uncovered. On the other hand, acquiring images using different monochromic wavelengths provides us with the relative variances in intensities across differing wavelengths. In this technique (known as hyper-spectral imaging—HSI), light transmittance, absorption, and scatter are reflected in the spectrum (intensity vs. wavelength plot) of light emitted from the tissue. Over multiple wavelengths, a pixel yields multiple number of light intensities (spectral dimension) so that the whole image comprises a cube of intensity values (More & Vince, 2015). Therefore, using HSI, not only the common spatial features but also "spectral signatures" of biomolecules could be revealed. This helps finding a wider variety of spatial/spectral features for a more accurate investigation of retinal biomarkers of diseases. The purpose of this thesis was to exploit information content of HSI using a novel hyper-spectral retinal imaging device and to extract combination of features from retinal vasculature and adjacent tissue with the goal of identifying biomarkers of AD and ATH.

CHAPTER 3 TECHNOLOGY AND METHODS

3.1 Hyper-spectral retinal imaging

Hyperspectral imaging (HSI) was originally developed for remote sensing and has been explored into numerous application areas including medical imaging. HSI generally covers a large light spectrum with more spectral bands than multispectral imaging (such as RGB). HSI collects spectral information at each pixel of a 2D detector array, thus generating a 3D dataset of spatial and spectral information that form a cube of data. The spectral data at each pixel, enable HSI to identify a signature of pathological conditions. Therefore, HSI has the capability of capturing the detailed spectral differences under different pathological conditions, while multispectral imaging may miss significant spectral information (Lu & Fei, 2014).

The hyperspectral retinal imaging system used in this study is a Metabolic Hyperspectral Retinal Camera (MHRC) developed by Optina Diagnostics (Montreal, Canada). It consists of an electronically tunable laser source (TLS) coupled to a custom-built mydriatic fundus camera. The TLS transmits safe light at different wavelengths within a spectral range covering visible to near-infrared with a narrow bandwidth (~2 nm). An automatic spectral calibration system is used to achieve precise (<1 nm) and rapid wavelength selection. The instrument is capable of imaging the retina at several monochromatic illumination wavelengths (450-900 nm) on a field-of-view of more than 30° in a few seconds. Each pixel corresponds to a region smaller than 10 x 10 μm2 on the retina with an exposure time per frame of 10 ms in the reflectance mode. Thus, a hyperspectral cube of 91 images from 900 to 450 nm in steps of 5 nm can be obtained in less than 1 second.

Each Hyper-spectral image was comprised of 91 gray-scaled images of 1288*1288 pixels stored as a cube of data (Matlab H5 file) generating 1288*1288*91 single values yielding a total data volume of around 600MB. As Figure 3-1 illustrates, retinal images are sequentially obtained for different wavelengths in order to build a hyperspectral cube of data. After image registration to correct for eye movements that may arise during acquisition, a spectrum is obtained for each pixel of the image. Having spectral intensity values at each pixel, not only the anatomical structures could be observed (similar to conventional retinal imaging), but also spectral signatures could be extracted to localize and quantify specific chromophores of known absorption spectra in the fundus.

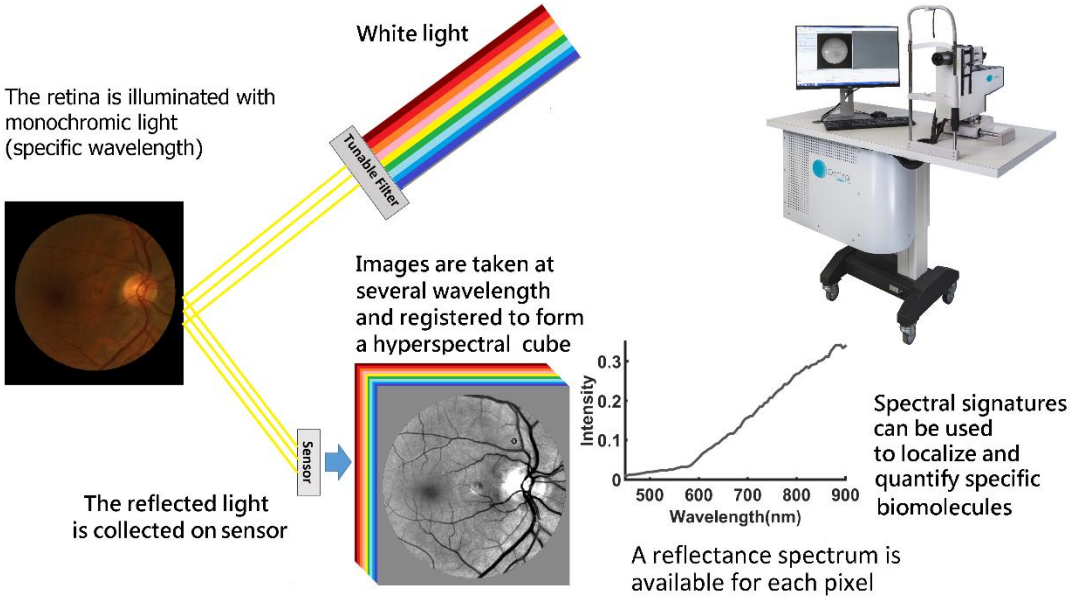

Figure 3.1 Schematic of the Metabolic Hyper-Spectral Retinal Camera used for acquiring the images.

3.2 Retinal image analysis

3.2.1 Normalization and registration

Due to spatial and spectral variations that may arise in light source intensity and system optics, raw data cubes (C_{eye}) were normalized using equation 3-1. White (w), dark (d) and baseline (b) images were recorded prior to human acquisition. The white cube was measured by imaging the surface of a material with high diffuse reflectance (Spectralon; Labsphere, Inc., North Sutton, NH) through a triplet lens replicating the optical properties of the eye. The baseline cube is measured by image acquisition of a light trap (beam dump) placed at the position of the eye to image the parasitic reflections caused by the camera. The dark images are obtained when the shutter is closed and no light is reaching the sensor. Images were corrected for illumination power (P) as shown in equation 3-1. More details about the image normalization are explained in (Patel, Flanagan, Shahidi, Sylvestre, & Hudson, 2013).

(3-1)

$$I_{norm} = \frac{\frac{C_{eye} - I_{d,eye}}{P_{eye}} - \frac{C_{b,eye} - I_{d,eye}}{P_{b,eye}}}{\frac{C_w - I_{d,w}}{P_w} - \frac{C_{b,w} - I_{d,w}}{P_{b,w}}}$$

After normalization, each image of the cube was spatially registered with the previous one to correct wavelength-dependent optical deformations (scaling) and eye movements (translation and rotation) which may occur during the HSI acquisition. The reflectance spectrum generated at each pixel is then available to be analyzed to identify spectral signatures associated with chromophores of interests (Desjardins et al., 2016).

3.2.2 Arterioles and venules segmentation

As mentioned in Chapter 1 and 2 many diseases including AD and ATH manifest themselves in retinal arterioles and venules. Therefore, automatic vessels segmentation and arterioles/venules (AV) classification is an important preprocessing step to any consequent image analysis, specifically when we need to process a large number of retinal images. In the following sections, the algorithms used for vessels' segmentation, AV classification, and an auxiliary graphical user interface developed for this purpose will be described.

Vessels segmentation

Based on the difference between the intensity of the vessels and the background retina at 570 nm, we designed a two-phase segmentation method based on a top-hat transformation. A first phase was optimized to segment fine-vessels (vessels with diameters of less than about 10 pixels or 82μm). In this phase the vessels' background was estimated by image opening with a disk-shape structuring elements of size 5 followed by Wiener filtering. The background was then subtracted from the original image to extract the vessels. Opening image *I* by a structuring element *H* is a morphological erosion of *I* by *H* followed by a dilation (equation 3-2).

$$I \circ H = (I \ominus H) \oplus H \tag{3-2}$$

Detecting fine vessels requires a sharper image (high-pass filtered) while coarse vessels (diameters of more than 10 pixels) could be recovered without sharpening.

In the second phase, we focused on the vessels with diameters larger than 10 pixels (without using Wiener filter) and used opening with a disc-shape structural element of size 10. False positives appeared as very small connected components that were unlikely to be parts of the vessels. They were removed after combination of the two phases to obtain the final segmentation. Figure 3-2 shows a typical result along with the corresponding outputs of phases 1 and 2.

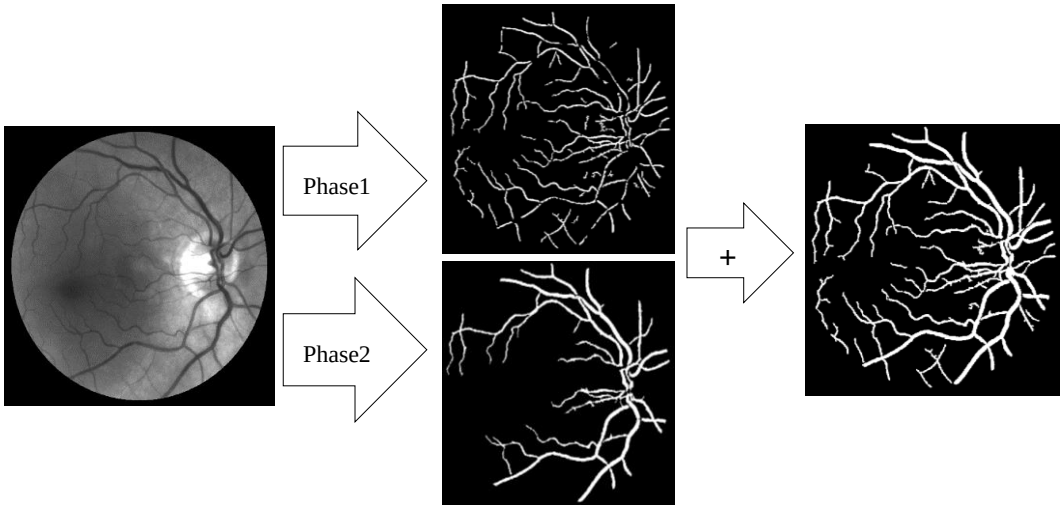

Figure 3.2 Two-phase vessel segmentation of a sampled image at 570nm

AV classification

Since arterioles are more oxygenated than veins, having hyperspectral images of the retinal vessels, it is possible to use the difference between the absorption spectra of oxy (HbO) and deoxyhomoglobin (Hb) as a main feature to build a classifier to discriminate arterioles from venules. In our hyperspectral images, the mentioned difference affects the spectral signatures of the pixels corresponding to arterioles and venules as illustrated in Figure 3.3. The signals shown in the Figure 3.3 (c) are measured after the a spatial Gaussian high-pass filter with size and standard deviation of 300 and 200 pixels respectively to emphasize the difference in the spectra of arterioles and venules. It should be noted that the mentioned filtering deforms the spectra of the original chromophores; however, this was not an issue in a classification task which did not aim to quantify chromophores as described below.

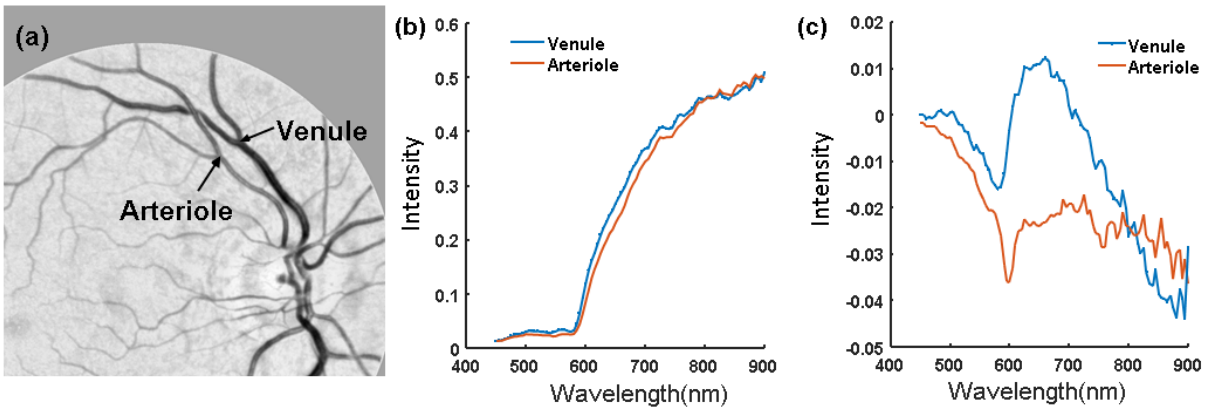

Figure 3.3 Difference between spectra of pixels located in an arteriole and a venule in retina; (a) positions of two pixels associated with an arteriole and a vein, image obtained at 600 nm; (b) spectral signals of the two pixels before Gaussian high-pass filtering; (c) spectral signals of the two pixels after a Gaussian high-pass filtering

We used the discriminating signals associated with arterioles and venules (Figure 3.3-c), and applied machine learning to obtain a method for AV classification. To improve upon the simple procedure, we tried different supervised techniques to find a more accurate AV discrimination approach. To provide training sets, a graphical user interface (GUI) was developed so that domain experts could label the regions of interest of arterioles, venules and background tissues, as the three classes of "arterioles", "venules", and "other". Three different classifiers were trained using the training sets: Linear and Quadratic Discriminant Analysis (LDA/QDA) and a supervised Neural Network. To choose an effective training set, we focused on several spectral bands around 550-900 nm. Amongst the investigated bands, 550 – 725 nm was seen to result in a higher accuracy for AV classification (detail of the method will be given in later in Section 3.2.5). Since our HSI were acquired with a 5nm-step, a spectral pixel has 36 different intensity values for each spatial location in the mentioned band. Accuracy of the classifier was validated against hand segmented vessel masks created by domain experts as gold standards. Among the investigated classifiers, LDA yielded higher classification accuracy.

Despite good performance, we observed a mix between classes in most of the small and some medium-sized vessels, mostly venules (i.e. some vessel segments contained pixels of both classes of arterioles and venules). To resolve this problem, we made use of the fact that pixels belonging to a vessel segment do not change classes between two crossings. Based on this idea, an algorithm

was used to uniquely identify the class of vessel segments between crossings and correcting misclassified pixels.

Finally, to provide explicit examples, the results of AV classification on two sample retinal images are shown in Figure 3-4 where the AV maps is superimposed on the original image at wavelength 570 nm. In this Figure, the output of LDA classification and the corrected AV maps are shown in the first and second columns respectively. The corresponding gold standards obtained by manual segmentation are shown in the third column. We observe that poorly classified vessels (i.e. those that contain a majority of classified pixels below threshold) are removed from the enhanced image. Although it decreases the overall number of classified pixels, it increases the accuracy of the classification by removing those pixels from the final AV map that the algorithm does not have enough confidence about their classes.

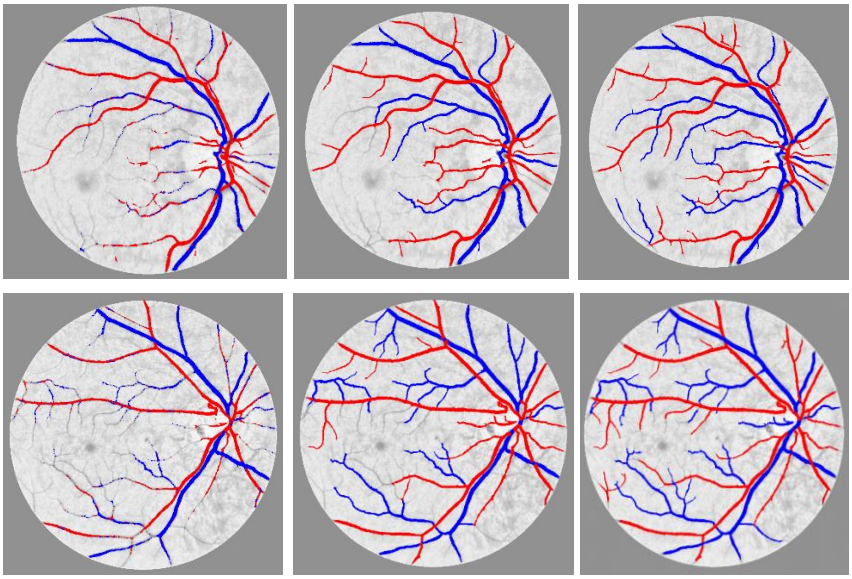

Figure 3.4 Result of automatic AV classification algorithm for two retinal images. Left column shows the images after AV classification and before automatic correction, middle column shows the corresponding images after automatic correction. Right column shows the gold standards determined by a domain expert using a graphical user interface.

Graphical user interface

Regarding the very precise image analysis required for investigating retinal biomarkers (e.g. vessels' tortuosity, diameter and texture measurements), we integrated our AV classification algorithm in to a GUI with extensive correction tools so that the results of automatic segmentation of arterioles and venules could be corrected manually for any classification error. Figure 3-5 illustrates a schematic view of this GUI.

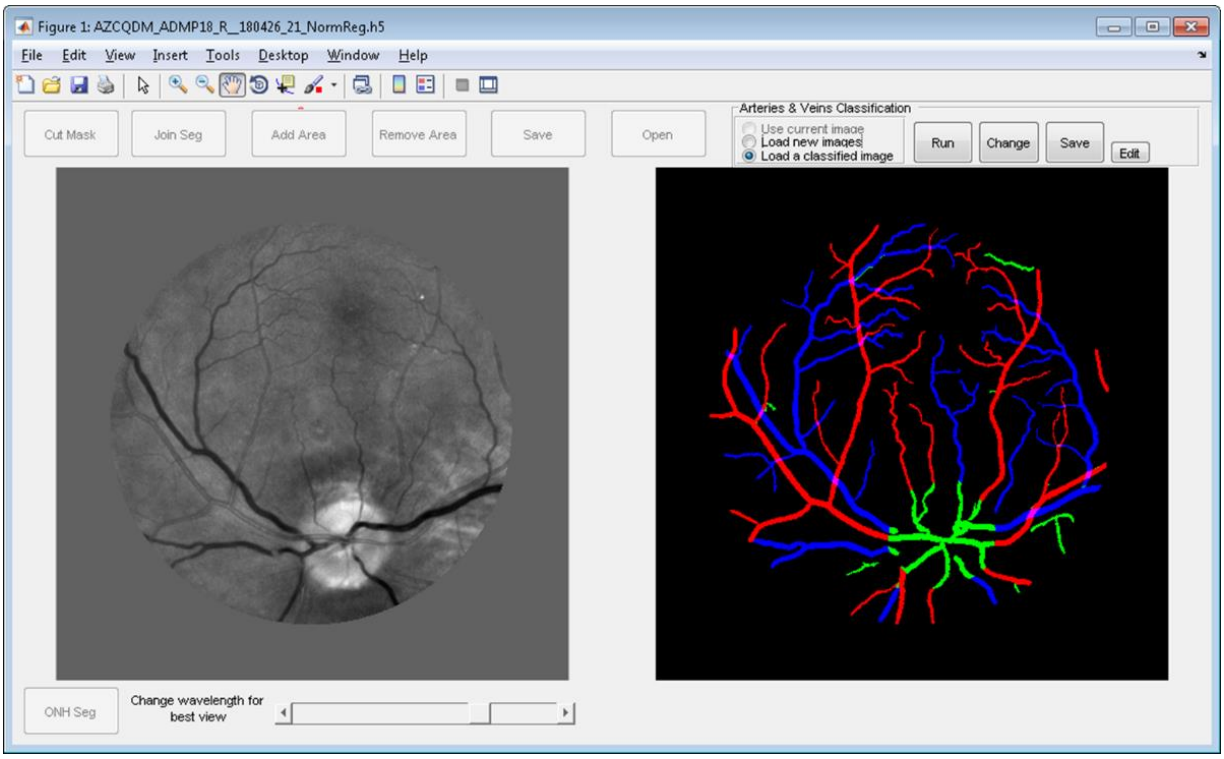

Figure 3.5 GUI developed for manual correction of AV classification errors

3.2.3 Tortuosity and diameter measurements

As described in Section 2, many neurodegenerative and cardiovascular diseases including AD and ATH affect retinal vessels by changing their tortuosity and/or diameters.

In this Section, details of the methods used in this thesis to calculate vessels tortuosity and diameters will be given.

Tortuosity measurements

Abnormal retinal tortuosity is identified as formation of curvatures along the blood vessels. Ophthalmologists believe that these buildups are due to the natural capabilities of the vessels to

avoid or to adapt to certain changes in the body including long-term illnesses and chronic conditions. (Abdalla, Hunter, & Al-Diri, 2015; Dougherty & Varro, 2000; Koprowski et al., 2012; Owen et al., 2009; Patasius, Marozas, Jegelevicius, & Lukosevicius, 2005; Ţălu, 2013). There has been many efforts in the literature to develop automated tortuosity measurement. They can be divided in to two general categories: distance-based and curvature-based methods (a review on these studies is given in (Abdalla et al., 2015).

Distance-based metrics are simply focused on computing the length of the path that the vessel segment or curve takes, known as the arc (L_c); and the distance (e.g. Euclidean) between the two end points of the vessel segment, known as the secant or chord (D), then tortuosity (T_{AOC}) is estimated by taking the ratio between those two lengths as shown in Equations 3-3. This method is also known as Arc over chord ratio (AOC). The measure has zero value for a straight vessel segment and increasing positive value for segments as they become more tortuous. Figure 3-6 shows how we calculated this metrics for a sample vessels segment.

(3-3)

$$T_{AOC} = \frac{L_c}{D} - 1, \qquad D = \sqrt{(x2 - x1)^2 + (y2 - y1)^2}$$

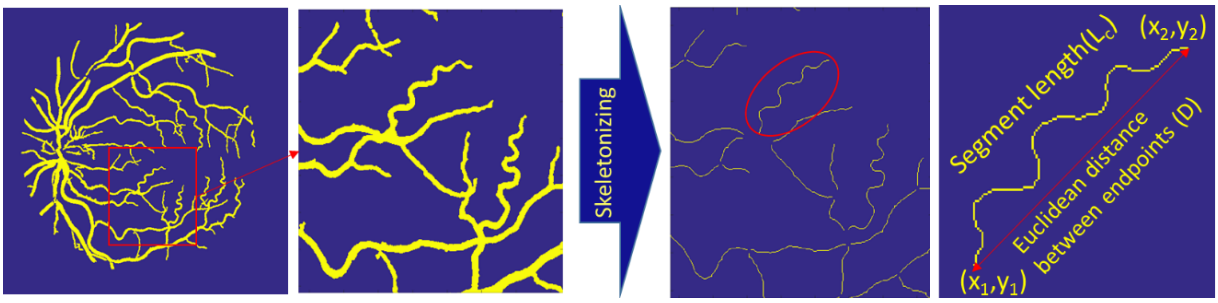

Figure 3.6 Simple tortuosity measurement of a vessel segment using arc and chord

Curvature-based metrics are more accurate and complicated than the distance-based metrics. Curvature is the amount by which a curve deviates from being straight. Geometrically, the curvature κ specifies how fast the tangent vector to the curve changes its direction. If a curve remains close to the same direction, tangent vector changes slightly and the curvature is small; where the curve goes through a sharp turn, the curvature is large. As a precise definition, if we estimate a vessel segment S in a digital image, by a spline (a continuously differentiable function

defined piecewise by polynomials), where *S* is represented by center line pixels (x_1, y_1), (x_2, y_2), ... , (x_{n-2}, y_{n-2})), (x_{n-1}, y_{n-1}), (x_n, y_n) , if the spline is given in the Cartesian coordinates as γ(t) = ($x(t)$, $y(t)$), the curvature κ at point *t,* i.e. κ (t), can be estimated by Equation 3-4 , where primes refer to derivatives d/dt with respect to the parameter *t*.

(3-4)

$$\kappa(t) = \frac{|x'(t)y''(t)-y'(t)x''(t)|}{(x'(t)^2 - y'(t)^2)^{\frac{3}{2}}}$$

Tortuosity of vessel segment S could be computed as the total curvature along S with respect to its length. Total curvature of S can be computed from point-wise curvature, κ (t) in various ways. For example, as the integral of the curvature (Equation 3-5), integral of the squared curvature (Equation 3-6), or an integral of square of derivative of curvature (Equation 3-7).

(3-5)

$$T_1 = \int_{t_0}^{t_n} \kappa(t)dt$$

(3-6)

$$T_2 = \int_{t_0}^{t_n} \kappa(t)^2 dt$$

(3-7)

$$T_3 = \int_{t_0}^{t_n} (\kappa'(t))^2$$

Tortuosity also has been estimated in the literature by normalizing the total curvature by the vessel segment's arc length. It this thesis, after investigating simple tortuosity measurement (AOC) on our datasets, in order to yield an appropriate level of precision, we used one of the state-of-the art methods (Patasius et al., 2005) which has been extensively used in the literature for computing retinal vessels' tortuosity. It estimates the tortuosity as the integral of square of derivative of curvature, divided by the length of the arc of the vessel segment (Equation 3-8). In this case, tortuosity of a completely straight vessel segment is estimated to be 0.

(3-8)

$$T = \frac{\int_{t_0}^{t_n} (\kappa'(t))^2}{L_c}$$

ONH detection

Majority of the retinal vessels diameter measurements reported in the literature calculated the vessels diameters for the vessel segments located in three well-known retinal zones (A, B, and C). These zones are defined based on the position of the ONH in the retinal image. Therefore, we developed an algorithm to detect ONH in our hyperspectral images to be able to perform vessels diameter measurements subsequently.

Retinal zone A is region from 0 to0.5 ONH diameter away from the ONH margin, zone B is the region from 0.5 to 1 ONH diameter away from the ONH margin, and zone C is defined as the region from 0.5 to2 ONH diameters away from the ONH margin. Figure 3.7 shows ONH detected and marked as red circles in two different images (taken at 570 nm) and different retinal zones in another images.

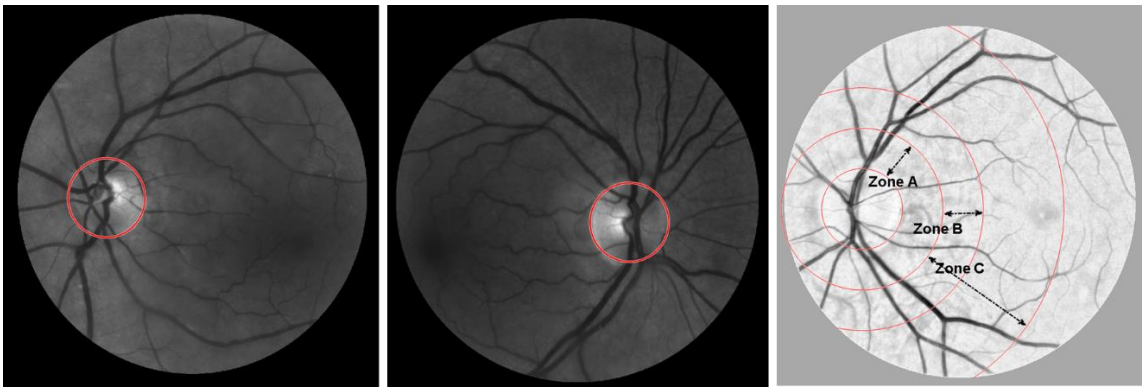

Figure 3.7 Results of ONH detection algorithm in two samples (left and middle). Retinal zones illustrated in the right side image

The developed ONH detection technique in this thesis, simply considered ONH as a circle (There are more precise ONH detection algorithms in the literature but in our application i.e. determining retinal zones for vessels' diameter measurement, we did not require that precision). The algorithm is based on an improved version of circle detection using Circle Hough Transform (CHT). This

method could be formulated as a convolution whose binary mask coefficients are set on the circle boundary and zero elsewhere. CHT filter kernels for single circle detection (O_{SC}) and annulus detection (O_A) are described by equations 3-9, 3-10 respectively.

(3-9)

$$O_{SC}(m,n)=\begin{cases}1 & iff\ (R-0.5)^2 < m^2+n^2 < (R-0.5)^2 \\ 0 & otherwise\end{cases}$$

(3-10)

$$O_A(m,n)=\begin{cases}1 & iff\ R_{min}^2 < m^2+n^2 < R_{max}^2;\ R_{max} > R_{min}+1 \\ 0 & otherwise\end{cases}$$

In Atheron et al. (Atherton & Kerbyson, 1999), the CHT kernels are improved to be scale invariant and robust at low signal-to-noise ratio. This method is the fundamental basis of our proposed technique for ONH detection. We also took the advantages of hyperspectral nature of our images to improve the accuracy of the ONH detection:

In most of our hyperspectral images, in images acquired at 500 nm, the ONH appeared as a bright circle which is detectable by the mentioned method after applying an average filter (to smooth the edges of the vessels inside the ONH that might be led to miss detection of the ONH). However, in some other acquisitions, there was not an enough contrast of ONH at 500 nm. For this reason, other wavelengths in which the ONH has a higher contrast were considered. The algorithm investigated wavelengths at which ONH is either brighter than the background (e.g. 705 nm to 455 nm) or darker than the background (e.g. 845 to 900 nm) using appropriate kernels. The algorithm continues investigating different images within the HSI cube until it finds a circle (bright or dark) with the higher kernel response with a radii in the range of an ONH's radius in our images (i.e. 100 to 200 pixels). The algorithm is accurate for almost 95% of the cases. However, it failed for very noisy images and also the images in which the ONH did not completely appear inside the FOV. The results were then checked visually by a domain expert to correct any misdetection.

Vessels' diameter measurement

As mentioned in Chapter 2, changes in retinal vessels diameter could be hallmarks of neurodegenerative and/or cardiovascular disorders. Therefore, in addition to an accurate AV

segmentation tool, we needed to calculate retinal vessel's diameters based on the AV segmentation masks created previously.

For each vessel segment, one third of its centerline pixels were selected. Then, the shortest line connecting each centerline pixel to the border of the vessel segment was calculated as the diameter of the vessel segment at that pixel. Average diameter of the vessel segment at all selected centerline pixels was considered as the diameter of the whole vessel segment. Vessel diameter at a specific zone was defined as the maximum diameter of the vessel segments within that zone. Figure 3.8 shows how the diameter of a venule segment in zone A of a retinal image (acquired at 575 nm) is calculated.

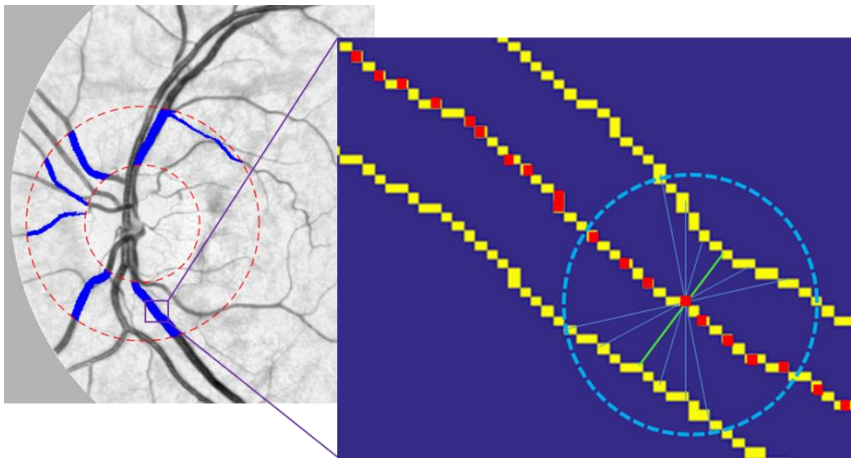

Figure 3.8 Schematic of calculating the diameter of a venule segment in zone A of a retinal image. In the right side of the figure, pixels at centerline and borders of the segment are shown in yellow. Random pixels chosen at the centerline are shown in red. Some of the lines passing through one of the centerline pixels are shown in purple. The shortest line (i.e. the diameter of the vessels at a specific centerline pixel) is shown in green.

3.2.4 Texture analysis

Texture measurements quantify the relationships between neighboring pixels' values. Textures describe the local spatial (and/or spectral) arrangement of reflectance values that may be used for further processing. Spectral relationships are not necessarily correlated with spatial data for a given class, thus using them could improve classification accuracy (Hall-Beyer, 2017). Within a

neighborhood of pixels, texture has three elements: tonal difference between pixels, the distance over which this difference is measured, and directionality. These are also referred as smoothness, coarseness, and regularity (Gonzalez & Woods, 2006).

The Grey Level Co-occurrence Matrix (GLCM) is a numerical representation of texture (suitable for computer-based classification) that was provided by Haralick in the 1970s (Robert M. Haralick, Shanmugam, & Dinstein, 1973). GLCM textures have been proved to be successful in a wide variety of classification activities, increasing classification accuracies (Hall-Beyer, 2017). Haralick's GLCM textures are co-occurrent or second order. It is capable of accounting for all three texture elements. The GLCM is simply related to the probability of finding a pixel with gray-level *i* at a distance *d* and directionality α from a pixel with a gray level *j*. In a 2D image, distance is usually defaulted to the image's spatial resolution (1 pixel) and α is usually defaulted to omnidirectional unless they are the subject of the investigation.

Many statistical texture measures can be calculated from the GLCM. Haralick (1979) suggested 14 statistics. Most of these statistics within a given group are strongly correlated. For example, GLCM variance, being a measure of variability, is commonly closely correlated to the contrast. Thus, common software have built-in function for a subset of texture measures. MATLAB has built-in code for four of them i.e. contrast, correlation, energy, and homogeneity ("Properties of gray-level co-occurrence matrix; MATLAB graycoprops," n.d.). Table 3.1 describes the formula of the four texture measures. $P_{i,j}$ is the probability of values *i* and *j* occurring in adjacent pixels in the original image within a neighborhood. *i* and *j* are the labels of the columns and rows (respectively) of the GLCM. Because of the construction of the GLCM, *i* refers to the value of a target pixel, and *j* is the value of its immediate neighbor (rook's case).

In this thesis, localizing the Aβ plaques (a possible retinal biomarker of AD) in the retinal images was confounding due to their small size (mostly less than10 μm—(Koronyo et al., 2017)) compared to the optical resolution of the retinal imaging system and the lack of sufficient information about the spectral signature of the plaques in vivo in human. Therefore, we were motivated to use texture analysis with the aim of improving the accuracy of the classification of AD and control subjects by investigating possible textural changes in vessels and tissue around them.

Table 3.1 Statistical texture measures and calculation formula

Texture measure name	Calculation formula
Mean (GLCM Mean)	$\mu_i = \sum_{i,j=0}^{N-1} i(P_{i,j});\ \mu_j = \sum_{i,j=0}^{N-1} j(P_{i,j})$
Variance (GLCM variance)	$\sigma_i^2 = \sum_{i,j=0}^{N-1} P_{i,j}\,(i-\mu_i)^2;\ \sigma_i^2 = \sum_{i,j=0}^{N-1} P_{i,j}\,(j-\mu_i)^2$
Contrast	$\sum_{i,j=0}^{N-1} P_{i,j}(i-i)^2$
Correlation	$\sum_{i,j=0}^{N-1} P_{i,j}\left[(i-\mu_i)(i-\mu_j)/\sqrt{(\sigma_i^2)(\sigma_j^2)}\right]$
Energy (square root of angular second moment—ASM)	$\sqrt{\sum_{i,j=0}^{N-1} {P^2}_{i,j}}$
Homogeneity	$\sum_{i,j=0}^{N-1} \frac{P_{i,j}}{1+(i-j)^2}$

Regarding the reported small-scaled changes ocuured at endothelial cells and retinal vessels' borders in patients with ATH (reviewed in Chapter 2), we also used GLCM texture measurements on retinal vessels and adjacent tissues to detect possible hallmarks of ATH in retina.

We extracted four different texture measures i.e. contrast, correlation, energy, and homogeneity from both spatial and spectral directions of our retinal HSIs. In this way, we not only investigated gray levels of pixels and their variations belonging to the spatial distribution of backscatters in retinal tissues, but also the relative variances in intensities across differing wavelengths. In this technique, we aimed to investigate both the common spatial features and "spatial/spectral signatures" of biomolecules to find retinal biomarkers of AD and ATH.

To extract GLCMs from different directions of a retinal HSI cube, after fetching the region of interest (e.g. around arterioles, venules, ONH, macula, etc.) by an appropriate masking, we formed spatial, spectral, and spatial/spectral GLCMs by taking the directions along x (and/or y), z, and

diagonal through x and z coordinates of the cube respectively. Figure 3.9 (left) illustrates directions used for extracting texture measures from a sample HSI.

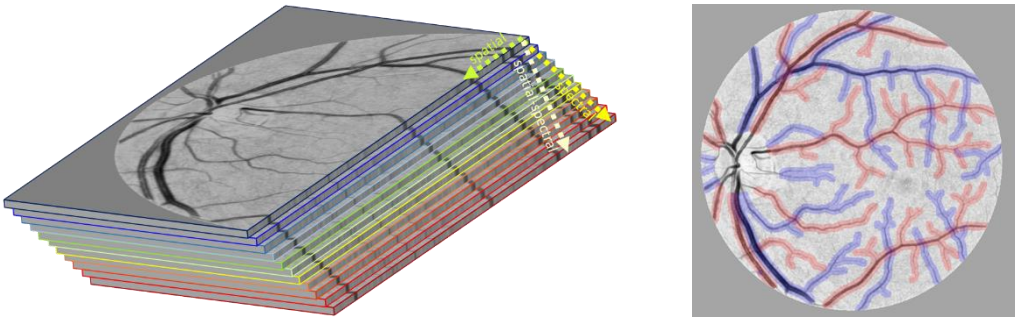

Figure 3.9 Left: Different directions used for computing GLCM on a 3D representation of a hyperspectral retinal image; Green, white, and yellow arrows show the spatial, spectral and spatial/spectral directions. (Colors and the amount of light spectrum shown in the figure is for demonstration purpose and is not part of the main image). Right: masks showing arterioles (in red) and venules (in blue) and around tissues (≈ 80μm away from the vessels' border).

In order to calculate texture measures of an HSI, in addition to the full range of the available spectrum (i.e. 450-900 nm), the two ends of the spectrum (i.e. 450-550 nm and 700-900 nm) were also separately investigated. The spectral range 450 to 550nm, is known as the spectral region most likely to be affected by scattering from Aß aggregates in the retina. Moreover, the spectral range 700 to 900nm is the spectral region least likely to be affected by the transmission of the anterior segment of the eye. The texture measures were extracted from different anatomical areas of the retina including arterioles, venules, regions around arterioles and venules (separately). Figure 3.9 (right) shows the spatial demonstration of the regions for which the texture measures were extracted from the sample HSI shown in the left side.

3.2.5 Statistical analysis and machine learning

The data processing was carried out with Matlab (MathWorks, USA) toolboxes. In this section, methods used for different statistical analysis within the context of this thesis will be described.

Linear discriminant analysis (LDA)

LDA has been widely used in the literature for pattern recognition and machine learning to find a linear combination of features to separate two or more classes of objects in multi-spectral images (Bandos, Bruzzone, & Camps-Valls, 2009; Lin, Wang, Wang, & Sun, 2010; Peng & Luo, 2016).

We used LDA for both AV classification (Section 3.2.2) and discriminating atherosclerosis subjects from healthy controls over a combination of image features. Following, a brief explanation of the application of LDA in classifying arterioles and venules based on hyperspectral image data will be given.

As previously mentioned, each pixel in a HSI cube comprises of a vector of spectral reflectance values, in AV classification we used LDA to discriminate between arteriole pixels and venule pixels based on their spectral intensity value (Figure 3.3). If we assume a set of *N* spectral pixels $\{p_1, p_2, ..., p_N\}$ each having intensity values corresponding to *N* different wavelengths (i.e. N-dimensional space) and also assume that each pixel belongs to one of *c* classes $\{X_1, X_2, \ldots, X_c\}$ (e.g. arterioles, venules, background etc.). The between-class and within class scattered matrices (i.e. estimation of the covariance matrices) are defined as equation 3-11 and 3-12 respectively.

(3-11)

$$S_b = \sum_{i=1}^{c} Ni(\mu_{i-}\mu)(\mu_{i-}\mu)^T$$

(3-12)

$$S_w = \sum_{i=1}^{c} \sum_{p_{k\in X_i}} (p_k - \mu_i)(p_k - \mu_i)^T$$

Where N_i is the number of samples in class X_i, and μ and μ_i are the total sample mean vector and the mean sample of class X_i respectively.

LDA looks for directions in which data points (the spectral pixels in our application) of different classes have the maximum between-class distances while requiring data points of the same class to be as close as possible to each other. This is achieved by maximizing the ratio of between-class against within-class scattered matrices (equation 3-13).

(3-13)

$$W^* = \arg\max_W \frac{|W^T S_b W|}{|W^T S_w W|}$$

To prevent S_W being singular, one can substitute S_W with $S_W + \lambda I$. The optimal transformation matrix W^* is then computed by applying an eigen-decomposition on the scatter matrices of the given training data.

Quadratic discriminant analysis (QDA) on the other hand, can learn quadratic boundaries (not just linear boundaries as LDA does). QDA like LDA assumes that the measurements from each class are normally distributed. However, in QDA there is no assumption that the covariance of each of the classes is identical. QDA, tend to fit data better than LDA, because it allows for more flexibility for the covariance matrix but it has more parameters to estimate. If there are many classes and not so many measurements, it could lead to inaccurate classification (James, Witten, Hastie, & Tibshirani, 2013).

In addition to AV classification as described earlier in this section, we used LDA for classifying retinal images of atherosclerosis subjects (n=30) and control subjects (n=30). In that context, LDA was used over a set of 7 retinal features comprised of arteriole diameter in zone B and 6 texture measures extracted from spectral and spatial/spectral directions of HSI cubes (details of the features will be explained later in this chapter). Classifiers evaluated other than LDA, were QDA, and SVM with linear and Gaussian radial basis function kernels. The rationales for choosing the features and the classifiers will be given in this chapter.

Feature selection

One of the important prerequisites for an effective classification is feature selection (also called feature subset selection). Feature selection is referred to filter out irrelevant, noisy, misleading or redundant features. Feature selection is therefore a combinatorial optimization problem that tries to identify those features which minimize the generalization error (Rückstieß, Osendorfer, & van der Smagt, 2011). A common method of feature selection is sequential feature selection (SFS). This method has two components: a criterion and a sequential search algorithm. The criterion (also called objective function) is a quantity that the method seeks to minimize over all feature subsets. Common criteria are the mean squared error (for regression models) and misclassification rate (for classification models). A sequential search algorithm, on the other hand, adds or removes features

from a candidate subset while evaluating the criterion. Sequential searches move in only one direction i.e. growing the candidate set (sequential forward selection) or shrinking the candidate set (sequential backward selection) because a complete comparison of the criterion value over all subsets of the feature set is not feasible.

In this thesis, for discerning Aß+ from Aß- subjects in a first step, two types of features were extracted from HSI cubes: vasculature features and texture measures. Vasculature features included arterioles and venules tortuosity and diameters (as described in Section 3.2.3). Texture measures included standard texture measures i.e. contrast, correlation, energy, and homogeneity extracted from arterioles, venules, and adjacent regions.

To combine features into a single biomarker, a sequential feature selection was conducted on the set of initial features mentioned above and then, eight features with highest validation criterion were selected. The validation criterion was evaluated through a 10-fold cross-validation of initial set of features with different training and testing subsets. Table3-2 summarizes the selected features and their attributes.

Table 3.2 Features yielded by sequential feature selection to discriminate AD from control subjects

Feature name	**Feature type**	**Anatomical region**	**Band(nm)**	**Direction**
Tortuosity	vasculature	venules	-	-
Diameter	vasculature	arterioles – zone A	-	-
Contrast	texture	arterioles and around	450-550	spectral
Energy	texture	arterioles and around	450-550	spectral
Energy	texture	arterioles	700-900	spectral
Contrast	texture	arterioles and around	450-550	spatial/spectral
Correlation	texture	arterioles and around	450-550	spatial/spectral
Homogeneity	texture	arterioles and around	450-550	spatial/spectral

The same rationale was used for selecting features for discriminating ATH from control subjects. Vessels' tortuosity, diameter and texture measures were calculated for both groups of data (i.e. ATH and CTL) as an initial set of features. In the next step, features that showed significant difference (uncorrected) between groups (t-test, $p<0.05$) were chosen for further combined analysis in a classification task. Significant vasculature feature in ATH study was arteriole diameter in zone

B. Texture measures associated with spatial areas covering both arterioles and venules and adjacent regions showed significant differences between the two groups. Seven features were selected after applying sequential feature selection on the set of initial features. Table 3.3 shows the selected feature and their attributes.

Table 3.3 Features yielded by sequential feature selection for discriminating ATH from control subjects

Feature name	Feature type	Anatomical region	Band	Direction
Diameter	vasculature	arterioles – zone B	-	-
Energy	texture	arterioles and around	450-550	spectral
Correlation	"	venules	450-550	spectral
Energy	"	venules and around	450-550	spatial/spectral
Correlation	"	arterioles	700-900	spatial/spectral
Contrast	"	venules	700-900	spatial/spectral
Correlation	"	venules	700-900	spatial/spectral

Support vector machine (SVM) for binary classification

Where data points are represented as n-dimentional vectors, a linear SVM classifies data by finding hyperplanes that separate data points of one class from those of the other class. The best hyperplane for an SVM means the one that represents the largest separation or margin (space that does not contain any observations) between the two classes. Therefore, we must choose the hyperplane so that the distance from it to the nearest data point on each side is maximized. The support vectors are the data points that are closest to the separating hyperplane (Figure 3.10).

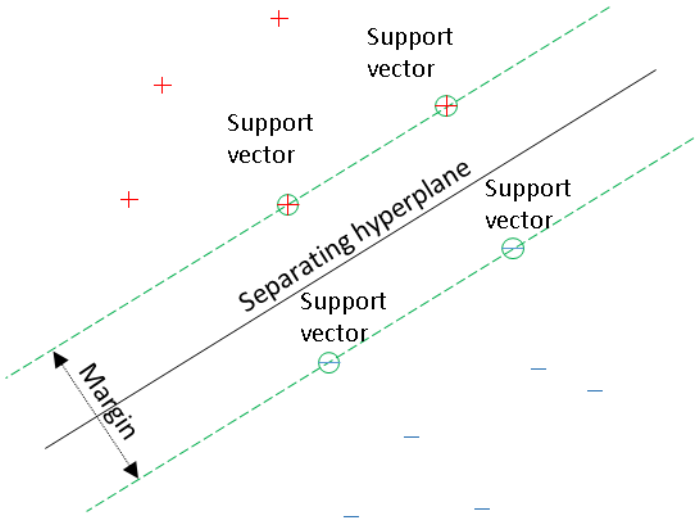

Figure 3.10 An illustration of support vectors, margin, and best hyperplane

If x_j are observations (data for training) and y_j are the corresponding categories (or labels), where for some dimension d, the $x_j \epsilon R^d$, and $y_j = \pm 1$, the equation of any hyperplane can be written as equation 3-14.

3-14

$$f(x) = x'\beta + b = 0$$

Where $\beta \epsilon R^d$ and b is a real number. The vector β contains the coefficients that define an orthogonal vector to the hyperplane. The best hyperplane (i.e. decision boundary) could be obtained by finding β and b that minimize $\|\beta\|$ such that for all data points (x_j, y_j), $y_j f(x_j) \geq 1$. The support vectors are xj on the boundary, such that for which $y_j f(xj)=1$. The problem of minimizing $\|\beta\|$ is a quadratic programming problem. Finding the optimal solution $(\hat{\beta}, \hat{b})$, one can classify a vector z by equation 3-15 where $\hat{f}(z)$ is the classification score that is corresponding to the distance z from the hyperplane. If the training data is linearly separable, the optimal hyperplane maximizes a margin surrounding itself. If the training data is not linearly separable, the objective is the same, but the algorithm considers a penalty on the length of the margin for every observation that is on the wrong side of the boundary (Cristianini & Shawe-Taylor, 2000; Hastie, Tibshirani, & Friedman, 2009).

3-15

$$class(z) = sign\left(z'\hat{\beta} + \hat{b}\right) = sign(\hat{f}(z))$$

For classifying Aß+ and Aß- subjects, we used a linear SVM classifier. Using Principal component analysis on eight features explained in Table 3.2, seven components were chosen for the final SVM classification. Following, the rationales for choosing the classifier and principal components will be described.

Selecting the classification model and principal components

For selecting classification models in both studies (i.e. AD and ATH) we investigated four models: LDA, QDA, linear SVM, and SVM with radial basis function kernel (rbf). For possible dimensional reduction, principal component analysis (PCA) was applied on the final set of features described in Tables 3.2 and 3.3. The final classification models were selected based on minimum cross validation losses. To this end, firstly principal components of the features were calculated. Then, 10-fold cross validation loss values were repeatedly calculated for all methods/principal components. Finally, method and principal components associated with the minimum cross validation loss were chosen. Algorithm 3.1 describes the procedure of choosing classification model and principal components in details.

Algorithm 3.1 Choosing classification method and principal components

Require: M={LDA, QDA, linear SVM, rbf SVM}; set of the investigated methods

PC= {$PC_{1..}PCn$}; set of principal component of *n* features

p=number of repetition (used to obtain a distribution of cross validation losses values to calculate mean and standard deviation of cross validation losses)

```
Calculate PC;
for all m_i ϵ M do
    for j= 1 to n do
        for k= 1 to p do
            Calculate 10-fold cross validation loss of m_i considering PC_1
            to PC_j inclusively;
        end for
    end for
    Calculate mean and sdv. of cross validation losses of m_i for PC_1 to PC_n
    (inclusively);
end for
Choose i,j so that (m_i,pc_j) is associated with minimum cross validation loss;
```

CHAPTER 4 ARTICLE 1: VASCULAR RETINAL BIOMARKERS IMPROVE THE DETECTION OF THE LIKELY CEREBRAL AMYLOID STATUS FROM HYPERSPECTRAL RETINAL IMAGES

Sayed Mehran Sharafi[a], Jean-Philippe Sylvestre[b], Claudia Chevrefils[b], Jean-Paul Soucy[c], Sylvain Beaulieu[e], Tharick A Pascoal[f], Jean Daniel Arbour[g], Marc-André Rhéaume[g], Alain Robillard[h], Céline Chayer[h], Pedro Rosa-Neto[i], Sulantha S. Mathotaarachchi[i], Ziad S. Nasreddine[j], Serge Gauthier[k], Frédéric Lesage*[a,d]

[a] Genie Electrique, Polytechnique Montreal, Montreal, Quebec, Canada, H3C 3A7;

[b] Optina Diagnostics, Montreal, Quebec, Canada, H4T 1Z2;

[c] Montreal Neurological Institute, McGill University, Montreal, Quebec, Canada, H3A 2B4;

[d] Research Center, Montreal Heart Institute, Montreal, Quebec, Canada, H1T 1C8;

[e] Département de médecine nucléaire, Hôpital Maisonneuve-Rosemont, Montreal, Quebec, Canada;

[f] Translational Neuroimaging Laboratory, McGill Centre for Studies in Aging, Douglas Mental Health University Institute, Montreal, Quebec, Canada;

[g] Clinique ophtalmologique 2121, Montreal, Quebec, Canada;

[h] Département de psychiatrie, Hôpital Maisonneuve-Rosemont, Montreal, Quebec, Canada;

[i] Translational Neuroimaging Laboratory, McGill Centre for Studies in Aging Douglas Mental Health University Institute, Montreal, Quebec, Canada;

[j] MoCA Clinic and Institute, Greenfield Park, Quebec, Canada;

[k] Alzheimer's Disease Research Unit, The McGill University Research Centre for Studies in Aging, Montreal, Quebec, Canada;

- This article accepted for publication in the journal of *Alzheimer's & Dementia: Translational Research & Clinical Interventions (TRCI)* from the Alzheimer's Association®.

4.1 Abstract

This study investigates the relationship between retinal image features and β-amyloid (Aβ) burden in the brain with the aim of developing a non-invasive method to predict the deposition of Aβ in the brain of Alzheimer's patients. Retinal images from 20 cognitively impaired and 26 cognitively unimpaired cases were acquired (3 images per subject) using a hyperspectral retinal camera. The cerebral amyloid status was determined from binary reads by a panel of 3 expert raters on 18F-Florbetaben positron-emission tomography (PET) studies. Image features from the hyperspectral retinal images were calculated, including vessels tortuosity and diameter and spatial/spectral texture measures in different retinal anatomical regions. Retinal venules of amyloid positive subjects (Aβ+) showed a higher mean tortuosity compared to the amyloid negative (Aβ-) subjects. Arteriolar diameter of Aβ+ subjects was found to be higher than the Aβ- subjects in a zone adjacent to the optical nerve head. Furthermore, a significant difference between texture measures built over retinal arterioles and their adjacent regions were observed in Aβ+ subjects when compared to the Aβ-. A classifier was trained to automatically discriminate subjects combining the extracted features. The classifier could discern Aβ+ subjects from Aβ- subjects with an accuracy of 85%.

Keywords: Multispectral fundus imaging, Alzheimer, Beta amyloid, Retina, Image processing, Machine learning.

4.2 Introduction

Alzheimer's disease (AD) is a slowly evolving neurodegenerative disorder characterized by cognitive loss that ultimately leads to MaCI a state of major cognitive impairment (MaCI). It is the most common cause of MaCI, affecting millions worldwide. The hallmark histopathological anomalies of AD result from the progressive accumulation of extracellular amyloid plaques (Aβ) composed of amyloid precursor protein (APP) fragments, Aβ peptides, and the intracellular tau tangles, composed of fibrils of hyperphosphorylated tau protein (Masters et al., 2015). Pathological changes can occur up to 20 years earlier than the onset of cognitive decline and brain degeneration has already spread widely by the time the cognitive decline becomes apparent. The National Institute of Aging and the Alzheimer's Association, as well as of the International Working Group on AD recently proposed a research framework based on a set of validated biomarkers linked

amongst others to both types of anomalies that are proxies for AD to define Alzheimer's disease in living people (Jack et al., 2018).

PET imaging with Aβ ligands is the standard non-invasive method for in vivo detection of Aβ plaques in the brain. They can indicate the presence, distribution and quantity of Aβ in the brain. Although the cerebral amyloid status on its own is not specific to AD, there is growing evidence that amyloid PET helps confirm or rule out the diagnosis, and can be useful for the optimization of patient management (Ceccaldi et al., 2018; Grundman et al., 2016; Rabinovici et al., 2017). However, PET with Aβ ligands is an expensive technique of limited accessibility and costs and practical limitations restrain its use for population screening. There has also been significant progress in the area of cerebrospinal fluid (CSF) biomarkers for AD. To date, decreased Aβ42 or Aβ 42/Aβ 40 ratio and high levels of p-Tau are the most accurate, reproducible and informative CSF biomarkers for AD (Kuhlmann et al., 2017; Olsson et al., 2016). However, these require lumbar puncture and standardization has proven to be complex.

The retina is an extension of the central nervous system (CNS) and represents the only part of the CNS which is noninvasively accessible for imaging by optical means. Therefore, the eye has been suggested as a window to the brain offering a unique site to measure biomarkers for neurodegenerative diseases (Javaid, Brenton, Guo, & Cordeiro, 2016; Shah, Gupta, Chatterjee, Campbell, & Martins, 2017).

Spectral domain optical coherence tomography (SD-OCT) has allowed 3-dimentional observation of histological details of the retinal layers and optic nerve with high resolution (4 μm axial resolution). SD-OCT is currently being applied to various CNS neurodegenerative diseases (Kesler, Vakhapova, Korczyn, Naftaliev, & Neudorfer, 2011) by measuring retinal nerve fibre layer loss and has been demonstrated to show nerve fiber anomalies in AD (Berisha, Feke, Trempe, McMeel, & Schepens, 2007; Jindahra, Hedges, Mendoza-Santiesteban, & Plant, 2010; Paquet et al., 2007; Parisi et al., 2001). However, the method may lack specificity, as nerve fiber alterations are also observed in glaucoma, MCI (Paquet et al., 2007) and Parkinson's disease (Jiménez-Jiménez, Alonso-Navarro, García-Martín, & Agúndez, 2014; Lee et al., 2014).

It was reported in the literature that Aβ plaques accumulate in the retina of AD mouse models (Edwards et al., 2014; Koronyo-Hamaoui et al., 2011; Liu et al., 2009; Ning, Cui, To, Ashe, &

Matsubara, 2008; Perez, Lumayag, Kovacs, Mufson, & Xu, 2009), an accumulation also observed in the retina of AD human subjects post mortem (Koronyo-Hamaoui et al., 2011) and in vivo (Shaun Frost et al., 2014; Koronyo et al., 2017).

Optical fluorescence imaging of the retina, with the fluorescent label curcumin, which binds to Aβ plaques with high affinity (Garcia-Alloza, Borrelli, Rozkalne, Hyman, & Bacskai, 2007; Yang et al., 2005), has been proposed as a simple procedure to detect Aβ plaques (Koronyo-Hamaoui et al., 2011) and has recently been tested in vivo in AD subjects (Shaun Frost et al., 2014; Koronyo et al., 2017). However, the latter study involved two visits by volunteers for retinal fluorescence imaging with the oral administration of a curcumin supplement between appointments and blood testing to confirm curcumin uptake.

Separately, an infrared laser confocal quasi-elastic light scattering procedure (QLS) and the Fluorescent Ligand Eye Scanning (FLES) technique (Kerbage et al., 2015a) have been developed to detect amyloid-related pathology in the ocular lens. Aβ has been shown to accumulate in the retina and lens in patients with AD (Dentchev, Milam, Lee, Trojanowski, & Dunaief, 2003; Goldstein et al., 2003; Johnson et al., 2002; Kerbage et al., 2015b). These methods, however, are limited to subjects who have not been operated for cataracts as the presence of the natural eye lens is required. This technique also involves n the application of an extraneous fluorescent label.

Spectral changes were also reported in Alzheimer's mice relative to age-matched wild-type mice ex vivo (More & Vince, 2015) and in vivo (More, Beach, & Vince, 2016) using label-free reflectance hyperspectral retinal images. A similar phenomenom was observed in human brain and retina tissue ex vivo. These results support the idea that hyperspectral retinal imaging could be used to identify amyloid-related signs of central nervous system AD deposition without extraneous labeling. Due to the much higher inter-individual variability of fundus reflectance in humans however, direct translation to useful applications in humans of the described method, based exclusively on the spectral evaluation of the datasets, is unlikely when compared to a uniform mice cohort. This variability may overwhelm the effect of Aβ aggregates on the spectral signal. More advanced image analysis techniques than the direct spectral evaluation proposed by the authors will likely be required to isolate the spectral signature of amyloid in the human tissue.

Literature has also shown correlations between retinal vessels abnormalities and AD (Berisha et al., 2007; Feke, Hyman, Stern, & Pasquale, 2015; S. Frost et al., 2013; Javaid et al., 2016; Lim et al., 2016; Williams et al., 2015) suggesting a potential for retinal imaging to deliver new biomarkers of the disease. Among those, retinal vascular tortuosity (RVT) is caused by the natural capability of vessels to adapt to factors associated with certain diseases (Dougherty & Varro, 2000; Koh et al., 2010; Koprowski et al., 2012; Owen et al., 2009; Ţălu, 2013). RVT has been studied as an indicator of blood pressure and cardiovascular diseases (Cheung et al., 2011; Gopinath et al., 2014; Tsui et al., 2009), diabetes , neuroretinal rim thinning (Koh et al., 2010), diabetic retinopathy, hypertensive retinopathy, retinopathy of prematurity, facio Scapulo Humeral Muscular Dystrophy (FSHD), and Coats diseases (Kanski & J.Kanski, 2007; Longmuir, Longmuir, Matthews, Olson, & Abramoff, 2009). Recent studies have further shown a relationship between RVT and AD (Ascaso et al., 2014; Attems & Jellinger, 2014; S. Frost et al., 2013; Williams et al., 2015).

A simple, non-invasive, and accessible technique to establish the presence or absence of cerebral amyloid plaques by looking at the retina has recently been developed by Optina Diagnostics. It uses the Metabolic Hyperspectral Retinal Camera (MHRC), a system that permits the acquisition of a series of retinal images obtained at specific wavelengths covering the visible and near infrared spectrum in combination with a proprietary classifier using spatial and spectral texture features obtained with the MHRC to determine the likely amyloid status of the brain. This approach does not aim to visualize directly amyloid deposits in the retina but rather to determine a likely amyloid status based on sets of image features highly correlated with the cerebral amyloid status.

The purpose of this study was to derive retinal vascular metrics from the hyperspectral retinal images and to evaluate their capability to discriminate subjects based on their cerebral PET amyloid status, on their own and in combination with texture metrics extracted from the hyperspectral retinal images. To that end, RVT and retinal vessels diameter were evaluated from images of a hyperspectral fundus camera. They were combined with spatial/spectral texture measures, taken over and around vessels to identify discriminating features. Following dimensional reduction, the predictive power of the measures was evaluated using a SVM classifier trained to discriminate between Aβ-positives and Aβ-negative subjects as define by PET scanning.

4.3 Methods

4.3.1 Subjects

All procedures were approved by the ethics committees of Polytechnique Montreal, McGill University, Hopital Maisoneuve-Rosemont and Véritas IRB. Subjects were aged between 60 and 85 years and had no retinal diseases or significant ocular media opacity, as determined by an ophthalmological evaluation. The studied cohort (n=46) included 20 cognitively impaired subjects (values outside the normal range for the Mini-Mental State Examination (MMSE) and/or the Montreal Cognitive Assessment (MoCA)) and 26 control cases with unimpaired cognition. Following PET amyloid imaging, 7 out of 20 cognitively impaired cases were identified as amyloid negative, while 3 of the 26 cognitively unimpaired subjects were amyloid positive.

4.3.2 Hyper-spectral retinal imaging

Pupils were dilated (> 6mm) using 1% w/v tropicamide and 2.5% w/v phenylephrine prior to the ophthalmological evaluation and retinal imaging. Retinal images were acquired using a Metabolic Hyperspectral Retinal Camera (MHRC) developed by Optina Diagnostics (Desjardins et al., 2016; "Optina Diagnostics," n.d.). The MHRC is based on a custom-built mydriatic fundus camera incorporating a Tunable Light Source, able to transmit safe light levels within a spectral range covering the visible to the near infrared region of the spectrum within a series of narrow bandwidths (<3nm). A schematic of the MHRC is shown in Figure 4.1. Images of the retina on a field of view of ≈ 30° were sequentially obtained for different monochromatic illumination wavelengths to build a cube of 91 images obtained in the spectral range of 450 to 900 nm in steps of 5nm in approximately 1 second. The images were normalized as previously described to correct for the response of the instrument and spatially registered to correct wavelength-dependent optical deformations (scaling) and eye movements (translation and rotation) that may occur during the acquisition.

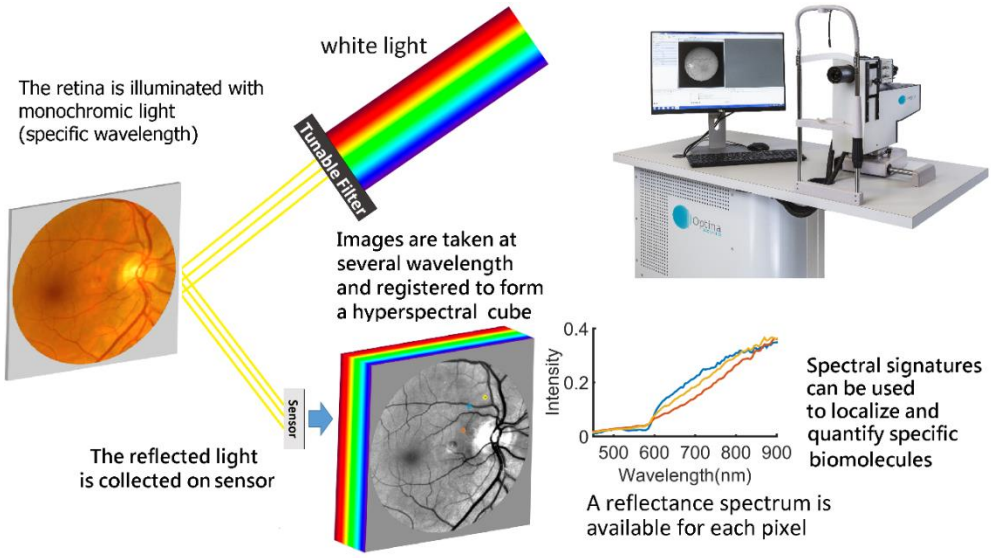

Figure 4.1 Schematic of the Metabolic Hyper-Spectral Retinal Camera used for acquiring the images.

4.3.3 PET scans and SUVR measurements

Amyloid imaging was performed using 18F-Florbetaben at a dose of 300 MBq (approx. 8.0 mCi) ± 20% on a General Electric PET/CT Discovery ST16. A very low-dose CT pilot study was performed to permit optimal positioning of the acquisition field centered on the brain. A low-dose computed tomography acquisition was performed initially to permit attenuation correction (40 mAs, 140 kvP. Pitch 3). PET acquisition was performed in 3D mode over a period of 20 minutes. OSEM iterative reconstruction (2 subsets, 10 iterations) was performed subsequently, with correction for attenuation by low-dose computed tomography. The reconstruction also includes the standard corrections for scattered photons and random detection. The cerebral amyloid status was determined from binary reads by a panel of 3 expert readers with experience in reporting such studies. Each reader evaluated independently the amyloid PET scans for all the participants of the study and an in-person meeting was organized with all three readers to review cases where readings were discordant in order to rule on a final amyloid status for each participant.

4.3.4 Retinal data processing

Normalization and Registration

Due to spatial and spectral variations that may arise in light source intensity and system optics, raw data cubes were normalized using white, dark and baseline images that were recorded prior to human acquisitions. More details about the image normalization are described in (Patel, Flanagan, Shahidi, Sylvestre, & Hudson, 2013). After normalization, each image of the cube was spatially registered with the previous one to correct wavelength-dependent optical deformations (scaling) and eye movements (translation and rotation) which may occur during the HSI acquisition. The reflectance spectrum generated at each pixel was then available to be analyzed to identify spectral signatures associated with chromophores of interests (Desjardins et al., 2016).

Vessel Segmentation

All vessels with a diameter larger than 3 pixels (approximately 25 μm) were automatically segmented and classified as arteriole or venule. Results were corrected for any misclassification using a graphical user interface built for this task.

Tortuosity measurement

Vessels segments between bifurcations were extracted and thinned to their skeleton, then tortuosity of each vessel segment was computed by taking the integral of the square derivative of curvature divided by the length of a curve (Patasius, Marozas, Jegelevicius, & Lukosevicius, 2005). For each of the images, average RVT values of arterioles and venules were calculated separately for all segmented vessels described above, except for vasculature located inside the optical nerve head (ONH) which were masked and excluded from the RVT measurements. Aβ+ and Aβ- subjects were compared based on average RVT values of their arterioles and venules. Figure 4.2-a illustrates sample outputs of the software developed for vessels' tortuosity measurement with a curvature map of a vessel segment.

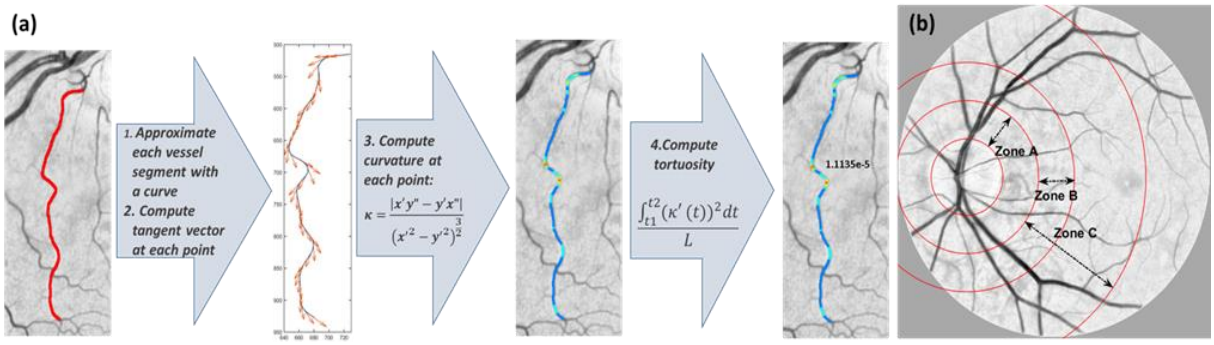

Figure 4.2 (a) Tortuosity measurement steps of a sample vessel segment. (b) Different zones of retina: zone A (region from 0 to0.5 ONH diameters away from the ONH margin), zone B (region from 0.5 to 1 ONH diameters away from the ONH margin), and zone C (region from 0.5 to2 ONH diameters away from the ONH margin).

Diameter measurements

For each vessel segment located between two bifurcations, one third of the centerline pixels were randomly chosen. The diameter of the vessel segment was calculated as the average of the length of the shortest paths passing through the selected centerline pixels. Vessel diameters were calculated for three different retinal zones: zone A (region from 0 to0.5 ONH diameters away from the ONH margin), zone B (region from 0.5 to 1 ONH diameters away from the ONH margin), and zone C (region from0.5 to2 ONH diameters away from the ONH margin) by taking the average of the vessels' diameter within the associated zone. Figure 4.2(b) illustrates the different retinal zones per this definition.

Image analysis

Image features were built using standard texture measures that included contrast, correlation, energy, homogeneity, standard deviation, range and entropy (Haralick, Shanmugam, & Dinstein, 1973). The textures were calculated along the spectral dimension of the HSI cube and along a combination of spectral and spatial dimensions. In addition to the full range of the available spectrum (i.e. 450-900 nm), different bands in between were separately investigated for texture measurements following observations of maximal spectral changes. The measures were calculated for different anatomical areas of the retina including arterioles, venules, regions around arterioles and venules (separately).

Feature selection and Classification

An initial set of features included vessels' tortuosity, diameter, AVR, and texture measures extracted from arterioles and venule and adjacent regions (including about 70 μm away from the vessel's border). After a sequential feature selection, 8 features with highest validation criterion were selected. The validation criterion was evaluated through a 10-fold cross-validation of the initial set of features by repeatedly fitting a multivariate normal density function to each group of data (i.e. Aβ+ and Aβ-), with different training and testing subsets. Table 4.1 summarizes the selected features and their attributes. Although texture measures are dependent features, we Bonferroni corrected p-values to illustrate the minimum p-value that could be considered for each of the features. Following Principal Component Analysis (PCA) of the features in Table 4.1, a SVM classifier with linear kernel was trained to discern Aβ+ subjects from Aβ- subjects.

Table 4.1 Eight features yielded by sequential feature selection. Anatomical regions, bands, and directions in which features were extracted are shown.

Feature code	Feature name	Anatomical region	Band(nm)	Direction	p-value
F1	tortuosity	venules	-	-	1.6e-6
F2	diameter	arterioles – zone A	-	-	0.0104
F3	Contrast (texture)	arterioles and around	450-550	spectral	1.05e-6
F4	Energy (texture)	arterioles and around	450-550	spectral	9.6e-7
F5	Energy (texture)	arterioles	700-900	spectral	0.0056
F6	Contrast (texture)	arterioles and around	450-550	spatial/spectral	7.4e-5
F7	Correlation (texture)	arterioles and around	450-550	spatial/spectral	0.0160
F8	Homogeneity (texture)	arterioles and around	450-550	spatial/spectral	2.9e-5

4.4 Results

Retinal venules of the PET amyloid positive subjects showed a higher mean tortuosity compared to the amyloid negative subjects ($p<1.6e-6$). Also, significant difference was observed between arterioles' tortuosity of Aβ+ and Aβ- subjects ($p<0.002$). Moreover, mean arterioles' diameters in Zone A ($p<0.011$) and Zone C ($p<0.02$) showed a significant difference between the two groups of subjects. Different textures measures of arterioles and adjacent regions also showed significant differences in Aβ+ retinal images compared to Aβ-. To provide the full distribution, Figure 4.3

illustrates the data points, mean, SEM (light gray) and standard deviations (dark gray) and associated p-values of each feature identified through the selection process.

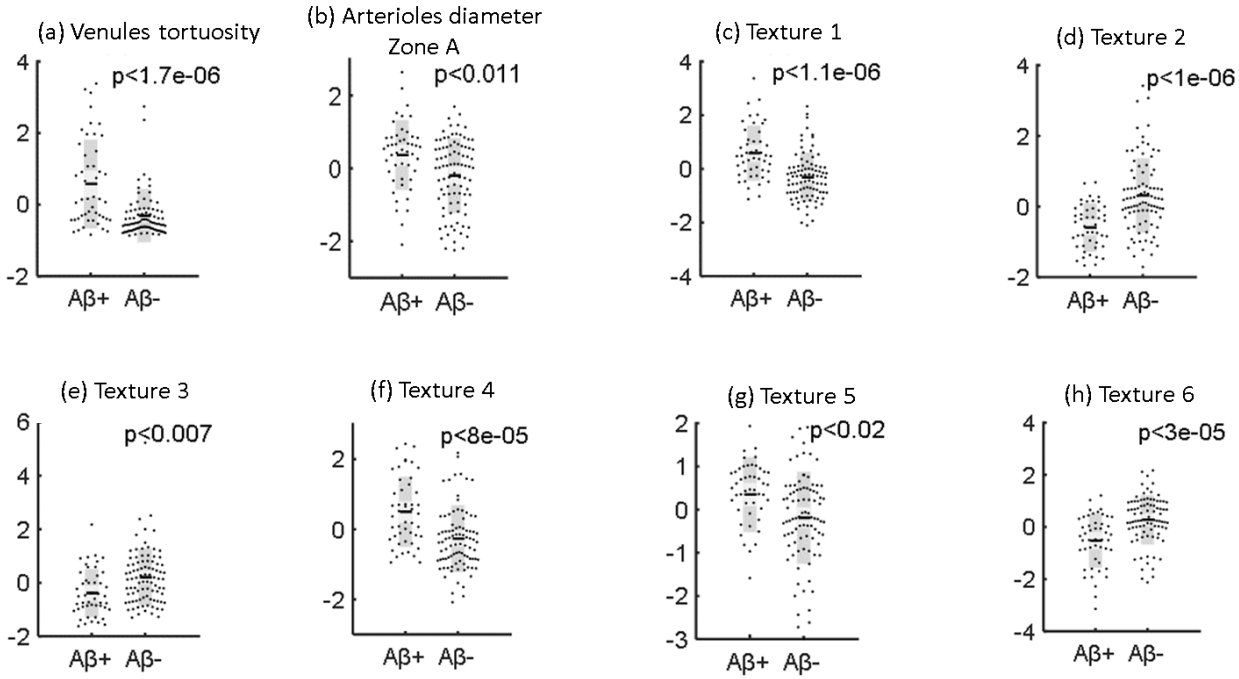

Figure 4.3 Difference between amyloid positive and amyloid negative subjects corresponding to features F1 (a) to F8 (h)−Data points are shown as normalized values.

For automatic discrimination of Aβ+ from Aβ- subjects, features F1 to F8 were used to train a SVM classifier with linear kernel. Ten-fold cross validation was conducted to evaluate classification loss of the classifier (from observations not used for training). Figure 4.4 (a) shows how classification loss of this classifier changes by stepwise appending the principal components of the features F1 to F8. The distribution of classification loss values was evaluated by repetitive execution of 10-fold cross validation in each step. The smallest cross validation loss is associated with 7th principal component (0.14±0.005).

Finally, to investigate the benefit of combining different types of features i.e. vasculature features and texture measures in improving the accuracy of discrimination between Aβ+ and Aβ- subjects, we evaluated the accuracy of the classification using texture measures (F3 to F8) and vasculature features (F1 and F2) separately. Figure 4.4 (b) compares classification loss when using vasculature (F1 and F2), textures (F3 to F8) and combined features (7 PCs of F1 to F8). One can observe that

lowest classification loss (0.14±0.005) is obtained when using a combined approach confirming the added information content of hyperspectral imaging.

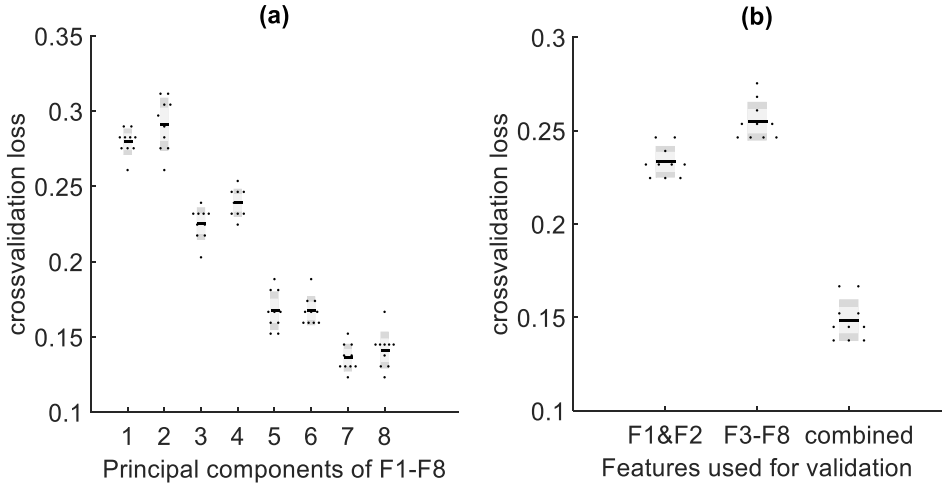

Figure 4.4 (a) SVM classification loss using principal components 1 to 8 inclusively; (b) comparison of classification losses when using different types of features.

Finally, Table 4.2 shows a comparison between classifications' accuracy when using different types of features. Sensitivity, specificity, positive predictive value (PPV) and negative predictive value (NPV) were obtained using 10-fold cross validations.

Table 4.2 Comparing classification performance based on features used. Performance was evaluated using cerebral amyloid status determined by PET imaging as gold standard.

Features used	Sensitivity	Specificity	PPV	NPV	Accuracy
Vasculature features (F1 and F2)	0.74±0.019	0.77±0.006	0.49±0.018	0.91±0.007	0.76±0.008
Texture measures (F3 to F8)	0. 68±0.022	0.76±0.007	0.50±0.019	0.87±0.012	0.74±0.010
Combined (7 PCs of F1 to F8)	0.82±0.022	0.86±0.011	0.73±0.025	0.91±0.011	0.85±0.013

4.5 Discussion

In this work, we aimed to establish a correlation between retinal image features related to the vasculature with cerebral Aβ deposition in the brain. The study was conducted using images taken by a novel hyperspectral imaging platform in a group of cognitively impaired and cognitively unimpaired subjects with known cerebral amyloid status determined by amyloid PET.

One of the findings was that both retinal arterioles and venules tortuosity were significantly higher in Aβ+ subjects than in Aβ- subjects ($p<0.002$, $p<1.6e-6$). This supports recent findings on the correlation between RVT and cognitive impairment (Ascaso et al., 2014; Brown & Thore, 2011; Williams et al., 2015) as well as RVT and amyloid deposition in the brain (S. Frost et al., 2013). In (Cheung et al., 2014) both arteriolar and venular tortuosity are reported to be increased in AD while in (Cheung et al., 2011), both arteriolar and venular tortuosity are reported to be inversely proportional to aging (between 60-80 yrs.). Considering the latter finding along with the studies supporting the increase of retinal vessels' tortuosity in AD patients, shows the importance of retinal vessels' tortuosity as a potential biomarker of AD among elderly subjects. Here, we quantitatively observed that not only the vessels' tortuosity, but also arteriole diameters in zone A ($p<0.02$) and texture measures taken over retinal arterioles and adjacent areas ($p<1e-6$) of Aβ+ subjects are significantly different from retinal images of Aβ- subjects. Significant differences in texture measures were observed in the spectral range 450 to 550 nm that is known as the spectral region most likely to be affected by scattering from amyloid aggregates in the retina. Also we observed significant difference in texture measures in the spectral range 700 to 900nm ($p<0.0008$) which is the spectral region least likely to be affected by the transmission of the anterior segment of the eye.

Despite significant difference between the groups, the important overlap between Aβ+ and Aβ- subjects (Figure 4.3) means that individual image features cannot achieve good separation of the two groups. We therefore used a combination of vasculature features and texture measures to classify Aβ+ and Aβ- subjects using a SVM classifier. Results showed that a classifier trained with vasculature measures alone, could discriminate Aβ+ from Aβ- subjects with an accuracy of 76%; however, combining vascular metrics with a set of spatial/spectral texture metrics resulted in a more accurate prediction of cerebral amyloid status with a classification loss of 0.14 ± 0.005 and accuracy of 85%. It should be noted that based on the method, type of textures, and the parameters used, the classification performance of texture features alone could be further optimized. For example, the proprietary method developed by Optina Diagnostics (J.-P. Soucy et al., 2018) achieved higher accuracy than the texture-based classification results shown in second row of Table 4.2.

Overall this study suggests that the inclusion of metrics related to the retinal vasculature in a classifier built from features extracted from hyperspectral retinal images could improve the discrimination performance of the cerebral amyloid status.

4.6 References

Abdalla, M., Hunter, A., & Al-Diri, B. (2015). Quantifying retinal blood vessels' tortuosity — Review. 2015 Science and Information Conference (SAI), 687–693. https://doi.org/10.1109/SAI.2015.7237216

Ascaso, F. J., Cruz, N., Modrego, P. J., Lopez-Anton, R., Santabárbara, J., Pascual, L. F., … Cristóbal, J. A. (2014). Retinal alterations in mild cognitive impairment and Alzheimer's disease: An optical coherence tomography study. Journal of Neurology, 261(8), 1522–1530. https://doi.org/10.1007/s00415-014-7374-z

Attems, J., & Jellinger, K. A. (2014). The overlap between vascular disease and Alzheimer's diseaseâ□"Lessons from pathology. BMC Medicine, 12, 206. https://doi.org/10.1186/s12916-014-0206-2

Berisha, F., Feke, G. T., Trempe, C. L., McMeel, J. W., & Schepens, C. L. (2007). Retinal Abnormalities in Early Alzheimer's Disease. Investigative Opthalmology & Visual Science, 48(5), 2285. https://doi.org/10.1167/iovs.06-1029

Brown, W. R., & Thore, C. R. (2011). Review: Cerebral microvascular pathology in ageing and neurodegeneration. Neuropathology and Applied Neurobiology, 37(1), 56–74. https://doi.org/10.1111/j.1365-2990.2010.01139.x

Ceccaldi, M., Jonveaux, T., Verger, A., Krolak-Salmon, P., Houzard, C., Godefroy, O., … Guedj, E. (2018). Added value of 18F-florbetaben amyloid PET in the diagnostic workup of most complex patients with dementia in France: A naturalistic study. Alzheimer's & Dementia: The Journal of the Alzheimer's Association, 14(3), 293–305. https://doi.org/10.1016/j.jalz.2017.09.009

Cheung, C. Y., Ong, Y. T., Ikram, M. K., Ong, S. Y., Li, X., Hilal, S., … Wong, T. Y. (2014). Microvascular network alterations in the retina of patients with Alzheimer's disease. Alzheimer's & Dementia, 10(2), 135–142. https://doi.org/10.1016/j.jalz.2013.06.009

Cheung, C. Y., Zheng, Y., Hsu, W., Lee, M. L., Lau, Q. P., Mitchell, P., … Wong, T. Y. (2011). Retinal Vascular Tortuosity, Blood Pressure, and Cardiovascular Risk Factors. Ophthalmology, 118(5), 812–818. https://doi.org/10.1016/j.ophtha.2010.08.045

Dentchev, T., Milam, A. H., Lee, V. M.-Y., Trojanowski, J. Q., & Dunaief, J. L. (2003). Amyloid-beta is found in drusen from some age-related macular degeneration retinas, but not in drusen from normal retinas. Molecular Vision, 9, 184–190.

Desjardins, M., Sylvestre, J.-P., Jafari, R., Kulasekara, S., Rose, K., Trussart, R., … Lesage, F. (2016). Preliminary investigation of multispectral retinal tissue oximetry mapping using a hyperspectral retinal camera. Experimental Eye Research, 146, 330–340. https://doi.org/10.1016/j.exer.2016.04.001

Dougherty, G., & Varro, J. (2000). A quantitative index for the measurement of the tortuosity of blood vessels. Medical Engineering & Physics, 22(8), 567–574.

Edwards, M. M., Rodríguez, J. J., Gutierrez-Lanza, R., Yates, J., Verkhratsky, A., & Lutty, G. A. (2014). Retinal macroglia changes in a triple transgenic mouse model of Alzheimer's disease. Experimental Eye Research, 127, 252–260. https://doi.org/10.1016/j.exer.2014.08.006

Feke, G. T., Hyman, B. T., Stern, R. A., & Pasquale, L. R. (2015). Retinal blood flow in mild cognitive impairment and Alzheimer's disease. Alzheimer's & Dementia: Diagnosis, Assessment & Disease Monitoring, 1(2), 144–151. https://doi.org/10.1016/j.dadm.2015.01.004

Frost, S., Kanagasingam, Y., Sohrabi, H., Vignarajan, J., Bourgeat, P., Salvado, O., … the AIBL Research Group. (2013). Retinal vascular biomarkers for early detection and monitoring of Alzheimer's disease. Translational Psychiatry, 3(2), e233. https://doi.org/10.1038/tp.2012.150

Frost, Shaun, Kanagasingam, Y., Macaulay, L., Koronyo-Hamaoui, M., Koronyo, Y., Biggs, D., … Martins, R. (2014). RETINAL AMYLOID FLUORESCENCE IMAGING PREDICTS CEREBRAL AMYLOID BURDEN AND ALZHEIMER'S DISEASE. Alzheimer's & Dementia: The Journal of the Alzheimer's Association, 10(4), P234–P235. https://doi.org/10.1016/j.jalz.2014.04.341

Garcia-Alloza, M., Borrelli, L. A., Rozkalne, A., Hyman, B. T., & Bacskai, B. J. (2007). Curcumin labels amyloid pathology in vivo, disrupts existing plaques, and partially restores distorted neurites in an Alzheimer mouse model. Journal of Neurochemistry, 102(4), 1095–1104. https://doi.org/10.1111/j.1471-4159.2007.04613.x

Goldstein, L. E., Muffat, J. A., Cherny, R. A., Moir, R. D., Ericsson, M. H., Huang, X., … Bush, A. I. (2003). Cytosolic beta-amyloid deposition and supranuclear cataracts in lenses from people with Alzheimer's disease. Lancet (London, England), 361(9365), 1258–1265. https://doi.org/10.1016/S0140-6736(03)12981-9

Gopinath, B., Chiha, J., Plant, A. J. H., Thiagalingam, A., Burlutsky, G., Kovoor, P., … Mitchell, P. (2014). Associations between retinal microvascular structure and the severity and extent of coronary artery disease. Atherosclerosis, 236(1), 25–30. https://doi.org/10.1016/j.atherosclerosis.2014.06.018

Grundman, M., Johnson, K. A., Lu, M., Siderowf, A., Dell'Agnello, G., Arora, A. K., … 18F-AV-45-A17 Study Group. (2016). Effect of Amyloid Imaging on the Diagnosis and Management of Patients with Cognitive Decline: Impact of Appropriate Use Criteria. Dementia and Geriatric Cognitive Disorders, 41(1–2), 80–92. https://doi.org/10.1159/000441139

Haralick, R. M., Shanmugam, K., & Dinstein, I. (1973). Textural Features for Image Classification. IEEE Transactions on Systems, Man, and Cybernetics, SMC-3(6), 610–621. https://doi.org/10.1109/TSMC.1973.4309314

Jack, C. R., Bennett, D. A., Blennow, K., Carrillo, M. C., Dunn, B., Haeberlein, S. B., … Contributors. (2018). NIA-AA Research Framework: Toward a biological definition of Alzheimer's disease. Alzheimer's & Dementia: The Journal of the Alzheimer's Association, 14(4), 535–562. https://doi.org/10.1016/j.jalz.2018.02.018

Javaid, F. Z., Brenton, J., Guo, L., & Cordeiro, M. F. (2016). Visual and Ocular Manifestations of Alzheimer's Disease and Their Use as Biomarkers for Diagnosis and Progression. Frontiers in Neurology, 7. https://doi.org/10.3389/fneur.2016.00055

Jiménez-Jiménez, F. J., Alonso-Navarro, H., García-Martín, E., & Agúndez, J. A. G. (2014). Cerebrospinal fluid biochemical studies in patients with Parkinson's disease: Toward a potential search for biomarkers for this disease. Frontiers in Cellular Neuroscience, 8. https://doi.org/10.3389/fncel.2014.00369

Jindahra, P., Hedges, T. R., Mendoza-Santiesteban, C. E., & Plant, G. T. (2010). Optical coherence tomography of the retina: Applications in neurology. Current Opinion in Neurology, 23(1), 16–23. https://doi.org/10.1097/WCO.0b013e328334e99b

Johnson, L. V., Leitner, W. P., Rivest, A. J., Staples, M. K., Radeke, M. J., & Anderson, D. H. (2002). The Alzheimer's A beta -peptide is deposited at sites of complement activation in pathologic deposits associated with aging and age-related macular degeneration. Proceedings of the National Academy of Sciences of the United States of America, 99(18), 11830–11835. https://doi.org/10.1073/pnas.192203399

J.-P. SOUCY, J.-P., C. CHEVREFILS, J.-P. SYLVESTRE, S. BEAULIEU, T. A. PASCOAL, S. M. SHARAFI, … F. LESAGE. (2018). Validation of a hyperspectral retinal imaging method to predict cerebral amyloid PET status. 2018 Neuroscience Meeting Planner. Presented at the 2018 Neuroscience Meeting Planner, San Diego, CA.

Kanski, J. J., & J.Kanski, by J. (2007). Clinical ophthalmology: A systematic approach (6th ed). Retrieved from https://trove.nla.gov.au/version/45741802

Kerbage, C., Sadowsky, C. H., Tariot, P. N., Agronin, M., Alva, G., Turner, F. D., … Hartung, P. D. (2015a). Detection of Amyloid β Signature in the Lens and Its Correlation in the Brain to Aid in the Diagnosis of Alzheimer's Disease. American Journal of Alzheimer's Disease and Other Dementias, 30(8), 738–745. https://doi.org/10.1177/1533317513520214

Kerbage, C., Sadowsky, C. H., Tariot, P. N., Agronin, M., Alva, G., Turner, F. D., … Hartung, P. D. (2015b). Detection of Amyloid β Signature in the Lens and Its Correlation in the Brain

to Aid in the Diagnosis of Alzheimer's Disease. American Journal of Alzheimer's Disease and Other Dementias, 30(8), 738–745. https://doi.org/10.1177/1533317513520214

Kesler, A., Vakhapova, V., Korczyn, A. D., Naftaliev, E., & Neudorfer, M. (2011). Retinal thickness in patients with mild cognitive impairment and Alzheimer's disease. Clinical Neurology and Neurosurgery, 113(7), 523–526. https://doi.org/10.1016/j.clineuro.2011.02.014

Koh, V., Cheung, C. Y., Zheng, Y., Wong, T. Y., Wong, W., & Aung, T. (2010). Relationship of Retinal Vascular Tortuosity with the Neuroretinal Rim: The Singapore Malay Eye Study. Investigative Ophthalmology & Visual Science, 51(7), 3736–3741. https://doi.org/10.1167/iovs.09-5008

Koprowski, R., Teper, S. J., Węglarz, B., Wylęgała, E., Krejca, M., & Wróbel, Z. (2012). Fully automatic algorithm for the analysis of vessels in the angiographic image of the eye fundus. Biomedical Engineering Online, 11, 35. https://doi.org/10.1186/1475-925X-11-35

Koronyo, Y., Biggs, D., Barron, E., Boyer, D. S., Pearlman, J. A., Au, W. J., … Koronyo-Hamaoui, M. (2017). Retinal amyloid pathology and proof-of-concept imaging trial in Alzheimer's disease. JCI Insight, 2(16), e93621. https://doi.org/10.1172/jci.insight.93621

Koronyo-Hamaoui, M., Koronyo, Y., Ljubimov, A. V., Miller, C. A., Ko, M. K., Black, K. L., … Farkas, D. L. (2011). Identification of amyloid plaques in retinas from Alzheimer's patients and noninvasive in vivo optical imaging of retinal plaques in a mouse model. NeuroImage, 54, S204–S217. https://doi.org/10.1016/j.neuroimage.2010.06.020

Kuhlmann, J., Andreasson, U., Pannee, J., Bjerke, M., Portelius, E., Leinenbach, A., … IFCC Working Group on Standardization of CSF proteins (WG-CSF). (2017). CSF Aβ1-42â□□An excellent but complicated Alzheimer's biomarkerâ□"A route to standardisation. Clinica Chimica Acta; International Journal of Clinical Chemistry, 467, 27–33. https://doi.org/10.1016/j.cca.2016.05.014

Lee, J.-Y., Kim, J. M., Ahn, J., Kim, H.-J., Jeon, B. S., & Kim, T. W. (2014). Retinal nerve fiber layer thickness and visual hallucinations in Parkinson's Disease. Movement Disorders:

Official Journal of the Movement Disorder Society, 29(1), 61–67. https://doi.org/10.1002/mds.25543

Lim, J. K. H., Li, Q.-X., He, Z., Vingrys, A. J., Wong, V. H. Y., Currier, N., … Nguyen, C. T. O. (2016). The Eye As a Biomarker for Alzheimer's Disease. Frontiers in Neuroscience, 10. https://doi.org/10.3389/fnins.2016.00536

Liu, B., Rasool, S., Yang, Z., Glabe, C. G., Schreiber, S. S., Ge, J., & Tan, Z. (2009). Amyloid-Peptide Vaccinations Reduce β-Amyloid Plaques but Exacerbate Vascular Deposition and Inflammation in the Retina of Alzheimer's Transgenic Mice. The American Journal of Pathology, 175(5), 2099–2110. https://doi.org/10.2353/ajpath.2009.090159

Longmuir, S. Q., Longmuir, R., Matthews, K., Olson, R., & Abramoff, M. (2009). Retinal Arterial but not Venous Tortuosity correlates with Facioscapulohumeral Muscular Dystrophy (FSHD) Severity. Investigative Ophthalmology & Visual Science, 50(13), 5419–5419.

Masters, C. L., Bateman, R., Blennow, K., Rowe, C. C., Sperling, R. A., & Cummings, J. L. (2015). Alzheimer's disease. Nature Reviews. Disease Primers, 1, 15056. https://doi.org/10.1038/nrdp.2015.56

More, S. S., Beach, J. M., & Vince, R. (2016). Early Detection of Amyloidopathy in Alzheimer's Mice by Hyperspectral Endoscopy. Investigative Ophthalmology & Visual Science, 57(7), 3231–3238. https://doi.org/10.1167/iovs.15-17406

More, S. S., & Vince, R. (2015). Hyperspectral imaging signatures detect amyloidopathy in Alzheimer's mouse retina well before onset of cognitive decline. ACS Chemical Neuroscience, 6(2), 306–315. https://doi.org/10.1021/cn500242z

Ning, A., Cui, J., To, E., Ashe, K. H., & Matsubara, J. (2008). Amyloid-beta deposits lead to retinal degeneration in a mouse model of Alzheimer disease. Investigative Ophthalmology & Visual Science, 49(11), 5136–5143. https://doi.org/10.1167/iovs.08-1849

Olsson, B., Lautner, R., Andreasson, U., Öhrfelt, A., Portelius, E., Bjerke, M., … Zetterberg, H. (2016). CSF and blood biomarkers for the diagnosis of Alzheimer's disease: A systematic review and meta-analysis. The Lancet. Neurology, 15(7), 673–684. https://doi.org/10.1016/S1474-4422(16)00070-3

Optina Diagnostics. (n.d.). Retrieved April 3, 2019, from http://optinadx.com/

Owen, C. G., Rudnicka, A. R., Mullen, R., Barman, S. A., Monekosso, D., Whincup, P. H., … Paterson, C. (2009). Measuring retinal vessel tortuosity in 10-year-old children: Validation of the Computer-Assisted Image Analysis of the Retina (CAIAR) program. Investigative Ophthalmology & Visual Science, 50(5), 2004–2010. https://doi.org/10.1167/iovs.08-3018

Paquet, C., Boissonnot, M., Roger, F., Dighiero, P., Gil, R., & Hugon, J. (2007). Abnormal retinal thickness in patients with mild cognitive impairment and Alzheimer's disease. Neuroscience Letters, 420(2), 97–99. https://doi.org/10.1016/j.neulet.2007.02.090

Parisi, V., Restuccia, R., Fattapposta, F., Mina, C., Bucci, M. G., & Pierelli, F. (2001). Morphological and functional retinal impairment in Alzheimer's disease patients. Clinical Neurophysiology, 112(10), 1860–1867. https://doi.org/10.1016/S1388-2457(01)00620-4

Patasius, M., Marozas, V., Jegelevicius, D., & Lukosevicius, A. (2005). Evaluation of tortuosity of eye blood vessels using the integral of square of derivative of curvature. IFMBE Proc. 3rd Eur. Med. Biol. Eng. Conf.(EMBEC05), 11.

Perez, S. E., Lumayag, S., Kovacs, B., Mufson, E. J., & Xu, S. (2009). Beta-amyloid deposition and functional impairment in the retina of the APPswe/PS1DeltaE9 transgenic mouse model of Alzheimer's disease. Investigative Ophthalmology & Visual Science, 50(2), 793–800. https://doi.org/10.1167/iovs.08-2384

Rabinovici, G. D., Gatsonis, C., Apgar, C., Gareen, I. F., Hanna, L., Hendrix, J., … Carrillo, M. C. (2017). IMPACT OF AMYLOID PET ON PATIENT MANAGEMENT: EARLY RESULTS FROM THE IDEAS STUDY. Alzheimer's & Dementia: The Journal of the Alzheimer's Association, 13(7), P1474. https://doi.org/10.1016/j.jalz.2017.08.003

Shah, T. M., Gupta, S. M., Chatterjee, P., Campbell, M., & Martins, R. N. (2017). Beta-amyloid sequelae in the eye: A critical review on its diagnostic significance and clinical relevance in Alzheimer's disease. Molecular Psychiatry, 22(3), 353–363. https://doi.org/10.1038/mp.2016.251

Ţălu, Ş. (2013). Characterization of retinal vessel networks in human retinal imagery using quantitative descriptors. 5(2), 6.

Tsui, I., Shamsa, K., Perloff, J. K., Lee, E., Wirthlin, R. S., & Schwartz, S. D. (2009). Retinal vascular patterns in adults with cyanotic congenital heart disease. Seminars in Ophthalmology, 24(6), 262–265. https://doi.org/10.3109/08820530903400739

Williams, M. A., McGowan, A. J., Cardwell, C. R., Cheung, C. Y., Craig, D., Passmore, P., … McKay, G. J. (2015). Retinal microvascular network attenuation in Alzheimer's disease. Alzheimer's & Dementia: Diagnosis, Assessment & Disease Monitoring, 1(2), 229–235. https://doi.org/10.1016/j.dadm.2015.04.001

Yang, F., Lim, G. P., Begum, A. N., Ubeda, O. J., Simmons, M. R., Ambegaokar, S. S., Cole, G. M. (2005). Curcumin inhibits formation of amyloid beta oligomers and fibrils, binds plaques, and reduces amyloid in vivo. The Journal of Biological Chemistry, 280(7), 5892–5901. https://doi.org/10.1074/jbc.M404751200

CHAPTER 5 ARTICLE 2: HYPERSPECTRAL RETINAL BIOMARKERS OF ATHEROSCLEROSIS

Sayed Mehran Sharafi[a], Jean-Philippe Sylvestre[b], Claudia Chevrefils[b], Marc-André Rhéaume[e], Jean Daniel Arbour[e], Jean-Claude Tardif[d], Frédéric Lesage *[a,d]

[a] Genie Electrique, Polytechnique Montreal, Montreal, Quebec, Canada, H3C 3A7;

[b] Optina Diagnostics, Montreal, Quebec, Canada, H4T 1Z2;

[c] Montreal Neurological Institute, McGill University, Montreal, Quebec, Canada, H3A 2B4 ;

[d] Research Center, Montreal Heart Institute, Montreal, Quebec, Canada, H1T 1C8 ;

[e] Clinique ophtalmologique 2121, Montreal, Quebec, H3H 1G6

• This article was submitted to the journal of Biomedical Optics Express on July 2019

5.1 Abstract

This study aimed to investigate hyperspectral retinal image features associated with atherosclerosis (ATH). 60 retinal images from 30 clinically probable ATH and 30 age-matched control cases were acquired using a hyperspectral retinal imaging system. Image texture metrics in both spatial and spectral dimensions were calculated in addition to vessel diameter and tortuosity. Retinal arterioles of ATH subjects showed a significant narrowing when compared to control subjects. Furthermore, a significant difference between image texture measures taken over retinal arterioles and venules and their adjacent regions were observed between ATH and control subjects. Classifiers were then trained to automatically discriminate subjects using the combined extracted features. A linear discriminant classifier based on retinal imaging could discern ATH subjects from control subjects with an accuracy of 87%.

Keywords: Hyperspectral retinal imaging; Atherosclerosis, Image processing; Machine learning

5.2 Introduction

Atherosclerosis (ATH) is a disease in which cholesterol accumulate in the inner most layer of the artery wall (the ‘tunica intima’) forming plaques,(Couper et al., 2002) triggering an inflammatory response and ultimately narrowing the lumen of the artery and restricting blood flow (Libby,

Lichtman, & Hansson, 2013). In advanced stages, depending on which arteries are affected, it can result in peripheral artery disease, kidney problems, heart attack and stroke ("Atherosclerosis | National Heart, Lung, and Blood Institute (NHLBI)," n.d.). Atherosclerosis can remain asymptomatic for decades and does not produce symptoms until sufficient narrowing or closure of an artery due to clots occurs when the patient experiences other cardiovascular disorders such as a stroke or heart attack.

Apart from methods that aim to identify severe narrowing of arteries (e.g. angiography, stress testing, hypertension), current diagnostics mostly rely on measuring carotid intima-media thickness (IMT) and arterial stiffness (Lorenz, Markus, Bots, Rosvall, & Sitzer, 2007; Mitchell et al., 2010; Nambi et al., 2012a; Niu et al., 2013). The carotid IMT is measured from ultrasound B-mode images by detecting the lumen-intima and media-adventitia interfaces over an artery segment (Nambi et al., 2012b; Sundholm, Gustavsson, & Sarkola, 2014). Arterial stiffness is mostly estimated by measuring the diameter change during the cardiac cycle from B-mode echo-tracking images (Blacher, Guerin, Pannier, Marchais, & London, 2001). However, in addition to cost, these methods are highly operator-dependent and time-consuming (Niu et al., 2014). Moreover, there is a growing need for finding methods and biomarkers that will allow to further risk-stratify patients. This becomes even more important in subsets of the population, such as women, in whom traditional predictors of risk might be inadequate (McClintic, McClintic, Bisognano, & Block, 2010). Literature has shown that cardiovascular diseases, and more specifically atherosclerosis, also have manifestations in fundoscopic measures of retinal arterioles and venules (Heitmar, Lip, Ryder, & Blann, 2017; Ikram et al., 2004; McClintic et al., 2010; McGeechan et al., 2009; Seidelmann et al., 2016; Sharrett et al., 1999; Tedeschi-Reiner, Strozzi, Skoric, & Reiner, 2005). The low cost, wide availability, reproducibility and radiation free assessments of fundoscopic imaging suggests the intriguing possibility of its use to quantify biomarkers of atherosclerosis (Chiu et al., 2018) .

Almost all of the studies conducted in this research area so far, have used monochromic or RGB imaging that mostly allow for investigating spatial features of retinal images and thus finding "spatial hallmarks". By using 2D or 3D intensity images, hidden tissue-related characteristics may remain uncovered. On the other hand, acquiring images using different monochromic wavelengths provides us with the relative variances in intensities across differing wavelengths. In this technique

(known as hyper-spectral imaging—HSI), the spectral data at each pixel, enable HSI to identify a signature of pathological conditions while multispectral imaging (like RGB) may miss significant spectral information (More & Vince, 2015). Therefore, using retinal HSI, not only the common spatial features but also "spectral signatures" of more subtle changes in the retinal tissue may become identifiable. This helps finding a wider variety of spatial/spectral features for a more accurate investigation of retinal biomarkers of diseases.

The purpose of this study was to investigate image features associated with retinal vasculature and adjacent tissue in a cohort of ATH positive and age-matched control subjects with the goal of identifying biomarkers of ATH and their prediction ability. To that end, retinal vessels tortuosity, arterioles and venules diameters and the arterio-venular ratio (AVR) were evaluated from images of a hyperspectral fundus camera. With the assumption that image texture analysis could help identify subtle differences in the spatial/spectral dimensions between subjects with atherosclerosis and controls, vasculature measures were combined with spatial and spectral texture measures derived from the hyperspectral images. The textures of different anatomical regions in the retinal hyperspectral images, including inside and around vessels were investigated with the aim of identifying discriminating features between groups. Following dimensional reduction, a linear classifier was trained using the final set of features to discern positive from negative subjects.

5.3 Methods

5.3.1 Subjects

All procedures were approved by the ethics committee of the Research Ethics and New Technology Development Committee at the Montreal Heart Institute (MHI). The studied cohort (n=60) included 30 clinically probable ATH and 30 age-matched control cases. Subjects were aged at least 18 years and underwent an ophthalmic examination to assess inclusion/exclusion criteria consisting first of a slit-lamp evaluation, an optical coherence tomography assessment plus a color fundus image following the instillation of eye drops to dilate the pupils. Subjects then underwent baseline hyperspectral retinal imaging.

5.3.2 Subjects inclusion/exclusion criteria

Inclusion criteria for subjects suffering from atherosclerosis included: myocardial infarction; coronary angiography showing at least one coronary stenosis (more than 50%); and/or coronary angioplasty; and/or coronary bypass.

Healthy control subjects had no medical history of cardiovascular, cerebrovascular and peripheral arterial disease. Exclusion criteria for healthy control subjects were: myocardial infarction or angina, known coronary stenosis, coronary angioplasty history or coronary bypass surgery, stroke or transient ischemic attack history, peripheral artery disease history, active smoking or history smoking in the past 5 years, diabetes mellitus, familial hypercholesterolemia, and poorly controlled hypertension (systolic blood pressure ≥ 150 mm Hg).

Furthermore, subjects with the following criteria were also excluded irrespective of the above groups: medium or high opacity of the lens, bleeding in vitreous, presence of venous occlusion, age-related macular degeneration or glaucoma; pupillary dilation inadequate or contra-indicated; deficient visual fixation; refractive error outside of the range -9 to +9; and inability to obtain satisfactory images with the MHRC.

5.3.3 Hyperspectral retinal imaging

To acquire retinal images, we used a Metabolic Hyper-spectral Retinal Camera (MHRC) developed by Optina Diagnostics (Desjardins et al., 2016). The MHRC is a research instrument which images the retina non-invasively and Health Canada authorization was obtained for its use in the context of this study. The MHRC is based on a custom-built mydriatic fundus camera incorporating a Tunable Light Source able to transmit safe light levels within a spectral range covering the visible to the near infrared with a narrow bandwidth (<3nm). A schematic of the MHRC is shown in Figure 3.1.

Prior to the ophthalmological evaluation and retinal imaging, tropicamide 1% w/v and phenylephrine 2.5% w/v were instilled in the eyes to make the pupils dilated (>6mm). Retinal images within a field of view of 30° covering the optic nerve head and the macula were sequentially obtained for different monochromatic illumination wavelengths to build a cube of data within approximately 1 second. Each pixel on the image corresponded to approximately 8.3µm on the

fundus. After image registration to correct eye movements, a spectrum can be extracted at each pixel. Therefore, not only the anatomical structures but also the spectral signatures of underlying chromophores in the fundus could be revealed (Desjardins et al., 2016). In this work, we used MHRC reflectance images taken at wavelengths located between 450 and 900 nm with a 5nm step. Each Hyperspectral image (HSI) was comprised of 91 gray-scale images stored as a cube of data (H5 file).

5.3.4 Retinal image processing

1) Normalization and Registration

Raw data cubes were normalized to correct the spatial and spectral variations that may arise in light source intensity and system optics (Patel, Flanagan, Shahidi, Sylvestre, & Hudson, 2013). Moreover, due to wavelength-dependent optical deformations (scaling) and eye movements (translation and rotation) which may occur during the HSI acquisition, each image of the cube was spatially registered with the previous one. The reflectance spectrum generated at each pixel was then available to identify spectral signatures and possible hallmarks of atherosclerosis at different anatomical regions of the retina.

2) Vessels segmentation

All vessels with a diameter larger than 3 pixels (approximately 33 μm) were automatically segmented using by combining two thresholding segmentation phases separately for extracting fine and coarse vessels with different pre- and post-processing methods. Segmented vessels then classified as arterioles and venules using a linear classifier that was trained with the spectral data and known absorption properties of hemoglobin. Results were corrected manually for any classification errors using a GUI.

3) Tortuosity measurement

Vessels segments between bifurcations were extracted and skeletonized and then the tortuosity of each vessel segment was computed by taking the integral of the square derivative of curvature divided by the length of the curve (Patasius, Marozas, Jegelevicius, & Lukosevicius, 2005). For each of the images, average tortuosity of arterioles and venules were calculated separately for all segmented vessels described above, except for vasculature located inside the optical nerve head

(ONH). ATH and control subjects were compared based on average tortuosity values of their arterioles and venules separately. Figure 5.1 illustrates a typical output of the software developed for vessels' tortuosity with curvature map on a sample vessel segment.

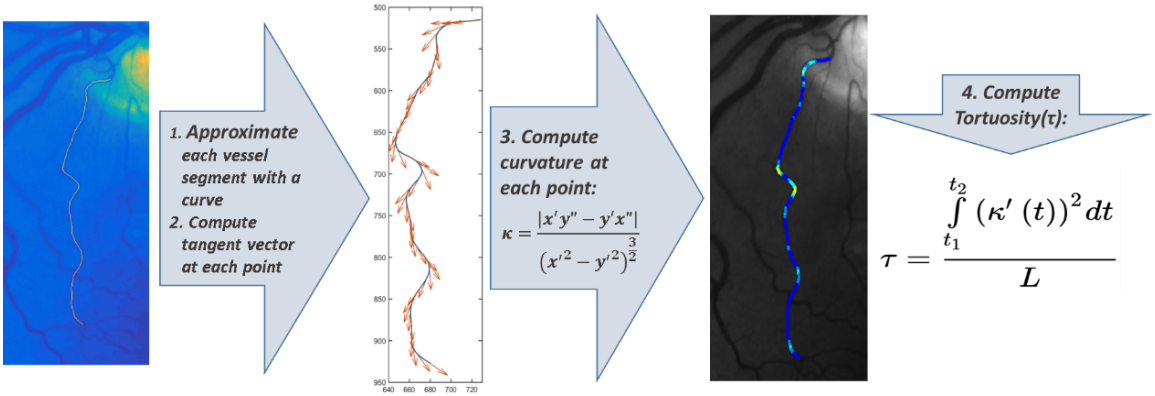

Figure 5.1 Schematic of tortuosity measurement for a vessel segment

4) Diameter measurements

For each vessels segment located between two bifurcations, one third of the total number of the centerline pixels of each vessel segment were randomly chosen. The diameter of the vessel segment was calculated as the average of the length of the shortest paths passing through the selected centerline pixels. Vessels' diameters were calculated in three different retinal zones defined as zone A (region from 0 to 0.5 ONH diameters away from the ONH margin), zone B (region from 0.5 to 1 ONH diameters away from the ONH margin), and zone C (region from 0.5 to2 ONH diameters away from the ONH margin) by taking the maximum vessels' diameter within the associated zone. Figure 5.2 illustrates an output of the algorithm developed for vessels' diameter measurement in different retinal zones with diameters marked on corresponding arterioles and venules.

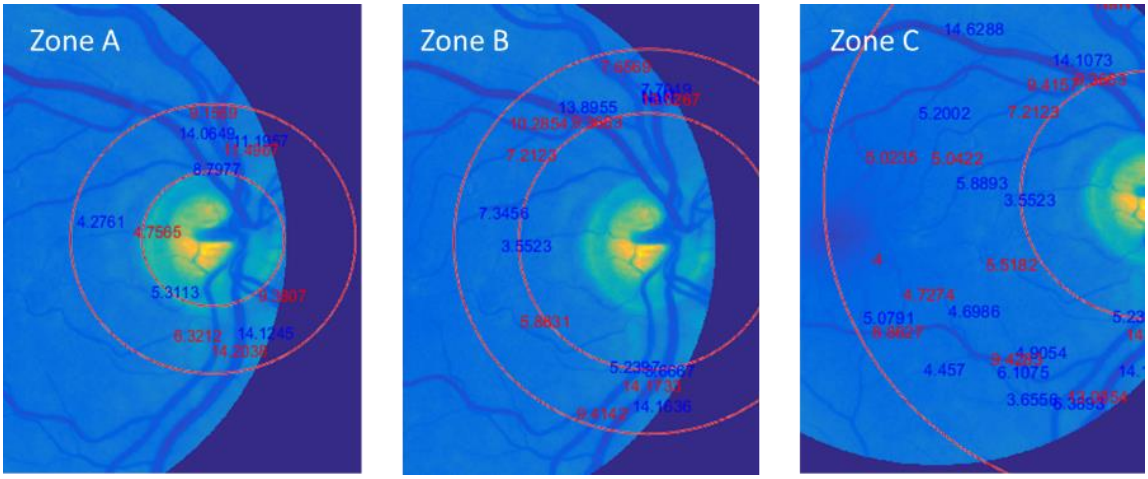

Figure 5.2 Different Anatomical zones of the retina used for automatic arterioles and venules diameter measurements.

5) Image analysis

Other image features were built using standard texture measures based on the gray level co-occurrence matrix (GLCM) and its statistics. The textures derived from the GLCM approach that were analyzed included contrast, correlation, energy, and homogeneity (Haralick, Shanmugam, & Dinstein, 1973) which correspond to descriptive statistics specifying variation in pixel intensities along specific directions in the hyperspectral cube. In our study, assuming each HSI as a cube of data, the textures were calculated along both spectral and spatial/spectral (i.e. diagonal) directions. In addition to the full range of the available spectrum (i.e. 450-900 nm), spectral bands at 450-550 nm (the band associated with optimized contrast between vessels and the background retina) and 700-900nm (which is the spectral region least likely to be affected by the transmission of the anterior segment of the eye) were also separately investigated for texture measurements. Regarding the changes reported to be occurred in retinal vessels' walls in atherosclerosis patients, texture measures were calculated for different anatomical areas of the retina: over arterioles and venules, and in regions around arterioles and venules (separately).

6) Feature selection

Vessels' tortuosity, diameter and texture measures were calculated for both groups of data (i.e. ATH and CTL) as an initial set of features. In the next step, features that showed (uncorrected) significant difference between groups (t-test, $p<0.05$) were chosen for further combined analysis

in a classification task. Significant vasculature feature included arteriole diameter in zone B. Texture measures associated with spatial areas covering both arterioles and venules and adjacent regions, defined to be up to 70 μm away from the vessel's border, also showed (uncorrected) significant differences between the two groups.

To combine features into a single biomarker, a sequential feature selection was then conducted on the set of selected features mentioned above by repeatedly fitting multivariate normal densities with covariance estimates stratified by the two groups of data with different training and testing subsets (through a 10-fold cross-validation). As a result, arteriole diameter in Zone B, and 6 texture measures were selected as final set of features. Table5.1 summarizes the final features and their attributes.

Table 5.1 Seven features yielded by sequential feature selection

Feature code	Feature name	Feature Type	Anatomical region	Band(nm)	Direction
F1	diameter	Vasculature	arterioles – zone B	-	-
F2	Energy	Texture	arterioles and adjacent regions	450-550	spectral
F3	Correlation	"	venules	450-550	spectral
F4	Energy	"	venules and adjacent regions	450-550	spatial/spectral
F5	Correlation	"	arterioles	700-900	spatial/spectral
F6	Contrast	"	venules	700-900	spatial/spectral
F7	Correlation	"	venules	700-900	spatial/spectral

5.4 Results

Retinal arterioles of ATH subjects showed a lower mean diameter in zone B ($p<0.004$) compared to the control subjects. No significant difference was observed in tortuosity of either venules or arterioles of the two groups. Some of the textures measures of both arterioles and venules and adjacent regions at 450-550 nm and 700-900nm in spatial/spectral directions showed significant differences in ATH retinal images compared to CTL subjects. Figure 5.3 illustrates the data points for each selected feature.

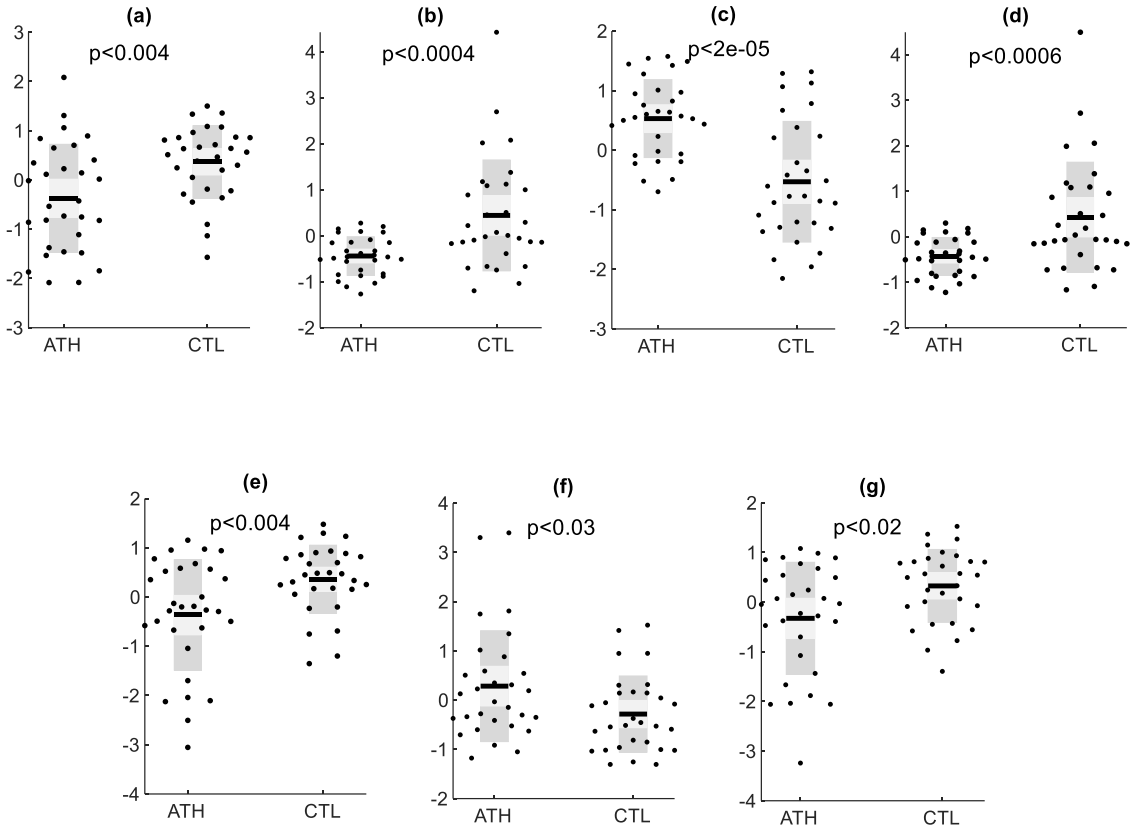

Figure 5.3 Difference between atherosclerosis and healthy control subjects corresponding to features F1 (a) to F7 (g) − values are normalized. Mean, SEM (light gray) and standard deviations (dark gray) and associated p values of the features are provided.

To discriminate atherosclerosis subjects from healthy controls, four classifiers were investigated: linear (LDA) and quadratic (QDA) discriminant analysis as well as support vector machines (SVM) with two types of kernels: linear and radial based function (rbf). 10-fold cross validation was conducted to evaluate classification loss of each classifier. A distribution of classification loss values was obtained by repetitive execution during 10-fold cross validation. Figure 5.4 (a) shows the classification loss of each classifier using features F1 to F7. LDA yielded the best results when compared to the other classifiers. To illustrate the effect of using different features in increasing the accuracy of the LDA classification, in Figure 5.4 (b), features F1 to F7 were step-by-step used to evaluate classification loss of the LDA classifier. Classification loss is decreased when using features F1 to F7 inclusively. Figure 5.4 (c) shows the distribution from each group in a 2D plane projection using first and second PCs of the selected features.

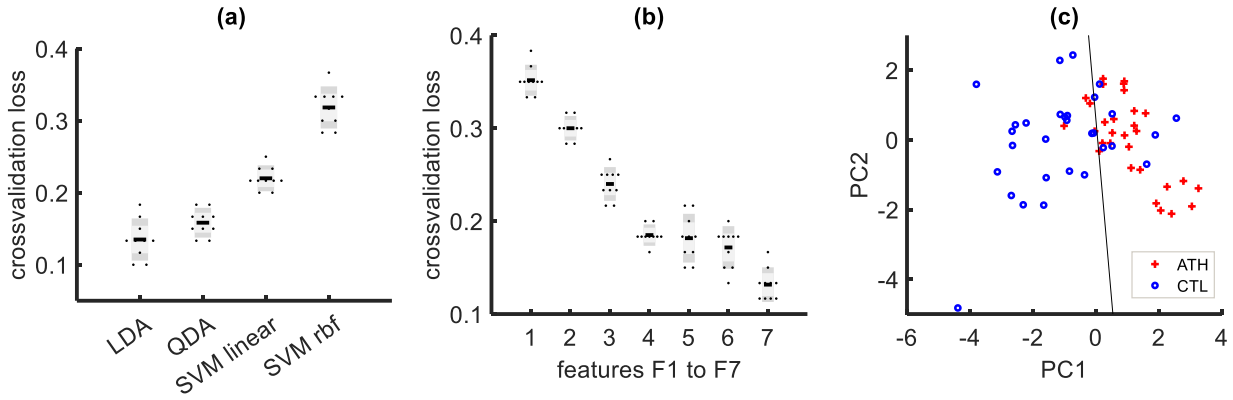

Figure 5.4 (a) Classification loss of four classifiers using features F1 to F7; (b) LDA classification loss using features F1 to F7 inclusively (c) data points in a 2D plane projection using PC1 and PC2 of the selected features.

Finally, Table 5.2 shows the sensitivity, specificity, positive predictive value (PPV) and negative predictive value (NPV) obtained with the LDA classifier and the 7 features using a 10-fold cross validation to measure errors.

Table 5.2 Classification performance based on features used

Sensitivity	Specificity	PPV	NPV	Accuracy
0.84±0.01	0.90±0.02	0.90±0.02	0.83±0.02	0.87±0.01

5.5 Discussion

In this work, we aimed to investigate a method to build novel biomarkers of atherosclerosis from retinal images. Exploiting data from a novel hyperspectral imaging platform, the study investigated several retinal features of images taken in patients with ATH and age-matched control subjects. We investigated retinal vasculature features, accessible through standard fundus imaging, including arterioles and venules caliber and tortuosity. Exploiting the increased information content of the imaging device, texture measures in spatial/spectral directions were also investigated in different anatomical regions including arterioles and venules and adjacent areas.

When studying vascular properties, we observed reduced arteriolar diameter in retinal zone B ($p<0.002$) and C ($p<0.04$) of ATH subjects when compared to control subjects. This supports recent findings on the association of narrower retinal arterioles with cardiovascular disease events

(Cheung et al., 2007; Gopinath et al., 2014; Seidelmann et al., 2016; Wang et al., 2008). In (Seidelmann et al., 2016), narrower retinal arterioles and wider retinal venules were associated with negative cardiovascular outcomes, narrower retinal arterioles were associated with lower hyperemic myocardial blood flow and perfusion reserve in asymptomatic adults (Wang et al., 2008). Narrower arteriolar caliber was also reported as a sign of concentric remodeling of the left ventricle (Cheung et al., 2007). In addition to retinal arteriolar narrowing, wider retinal venules were reported as a marker conferring a greater risk of CVD in woman (Seidelmann et al., 2016)(Gopinath et al., 2014). Although we did not observe significant difference in venular caliber, significant differences in textures of the image regions over venules and in adjacent areas were observed between the two groups. Retinal vessels tortuosity was anticipated to yield discriminatory information, however our comparison between groups did not reveal any significant difference. In the literature reviewed, Peña et al. (Peña et al., 2018) was the only study reporting that mean aortic IMT was associated with increased retinal arteriolar tortuosity. In addition to the vessels tortuosity and diameter, retinal arterio-venular nicking and fractal dimension have been also reported as signs of cardio vascular disease (Sharrett et al., 1999; Wong et al., 2007), biomarkers that could be further investigated in future studies.

Exploiting the hyperspectral nature of our acquisitions, we built texture measures that were spatially separated into regions over retinal vasculature and adjacent areas. Focussing on these measures, ATH subjects had significantly different texture values when compared to control subjects. These significant differences in texture measures were observed in the 450 to 550nm spectral range and between 700 and 900nm. Investigations of correlations between retinal texture measures and CVD events /risk factors have not been conducted so far and we anticipate to pursue these measures in longitudinal studies. Spatial-spectral properties reflect changes in tissue composition that modulate absorption and scattering of light and suggests that the hyperspectral acquisition is capturing independent biochemical changes not seen with standard fundus imaging. Using the same imaging system, we showed that there were correlations between retinal texture measures/vasculature attributes and cerebral amyloid status (J.-P. Soucy et al., 2018; Sharafi, Sylvestre, Chevrefils, Soucy, & Lesage, 2019).

We then used a combination of vasculature features and texture measures to automatically classify ATH and CTL subjects investigating the accuracy of different classifiers. Results showed that a

linear classifier could discriminate ATH subjects with an accuracy of 0.87±0.01%. Overall, this study suggests a potential for hyperspectral fundus imaging towards atherosclerosis identification and risk stratification of patients. Further work to explore serial monitoring of retinal images in correlation with disease time-course could help define a clinical scenario for fundus imaging in atherosclerosis.

5.6 References

Atherosclerosis | National Heart, Lung, and Blood Institute (NHLBI). (n.d.). Retrieved May 15, 2019, from https://www.nhlbi.nih.gov/health-topics/atherosclerosis

Blacher, J., Guerin, A. P., Pannier, B., Marchais, S. J., & London, G. M. (2001). Arterial calcifications, arterial stiffness, and cardiovascular risk in end-stage renal disease. Hypertension (Dallas, Tex.: 1979), 38(4), 938–942.

Cheung, N., Bluemke, D. A., Klein, R., Sharrett, A. R., Islam, F. M. A., Cotch, M. F., … Wong, T. Y. (2007). Retinal Arteriolar Narrowing and Left Ventricular Remodeling. Journal of the American College of Cardiology, 50(1), 48–55. https://doi.org/10.1016/j.jacc.2007.03.029

Chiu, M. H., Heydari, B., Batulan, Z., Maarouf, N., Subramanya, V., Schenck-Gustafsson, K., & O'Brien, E. R. (2018). Coronary artery disease in post-menopausal women: Are there appropriate means of assessment? Clinical Science (London, England: 1979), 132(17), 1937–1952. https://doi.org/10.1042/CS20180067

Couper, D. J., Klein, R., Hubbard, L. D., Wong, T. Y., Sorlie, P. D., Cooper, L. S., … Nieto, F. J. (2002). Reliability of retinal photography in the assessment of retinal microvascular characteristics: The atherosclerosis risk in communities study. American Journal of Ophthalmology, 133(1), 78–88. https://doi.org/10.1016/S0002-9394(01)01315-0

Desjardins, M., Sylvestre, J.-P., Jafari, R., Kulasekara, S., Rose, K., Trussart, R., … Lesage, F. (2016). Preliminary investigation of multispectral retinal tissue oximetry mapping using a hyperspectral retinal camera. Experimental Eye Research, 146, 330–340. https://doi.org/10.1016/j.exer.2016.04.001

Gopinath, B., Chiha, J., Plant, A. J. H., Thiagalingam, A., Burlutsky, G., Kovoor, P., … Mitchell, P. (2014). Associations between retinal microvascular structure and the severity and extent of coronary artery disease. Atherosclerosis, 236(1), 25–30. https://doi.org/10.1016/j.atherosclerosis.2014.06.018

Haralick, R. M., Shanmugam, K., & Dinstein, I. (1973). Textural Features for Image Classification. IEEE Transactions on Systems, Man, and Cybernetics, SMC-3(6), 610–621. https://doi.org/10.1109/TSMC.1973.4309314

Heitmar, R., Lip, G. Y. H., Ryder, R. E., & Blann, A. D. (2017). Retinal vessel diameters and reactivity in diabetes mellitus and/or cardiovascular disease. Cardiovascular Diabetology, 16(1). https://doi.org/10.1186/s12933-017-0534-6

Ikram, M. K., de Jong, F. J., Vingerling, J. R., Witteman, J. C. M., Hofman, A., Breteler, M. M. B., & de Jong, P. T. V. M. (2004). Are Retinal Arteriolar or Venular Diameters Associated with Markers for Cardiovascular Disorders? The Rotterdam Study. Investigative Opthalmology & Visual Science, 45(7), 2129. https://doi.org/10.1167/iovs.03-1390

J.-P. SOUCY, C. CHEVREFILS, J.-P. SYLVESTRE, S. BEAULIEU, T. A. PASCOAL, S. M. SHARAFI, … F. LESAGE. (2018). Validation of a hyperspectral retinal imaging method to predict cerebral amyloid PET status. 2018 Neuroscience Meeting Planner. Presented at the 2018 Neuroscience Meeting Planner, San Diego, CA.

Libby, P., Lichtman, A. H., & Hansson, G. K. (2013). Immune effector mechanisms implicated in atherosclerosis: From mice to humans. Immunity, 38(6), 1092–1104. https://doi.org/10.1016/j.immuni.2013.06.009

Lorenz, M. W., Markus, H. S., Bots, M. L., Rosvall, M., & Sitzer, M. (2007). Prediction of clinical cardiovascular events with carotid intima-media thickness: A systematic review and meta-analysis. Circulation, 115(4), 459–467. https://doi.org/10.1161/CIRCULATIONAHA.106.628875

McClintic, B. R., McClintic, J. I., Bisognano, J. D., & Block, R. C. (2010). The Relationship between Retinal Microvascular Abnormalities and Coronary Heart Disease: A Review. The

American Journal of Medicine, 123(4), 374.e1-374.e7. https://doi.org/10.1016/j.amjmed.2009.05.030

McGeechan, K., Liew, G., Macaskill, P., Irwig, L., Klein, R., Klein, B. E. K., … Wong, T. Y. (2009). Prediction of Incident Stroke Events Based on Retinal Vessel Caliber: A Systematic Review and Individual-Participant Meta-Analysis. American Journal of Epidemiology, 170(11), 1323–1332. https://doi.org/10.1093/aje/kwp306

Mitchell, G. F., Hwang, S.-J., Vasan, R. S., Larson, M. G., Pencina, M. J., Hamburg, N. M., … Benjamin, E. J. (2010). Arterial stiffness and cardiovascular events: The Framingham Heart Study. Circulation, 121(4), 505–511. https://doi.org/10.1161/CIRCULATIONAHA.109.886655

More, S. S., & Vince, R. (2015). Hyperspectral Imaging Signatures Detect Amyloidopathy in Alzheimer's Mouse Retina Well before Onset of Cognitive Decline. ACS Chemical Neuroscience, 6(2), 306–315. https://doi.org/10.1021/cn500242z

Nambi, V., Chambless, L., He, M., Folsom, A. R., Mosley, T., Boerwinkle, E., & Ballantyne, C. M. (2012a). Common carotid artery intima-media thickness is as good as carotid intima-media thickness of all carotid artery segments in improving prediction of coronary heart disease risk in the Atherosclerosis Risk in Communities (ARIC) study. European Heart Journal, 33(2), 183–190. https://doi.org/10.1093/eurheartj/ehr192

Nambi, V., Chambless, L., He, M., Folsom, A. R., Mosley, T., Boerwinkle, E., & Ballantyne, C. M. (2012b). Common carotid artery intima-media thickness is as good as carotid intima-media thickness of all carotid artery segments in improving prediction of coronary heart disease risk in the Atherosclerosis Risk in Communities (ARIC) study. European Heart Journal, 33(2), 183–190. https://doi.org/10.1093/eurheartj/ehr192

Niu, L., Zhang, Y., Meng, L., Xiao, Y., Wong, K. K. L., Abbott, D., … Qian, M. (2014). Detection of Subclinical Atherosclerosis in Asymptomatic Subjects Using Ultrasound Radiofrequency-Tracking Technology. PLoS ONE, 9(11). https://doi.org/10.1371/journal.pone.0111926

Niu, L., Zhang, Y., Qian, M., Meng, L., Xiao, Y., Wang, Y., … Zheng, H. (2013). Impact of multiple cardiovascular risk factors on carotid intima-media thickness and elasticity. PloS One, 8(7), e67809. https://doi.org/10.1371/journal.pone.0067809

Patasius, M., Marozas, V., Jegelevicius, D., & Lukosevicius, A. (2005). Evaluation of tortuosity of eye blood vessels using the integral of square of derivative of curvature. IFMBE Proc. 3rd Eur. Med. Biol. Eng. Conf.(EMBEC05), 11.

Patel, S. R., Flanagan, J. G., Shahidi, A. M., Sylvestre, J.-P., & Hudson, C. (2013). A prototype hyperspectral system with a tunable laser source for retinal vessel imaging. Investigative Ophthalmology & Visual Science, 54(8), 5163–5168. https://doi.org/10.1167/iovs.13-12124

Peña, A. S., Liew, G., Anderson, J., Giles, L. C., Gent, R., Wong, T. Y., & Couper, J. J. (2018). Early atherosclerosis is associated with retinal microvascular changes in adolescents with type 1 diabetes. Pediatric Diabetes, 19(8), 1467–1470. https://doi.org/10.1111/pedi.12764

Publishing, H. H. (n.d.). Atherosclerosis. Retrieved May 15, 2019, from Harvard Health website: https://www.health.harvard.edu/a_to_z/atherosclerosis-a-to-z

Seidelmann, S. B., Claggett, B., Bravo, P. E., Gupta, A., Farhad, H., Klein, B. E., … Solomon, S. D. (2016). Retinal Vessel Calibers in Predicting Long-Term Cardiovascular Outcomes: The Atherosclerosis Risk in Communities Study. Circulation, 134(18), 1328–1338. https://doi.org/10.1161/CIRCULATIONAHA.116.023425

Sharafi, S. M., Sylvestre, J.-P., Chevrefils, C., Soucy, J.-P., & Lesage, F. (2019). Correlation between PET-derived cerebral amyloid status and retinal image features using a hyperspectral fundus camera. In S. J. Madsen, V. X. D. Yang, & N. V. Thakor (Eds.), Clinical and Translational Neurophotonics 2019 (p. 20). https://doi.org/10.1117/12.2508557

Sharrett, A. R., Hubbard, L. D., Cooper, L. S., Sorlie, P. D., Brothers, R. J., Nieto, F. J., … Klein, R. (1999). Retinal Arteriolar Diameters and Elevated Blood Pressure: The Atherosclerosis Risk in Communities Study. American Journal of Epidemiology, 150(3), 263–270. https://doi.org/10.1093/oxfordjournals.aje.a009997

Sundholm, J., Gustavsson, T., & Sarkola, T. (2014). Semi-automatic border detection software for the quantification of arterial lumen, intima-media and adventitia layer thickness with very-high resolution ultrasound. Atherosclerosis, 234(2), 283–287. https://doi.org/10.1016/j.atherosclerosis.2014.03.006

Tedeschi-Reiner, E., Strozzi, M., Skoric, B., & Reiner, Z. (2005). Relation of Atherosclerotic Changes in Retinal Arteries to the Extent of Coronary Artery Disease. The American Journal of Cardiology, 96(8), 1107–1109. https://doi.org/10.1016/j.amjcard.2005.05.070

Wang, L., Wong, T. Y., Sharrett, A. R., Klein, R., Folsom, A. R., & Jerosch-Herold, M. (2008). Relationship between retinal arteriolar narrowing and myocardial perfusion: Multi-ethnic study of atherosclerosis. Hypertension (Dallas, Tex.: 1979), 51(1), 119–126. https://doi.org/10.1161/HYPERTENSIONAHA.107.098343

Wong, T. Y., Cheung, N., Islam, F. M. A., Klein, R., Criqui, M. H., Cotch, M. F., … Sharrett, A. R. (2007). Relation of Retinopathy to Coronary Artery Calcification: The Multi-Ethnic Study of Atherosclerosis. American Journal of Epidemiology, 167(1), 51–58. https://doi.org/10.1093/aje/kwm256

CHAPTER 6 GENERAL DISCUSSION

In this thesis, the prediction ability of hyperspectral and vasculature features extracted from retinal images were investigated with the aim of finding biomarkers of Alzheimer's disease and atherosclerosis. Two scientific papers were presented in Chapters 4 and 5, focusing on the Alzheimer's and atherosclerosis retinal biomarker respectively. Based on the objectives initially proposed in Chapter 1, this chapter summarizes the research findings, gives interpretations of the results and discusses the limitations of the current methods and possible improvements that could be considered.

6.1 Objective 1

The first objective of this thesis was to investigate spatial/spectral image features of retinal arterioles and venules and adjacent tissues in a cohort of AD positive and control subjects with the goal of identifying biomarkers of AD based on data accumulated using a hyper-spectral retinal imaging device. The article presented in Chapter 4 addressed this objective by evaluating a combination of vasculature and spatial/spectral texture measures against burden of Aβ in the brain determined by amyloid-PET. The studied cohort included 138 retinal images of 20 cognitively impaired and 26 cognitively unimpaired cases (1 to 3 images per subject). Following PET amyloid imaging, 7 out of 20 cognitively impaired cases were identified as amyloid negative, while 3 of the 26 cognitively unimpaired subjects were amyloid positive. Retinal image features showed correlations to both cerebral amyloid status (Chapter 4) and cognitive test results (Appendix A.1).

Retinal arterioles' and venules' tortuosity in Aβ+ subjects were significantly higher than Aβ- ($p<0.002$, $p<1.6e-6$). Moreover, retinal arterioles' and venules' tortuosity in cognitively impaired subjects were significantly higher than the cognitively unimpaired subjects ($p<0.002$, $p<0.0002$). This supports recent findings on the correlation between retinal vessels tortuosity and AD (Brown & Thore, 2011; C. Y. Cheung et al., 2014; Frost et al., 2013; Williams et al., 2015). We also quantitatively showed that retinal arterioles' diameters of Aβ+ subjects in zone A are higher than of the controls ($p<0.02$). This finding is in contradiction with Cheung et al. (2014) that reported reduction in retinal vessel caliber in AD patients; however, it supports findings of a larger study conducted by Williams et. al (Williams et al., 2015) reporting that mean CRAE of AD patients were higher than the control subjects. Querques et al. in (Querques et al., 2019) also reported that

CRAE is correlated with the burden of phosphorylated-tau protein in CFS—one of the biomarkers found in CFS of AD patients.

As mentioned in Section 2.1.2, characterizing Aβ deposition in retina of AD mice and human retinal tissue ex vivo, have been widely addressed in the literature as biomarkers of AD. However, in our study, direct imaging of amyloid plaques in the retina of AD subjects (in vivo) was challenging due to the plaques size being comparable to optical resolution of the HSI device. Therefore, we postulated that texture analysis could potentially resolve this issue by investigating the variation of the gray levels of the neighboring pixels that may arise because of Aβ deposition in retina. Based on this idea, different texture measures were extracted from vessels and surrounding tissues along the spatial/spectral dimensions available in the HSI. We observed that texture measures taken over retinal arterioles and adjacent regions ($p<1e-6$) of Aβ+ subjects are significantly different from retinal images of Aβ- subjects. The differences in texture measures were observed in the spectral ranges of 450 to 550nm. This range is known as the spectral region most likely to be affected by scattering from amyloid aggregates in the retina. Moreover, we observed significant differences in texture measures in the spectral range 700 to 900nm ($p<0.0008$) which is the spectral region least likely to be affected by the transmission of the anterior segment of the eye. Another striking findings was that the p-values corresponding to one of the texture measures i.e. correlation of arterioles and adjacent region at 450-550 nm significantly decreased compared to when the cerebral amyloid status was used as gold standard (see Appendix A). Since the appearance of Aβ plaques often occur many years before clinical symptoms (Perrin, Fagan, & Holtzman, 2009), our later finding motivates further study on the effectiveness of the mentioned feature as a retinal biomarker that correlates with the development of the disease.

We showed that a combination of vasculature features and spatial/spectral texture measures could be used to discriminate Aβ+ from Aβ- subjects using a SVM classifier with a classification loss of 0.14 ± 0.005 and accuracy of 85%.

Spectral changes were also reported in Alzheimer's mice relative to age-matched wild-type mice ex vivo (More & Vince, 2015) and in vivo (More, Beach, & Vince, 2016) using label-free reflectance hyperspectral retinal images. As mentioned earlier, a similar trend was also observed in human brain and retina tissue ex vivo. These findings support our results that hyperspectral retinal imaging could be used to identify amyloid-related signs of AD without extraneous labeling.

In Chapters 1 and 2, the use of different imaging techniques in the literature for investigating retinal biomarkers of AD were reviewed. OCT-based imaging has allowed observation of histological details of the retinal layers and optic nerve with high resolution (4 μm axial resolution). It is currently being applied to various CNS neurodegenerative diseases (Kesler et al., 2011) by measuring retinal nerve fibre layer loss and has been demonstrated to show nerve fiber deficits in AD (Berisha et al., 2007; Jindahra, Hedges, Mendoza-Santiesteban, & Plant, 2010; Paquet et al., 2007; Parisi et al., 2001). However, nerve fiber deficits are also observed in glaucoma, MCI (Paquet et al., 2007) and Parkinson's disease (Jiménez-Jiménez, Alonso-Navarro, García-Martín, & Agúndez, 2014; Lee et al., 2014) and thus is not specific to AD. Moreover, while OCT-based techniques provide 'topography' of a tissue region, HSI gives information about its nature by reveling the spectral signatures of backscatters within the tissue that may remained uncovered in OCT images (Dontu, Miclos, Savastru, & Tautan, 2017). However, none of the studies conducted so far claimed that the HSI is aimed to substitute the OCT in the context of investigating retinal biomarkers of AD. Instead, a combination of the two techniques could be best used for identifying tissue-related characteristics in retina to detect possible signs of the disease.

Optical fluorescence imaging of the retina, with fluorescent label curcumin, was also proposed to detect the Aβ plaques (Koronyo-Hamaoui et al., 2011) and recently tested in vivo in AD subjects (Shaun Frost et al., 2014; Koronyo et al., 2017). However, the latter study involved two visits by volunteers for retinal imaging with the oral administration of a curcumin between appointments. This study also requires blood testing to confirm curcumin uptake. These limitations make the method difficult to be used for popular screening.

As a conclusion, this study suggests that a combination of vasculature metrics and features extracted from hyperspectral retinal images has a potential to detect a signal likely related to Aβ plaques in the retina of AD subjects using a non-invasive eye scan.

6.2 Objective 2

The second objective of this thesis was to find retinal image features and evaluate their prediction ability to discern between atherosclerosis and healthy control participants using the same hyper-spectral retinal imaging device. The article presented in Chapter 5 addressed this objective by

evaluating a combination of retinal image features including arterioles and venules diameter and tortuosity and spatial/spectral texture measures associated with different anatomical regions including arterioles, venules and adjacent tissues. The studied cohort (n=60) included 30 clinically probable ATH and 30 age-matched control cases.

Investigating vascular metrics, we observed narrowing of the arterioles in retinal zone B ($p<0.002$) and zone C ($p<0.04$) of ATH subjects when compared to control subjects. This supports recent findings on the association of narrower retinal arterioles with cardiovascular diseases and events (N. Cheung et al., 2007; Gopinath et al., 2014; Seidelmann et al., 2016; Wang et al., 2008). Seidelmann et al.(2016), reported that narrower retinal arterioles and wider retinal venules were associated with negative cardiovascular outcomes, narrower retinal arterioles were associated with lower hyperemic myocardial blood flow and perfusion reserve in asymptomatic adults (Wang et al., 2008). Narrower arteriolar caliber was also reported as a sign of concentric remodeling of the left ventricle (N. Cheung et al., 2007). In addition to retinal arteriolar narrowing, wider retinal venules was also reported as a marker conferring a greater risk of CVD in woman (Gopinath et al., 2014; Seidelmann et al., 2016). Although we did not observe significant difference in venular caliber, significant differences in image textures of the regions over venules and surrounding tissues were observed between the two groups.

We built texture measures covering both spatial and spectral variations in intensities across differing wavelengths separated into regions over retinal arterioles and venules and adjacent tissues. Focussing on these measures, ATH subjects not only had significantly different texture values over retinal venules and adjacent tissues but also they had significantly different texture values over arterioles and tissue around when compared to control subjects. These significant differences in texture measures were observed in the 450 to 550nm spectral range and between 700 and 900nm. The idea behind using these spectral ranges in the context of atherosclerosis study was that 700-900nm is the band least likely to be affected by the opacification of the eye lens and cataracts, whereas, 450 to 550nm is the spectral range in which contrast between vessels and the background retina become optimized.

Significant differences observed in texture values of retinal vessels and around tissues can support the reported small-scaled changes occurred at retinal vessels' walls and associated endothelial

dysfunction in patients with ATH (Adzhemian et al., 2016; Delles et al., 2004; Heitmar et al., 2017b; Kotliar et al., 2011; Mandecka et al., 2007; Reimann et al., 2009)

Investigations of correlations between retinal texture measures and CVD events /risk factors have not been conducted so far and we anticipate pursuing these measures in longitudinal studies.

As another vasculature characteristic, retinal vessels tortuosity was anticipated to yield discriminatory information, however our comparison between groups did not reveal any significant difference. In the literature reviewed, Peña et al. (Peña et al., 2018) was the only study reporting that mean aortic IMT was associated with increased retinal arteriolar tortuosity. In addition to the vessels tortuosity and diameter, retinal arterio-venular nicking and fractal dimension have been also reported as signs of cardio vascular disease (Sharrett et al., 1999; T. Y. Wong et al., 2007), biomarkers that could be further investigated in future studies.

In the article presented in Chapter 5 we used combination of the extracted vasculature features and spectral and spatial-spectral texture measures to automatically classify ATH and CTL subjects. Results showed that a linear classifier using the mentioned features could discriminate ATH subjects with an accuracy of 0.87±0.01. However, as an alternate approach, when we combine spatial (instead of spatial/spectral) and spectral texture measures we could discriminate ATH from CTL subjects with an accuracy of 0.9 using a quadratic classifier (see Appendix A.2).

As a conclusion, this study suggests that using data-rich hyperspectral retinal images could be used to identify atherosclerosis using a non-invasive eye scan. Further work to explore serial monitoring of retinal images in correlation with disease time-course could help define a clinical scenario for fundus imaging in atherosclerosis.

Overall to both studies, spatial/spectral properties in HSI, reflect changes in tissue composition that modulate absorption and scattering along a wide spectrum of light. Thus, it is capable of capturing independent biochemical changes that are not seen with standard fundus imaging and OCT-based techniques. This study showed that a combination of hyperspectral retinal features and retinal vasculature metrics could be potentially used to detect signs of AD and ATH through a simple, non-invasive eye scan.

6.3 Limitations of using hyperspectral imaging technique and data analysis methods

Taking the advantages of hyperspectral retinal imaging could bring about specific challenges in addition to the common challenges associated with conventional fundus imaging. In contrast to ex vivo retinal imaging, safety-based limitations on the amount of illumination, cause in vivo images of the retina to be consisting of low contrast regions without clear boundaries. Large imaging apertures can gather more light but simultaneously leads to a small depth of focus. Consequently, depth variations may cause different degrees of blurriness due to defocusing of the camera. On the other hand, an increase of exposure time may incur blur due to the eye movements (Abràmoff et al., 2010).

Eye movements (saccades, slow drifts, etc.) during HSI also have a negative influence on the quality of retinal images: During the exposure time needed to acquire the images at different wavelengths, eye movements cause the pixels of the images in the hyperspectral cube, not to be located at the same position on the retina through all wavelengths. As described in Section 3.2.1, registration methods were applied to resolve this issue; however, correcting eye movements by registration to align retinal images into a montage, brings about new kind of errors, i.e. registration errors that affect the image quality on their own.

Parasitic reflections are another source of errors that were observed in most subjects with an intraocular lens (operated for cataract). As mentioned earlier in this chapter, this type of noise mostly affects images taken at 450–700 nm compared to 700-900 nm. Improvement in the device optics by avoiding undesired reflections from specific regions of the surface is currently on going by the device producers to reduce this kind of noise.

The mentioned challenges (i.e. focusing issues, registration errors, and parasitic reflections) affected the accuracy of the consequent image analysis tasks like vessels segmentation and texture measurements. Moreover, those errors were the source of intra-subject and overall variability in the spatial/spectral features space for some subjects, when more than one acquisition of each subject were available. Although based on the comparison made between the features' values of different acquisitions of the same subjects, intra-subject variability was less than 15%, it suggests

further optimization efforts in device optics and the image analysis pipeline for decreasing the variability of the results.

As explained in Sections 4.4 and 5.4, we compared linear, quadratic and SVM classifiers for the discrimination of ATH and Aβ+ groups from their corresponding control groups. However, investigating other classifiers (e.g. neural networks) could result in different classification performance and make it possible to conduct a more comprehensive comparison.

As mentioned in Chapter 2, in addition to vessels tortuosity and diameter measurements (that we investigated in this thesis), other vasculature measures like changes in fractional dimension and AV nicking were also addressed in the literature as the biomarkers of both AD and ATH. These two measures could be investigated as additional discriminative features to improve classifications accuracy in both studies.

There were some issues recruiting sufficient human subjects in a timely manner. Ethical approval process, delays due to technical problems, and cancellation and rescheduling of several PET imaging appointments due to patients' health issues specifically in AD study, reduced the sample size. However, larger sample sizes will improve the statistical power of the comparisons and increase the reliability of the results in future work.

CHAPTER 7 CONCLUSION AND RECOMMENDATION

In this thesis, a non-invasive hyperspectral retinal imaging platform was used to investigate biomarkers of Alzheimer's disease and atherosclerosis.

A significant, growing body of the literature has shown that long chronic conditions like Alzheimer's disease and atherosclerosis have manifestations in retina. However, most of the studies conducted so far, investigated monochromic or RGB retinal images that do not allow for analyzing "spectral tissue-related characteristics" of the retina. Acquiring images using different monochromic wavelengths on the other hand, provides us with the relative scatterings across a wider range of light spectrum.

Regarding the reported changes occur to the retinal tissue because of AD and ATH, analyzing the data-rich hyperspectral retinal images was anticipated to yield, hidden tissue-related discriminatory information that might remain uncovered by the conventional imaging techniques. Taking the advantages of hyperspectral imaging, we could exploit spatial-spectral features from retinal vessels and adjacent tissues. Investigated features, consisted of vasculature characteristics (i.e. vessels' tortuosity and diameter) and texture measures in spatial and spectral directions. We showed that a combination of extracted features could yield discriminatory information in different contexts of cerebral amyloid status, cognitive impairment, and atherosclerosis.

In the context of Alzheimer's disease, we evaluated vasculature and texture measures against the burden of Aβ in the brain measured by amyloid-PET imaging. Classification results showed that the mentioned features could discern Aβ-positives from age-matched Aβ-negative subjects with good accuracy. Therefore, the proposed research introduced a method that potentially could be used to detect a signal likely related to Aβ plaques in the retina of AD subjects and validate the method against brain Aβ plaques imaging with amyloid-binding PET tracers. This research is expected to help the early detection of AD using a cost-effective and non-invasive eye scan.

Currently diagnosis of atherosclerosis rely on measuring carotid IMT and arterial stiffness using B-mode ultrasound and echo tracking. These methods have been reported to be expensive, time-consuming and their accuracy is highly dependent on the operator. Literature has shown that early signs of atherosclerosis could be identified in fundoscopic images. We evaluated retinal vasculature and texture features from our hyperspectral retinal images with the goal of identifying biomarkers

of atherosclerosis and their prediction ability. Our cross-sectional study showed that hyperspectral image analysis could discern atherosclerosis subjects from control subjects with good accuracy.

However, the results from this study also suggested that further work is needed to replicate our findings and establish whether the identified biomarkers can be extended to provide predictive outcomes in longitudinal studies in both contexts of AD and ATH.

REFERENCES

Abdalla, M., Hunter, A., & Al-Diri, B. (2015). Quantifying retinal blood vessels' tortuosity—Review. *2015 Science and Information Conference (SAI)*, 687–693. https://doi.org/10.1109/SAI.2015.7237216

Abràmoff, M. D., Garvin, M. K., & Sonka, M. (2010). Retinal Imaging and Image Analysis. *IEEE Reviews in Biomedical Engineering*, *3*, 169–208. https://doi.org/10.1109/RBME.2010.2084567

Adzhemian, N., Neroev, V., Kiseleva, T., Ezhov, M., Balatskaya, N., Ilina, N., & Tankovskiy, V. (2016). Retinal vascular caliber, ocular blood flow and endothelin-1 level in blood serum in patients with subclinical atherosclerosis. *Atherosclerosis*, *252*, e194. https://doi.org/10.1016/j.atherosclerosis.2016.07.891

Anyfanti, P., Triantafyllou, A., Gkaliagkousi, E., Koletsos, N., Athanasopoulos, G., Zabulis, X., … Douma, S. (2017). Retinal vessel morphology in rheumatoid arthritis: Association with systemic inflammation, subclinical atherosclerosis, and cardiovascular risk. *Microcirculation*, *24*(8), e12417. https://doi.org/10.1111/micc.12417

Ascaso, F. J., Cruz, N., Modrego, P. J., Lopez-Anton, R., Santabárbara, J., Pascual, L. F., … Cristóbal, J. A. (2014). Retinal alterations in mild cognitive impairment and Alzheimer's disease: An optical coherence tomography study. *Journal of Neurology*, *261*(8), 1522–1530. https://doi.org/10.1007/s00415-014-7374-z

Atherton, T. J., & Kerbyson, D. J. (1999). *Size Invariant Circle Detection*.

Baker, M. L., Hand, P. J., Wang, J. J., & Wong, T. Y. (2008). Retinal signs and stroke: Revisiting the link between the eye and brain. *Stroke*, *39*(4), 1371–1379. https://doi.org/10.1161/STROKEAHA.107.496091

Bandos, T. V., Bruzzone, L., & Camps-Valls, G. (2009). Classification of Hyperspectral Images With Regularized Linear Discriminant Analysis. *IEEE Transactions on Geoscience and Remote Sensing*, *47*(3), 862–873. https://doi.org/10.1109/TGRS.2008.2005729

Beach, T. G., Monsell, S. E., Phillips, L. E., & Kukull, W. (2012). Accuracy of the clinical diagnosis of Alzheimer disease at National Institute on Aging Alzheimer Disease Centers, 2005-2010. *Journal of Neuropathology and Experimental Neurology*, *71*(4), 266–273. https://doi.org/10.1097/NEN.0b013e31824b211b

Berisha, F., Feke, G. T., Trempe, C. L., McMeel, J. W., & Schepens, C. L. (2007). Retinal Abnormalities in Early Alzheimer's Disease. *Investigative Opthalmology & Visual Science*, *48*(5), 2285. https://doi.org/10.1167/iovs.06-1029

Bild, D. E., Bluemke, D. A., Burke, G. L., Detrano, R., Diez Roux, A. V., Folsom, A. R., … Tracy, R. P. (2002). Multi-Ethnic Study of Atherosclerosis: Objectives and design. *American Journal of Epidemiology*, *156*(9), 871–881.

Blennow, K., Mattsson, N., Schöll, M., Hansson, O., & Zetterberg, H. (2015). Amyloid biomarkers in Alzheimer's disease. *Trends in Pharmacological Sciences*, *36*(5), 297–309. https://doi.org/10.1016/j.tips.2015.03.002

Bloom, G. S. (2014). Amyloid-β and tau: The trigger and bullet in Alzheimer disease pathogenesis. *JAMA Neurology*, *71*(4), 505–508. https://doi.org/10.1001/jamaneurol.2013.5847

Bonetti, P. O., Lerman, L. O., & Lerman, A. (2003). Endothelial dysfunction: A marker of atherosclerotic risk. *Arteriosclerosis, Thrombosis, and Vascular Biology*, *23*(2), 168–175.

Bories, G. F. P., & Leitinger, N. (2017). Macrophage metabolism in atherosclerosis. *FEBS Letters*, *591*(19), 3042–3060. https://doi.org/10.1002/1873-3468.12786

Campbell, M. C. W., De Vries, D., Emptage, L., Cookson, C., Kisilak, M., Bueno, J. M., & Avila, F. J. (2015). Polarization Properties of Amyloid Beta in the Retina of the Eye as a Biomarker of Alzheimer's Disease. *Optics in the Life Sciences*, BM3A.4. https://doi.org/10.1364/BODA.2015.BM3A.4

Chandra, A., Seidelmann, S., Claggett, B., Klein, R., Klein, B., Shah, A., & Solomon, S. (2018). ASSOCIATION BETWEEN RETINAL VESSEL CALIBERS AND LONG-TERM CARDIAC STRUCTURE AND FUNCTION: THE ATHEROSCLEROSIS RISK IN COMMUNITIES (ARIC) STUDY. *Journal of the American College of Cardiology*, *71*(11, Supplement), A1898. https://doi.org/10.1016/S0735-1097(18)32439-2

Cheung, C. Y., Ong, Y. T., Hilal, S., Ikram, M. K., Low, S., Ong, Y. L., … Wong, T. Y. (2015). Retinal Ganglion Cell Analysis Using High-Definition Optical Coherence Tomography in Patients with Mild Cognitive Impairment and Alzheimer's Disease. *Journal of Alzheimer's Disease*, *45*(1), 45–56. https://doi.org/10.3233/JAD-141659

Cheung, C. Y., Ong, Y. T., Ikram, M. K., Ong, S. Y., Li, X., Hilal, S., … Wong, T. Y. (2014). Microvascular network alterations in the retina of patients with Alzheimer's disease. *Alzheimer's & Dementia*, *10*(2), 135–142. https://doi.org/10.1016/j.jalz.2013.06.009

Cheung, N., Bluemke, D. A., Klein, R., Sharrett, A. R., Islam, F. M. A., Cotch, M. F., … Wong, T. Y. (2007). Retinal Arteriolar Narrowing and Left Ventricular Remodeling. *Journal of*

the American College of Cardiology, *50*(1), 48–55. https://doi.org/10.1016/j.jacc.2007.03.029

Cheung, N., Mitchell, P., & Wong, T. Y. (2010). Diabetic retinopathy. *Lancet (London, England)*, *376*(9735), 124–136. https://doi.org/10.1016/S0140-6736(09)62124-3

Chiu, M. H., Heydari, B., Batulan, Z., Maarouf, N., Subramanya, V., Schenck-Gustafsson, K., & O'Brien, E. R. (2018). Coronary artery disease in post-menopausal women: Are there appropriate means of assessment? *Clinical Science (London, England: 1979)*, *132*(17), 1937–1952. https://doi.org/10.1042/CS20180067

Couper, D. J., Klein, R., Hubbard, L. D., Wong, T. Y., Sorlie, P. D., Cooper, L. S., … Nieto, F. J. (2002). Reliability of retinal photography in the assessment of retinal microvascular characteristics: The atherosclerosis risk in communities study. *American Journal of Ophthalmology*, *133*(1), 78–88. https://doi.org/10.1016/S0002-9394(01)01315-0

Cristianini, N., & Shawe-Taylor, J. (2000). *An Introduction to Support Vector Machines: And Other Kernel-based Learning Methods*. New York, NY, USA: Cambridge University Press.

de Jong, F. J., Schrijvers, E. M. C., Ikram, M. K., Koudstaal, P. J., de Jong, P. T. V. M., Hofman, A., … Breteler, M. M. B. (2011). Retinal vascular caliber and risk of dementia: The Rotterdam study. *Neurology*, *76*(9), 816–821. https://doi.org/10.1212/WNL.0b013e31820e7baa

Delles, C., Michelson, G., Harazny, J., Oehmer, S., Hilgers, K. F., & Schmieder, R. E. (2004). Impaired endothelial function of the retinal vasculature in hypertensive patients. *Stroke*, *35*(6), 1289–1293. https://doi.org/10.1161/01.STR.0000126597.11534.3b

Desjardins, M., Sylvestre, J.-P., Jafari, R., Kulasekara, S., Rose, K., Trussart, R., … Lesage, F. (2016). Preliminary investigation of multispectral retinal tissue oximetry mapping using a hyperspectral retinal camera. *Experimental Eye Research*, *146*, 330–340. https://doi.org/10.1016/j.exer.2016.04.001

Dontu, S., Miclos, S., Savastru, D., & Tautan, M. (2017). Combined spectral-domain optical coherence tomography and hyperspectral imaging applied for tissue analysis: Preliminary results. *Applied Surface Science*, *417*, 119–123. https://doi.org/10.1016/j.apsusc.2017.03.175

Doraiswamy, P. M., Sperling, R. A., Johnson, K., Reiman, E. M., Wong, T. Z., Sabbagh, M. N., … Pontecorvo, M. J. (2014). Florbetapir F 18 amyloid PET and 36-month cognitive decline:a prospective multicenter study. *Molecular Psychiatry*, *19*(9), 1044–1051. https://doi.org/10.1038/mp.2014.9

Dougherty, G., & Varro, J. (2000). A quantitative index for the measurement of the tortuosity of blood vessels. *Medical Engineering & Physics*, *22*(8), 567–574.

Dubois, B., Feldman, H. H., Jacova, C., Hampel, H., Molinuevo, J. L., Blennow, K., … Cummings, J. L. (2014). Advancing research diagnostic criteria for Alzheimer's disease: The IWG-2 criteria. *The Lancet. Neurology*, *13*(6), 614–629. https://doi.org/10.1016/S1474-4422(14)70090-0

Feke, G. T., Hyman, B. T., Stern, R. A., & Pasquale, L. R. (2015). Retinal blood flow in mild cognitive impairment and Alzheimer's disease. *Alzheimer's & Dementia: Diagnosis, Assessment & Disease Monitoring*, *1*(2), 144–151. https://doi.org/10.1016/j.dadm.2015.01.004

Flammer, J., Konieczka, K., Bruno, R. M., Virdis, A., Flammer, A. J., & Taddei, S. (2013). The eye and the heart. *European Heart Journal*, *34*(17), 1270–1278. https://doi.org/10.1093/eurheartj/eht023

Frost, S., Kanagasingam, Y., Sohrabi, H., Vignarajan, J., Bourgeat, P., Salvado, O., … the AIBL Research Group. (2013). Retinal vascular biomarkers for early detection and monitoring of Alzheimer's disease. *Translational Psychiatry*, *3*(2), e233. https://doi.org/10.1038/tp.2012.150

Frost, Shaun, Kanagasingam, Y., Macaulay, L., Koronyo-Hamaoui, M., Koronyo, Y., Biggs, D., … Martins, R. (2014). RETINAL AMYLOID FLUORESCENCE IMAGING PREDICTS CEREBRAL AMYLOID BURDEN AND ALZHEIMER'S DISEASE. *Alzheimer's & Dementia: The Journal of the Alzheimer's Association*, *10*(4), P234–P235. https://doi.org/10.1016/j.jalz.2014.04.341

Hastie, T., Tibshirani, R., & Friedman, J. (2009). *The Elements of Statistical Learning: Data Mining, Inference, and Prediction, Second Edition* (2nd ed.). Retrieved from https://www.springer.com/de/book/9780387848570

Heitmar, R., Lip, G. Y. H., Ryder, R. E., & Blann, A. D. (2017a). Retinal vessel diameters and reactivity in diabetes mellitus and/or cardiovascular disease. *Cardiovascular Diabetology*, *16*(1). https://doi.org/10.1186/s12933-017-0534-6

Heitmar, R., Lip, G. Y. H., Ryder, R. E., & Blann, A. D. (2017b). Retinal vessel diameters and reactivity in diabetes mellitus and/or cardiovascular disease. *Cardiovascular Diabetology*, *16*(1), 56. https://doi.org/10.1186/s12933-017-0534-6

Huang, D., Swanson, E. A., Lin, C. P., Schuman, J. S., Stinson, W. G., Chang, W., … Et, A. (1991). Optical coherence tomography. *Science*, *254*(5035), 1178–1181. https://doi.org/10.1126/science.1957169

Jagust, W. (2016). Is amyloid-β harmful to the brain? Insights from human imaging studies. *Brain*, *139*(1), 23–30. https://doi.org/10.1093/brain/awv326

James, G., Witten, D., Hastie, T., & Tibshirani, R. (2013). *An Introduction to Statistical Learning: With Applications in R*. Retrieved from https://www.springer.com/gp/book/9781461471370

Javaid, F. Z., Brenton, J., Guo, L., & Cordeiro, M. F. (2016). Visual and Ocular Manifestations of Alzheimer's Disease and Their Use as Biomarkers for Diagnosis and Progression. *Frontiers in Neurology*, *7*. https://doi.org/10.3389/fneur.2016.00055

Jindahra, P., Hedges, T. R., Mendoza-Santiesteban, C. E., & Plant, G. T. (2010). Optical coherence tomography of the retina: Applications in neurology. *Current Opinion in Neurology*, *23*(1), 16–23. https://doi.org/10.1097/WCO.0b013e328334e99b

Kesler, A., Vakhapova, V., Korczyn, A. D., Naftaliev, E., & Neudorfer, M. (2011). Retinal thickness in patients with mild cognitive impairment and Alzheimer's disease. *Clinical Neurology and Neurosurgery*, *113*(7), 523–526. https://doi.org/10.1016/j.clineuro.2011.02.014

Khan, T. K., & Alkon, D. L. (2015). Alzheimer's Disease Cerebrospinal Fluid and Neuroimaging Biomarkers: Diagnostic Accuracy and Relationship to Drug Efficacy. *Journal of Alzheimer's Disease: JAD*, *46*(4), 817–836. https://doi.org/10.3233/JAD-150238

Kirbas, S., Turkyilmaz, K., Anlar, O., Tufekci, A., & Durmus, M. (2013). Retinal Nerve Fiber Layer Thickness in Patients With Alzheimer Disease: *Journal of Neuro-Ophthalmology*, *33*(1), 58–61. https://doi.org/10.1097/WNO.0b013e318267fd5f

Kitaoka, T., Hara, Y., Matsumoto, M., & Tsuiki, E. (2017). 3D Heads-up vitreo-retinal surgery with intraoperative OCT and intraocular endoscopy. *Investigative Ophthalmology & Visual Science, 58*(8).

Kolb, H. (2003a). How the Retina Works. *American Scientist*, *91*(1), 28. https://doi.org/10.1511/2003.1.28

Kolb, H. (2003b). How the Retina Works. *American Scientist*, *91*(1), 28. https://doi.org/10.1511/2003.1.28

Koprowski, R., Teper, S. J., Węglarz, B., Wylęgała, E., Krejca, M., & Wróbel, Z. (2012). Fully automatic algorithm for the analysis of vessels in the angiographic image of the eye fundus. *Biomedical Engineering Online, 11*, 35. https://doi.org/10.1186/1475-925X-11-35

Koronyo, Y., Biggs, D., Barron, E., Boyer, D. S., Pearlman, J. A., Au, W. J., … Koronyo-Hamaoui, M. (2017). Retinal amyloid pathology and proof-of-concept imaging trial in Alzheimer's disease. *JCI Insight*, *2*(16), e93621. https://doi.org/10.1172/jci.insight.93621

Koronyo-Hamaoui, M., Koronyo, Y., Ljubimov, A. V., Miller, C. A., Ko, M. K., Black, K. L., … Farkas, D. L. (2011). Identification of amyloid plaques in retinas from Alzheimer's patients and noninvasive in vivo optical imaging of retinal plaques in a mouse model. *NeuroImage*, *54*, S204–S217. https://doi.org/10.1016/j.neuroimage.2010.06.020

Kotliar, K. E., Lanzl, I. M., Schmidt-Trucksäss, A., Sitnikova, D., Ali, M., Blume, K., … Hanssen, H. (2011). Dynamic retinal vessel response to flicker in obesity: A methodological

approach. *Microvascular Research*, *81*(1), 123–128. https://doi.org/10.1016/j.mvr.2010.11.007

Kovarnik, T., Chen, Z., Wahle, A., Skalicka, H., Kral, A., Lee, K., … Linhart, A. (2016). IS RETINAL LAYER THICKNESS RELATED TO CORONARY ATHEROSCLEROSIS? A STUDY WITH RETINAL OPTICAL COHERENCE TOMOGRAPHY AND CORONARY INTRAVASCULAR ULTRASOUND-VH. *Journal of the American College of Cardiology*, *67*(13), 359. https://doi.org/10.1016/S0735-1097(16)30360-6

Liew, G., Mitchell, P., Rochtchina, E., Wong, T. Y., Hsu, W., Lee, M. L., … Wang, J. J. (2011). Fractal analysis of retinal microvasculature and coronary heart disease mortality. *European Heart Journal*, *32*(4), 422–429. https://doi.org/10.1093/eurheartj/ehq431

Liew, G., & Wang, J. J. (2011). [Retinal vascular signs: A window to the heart?]. *Revista Espanola De Cardiologia*, *64*(6), 515–521. https://doi.org/10.1016/j.recesp.2011.02.014

Lin, G.-C., Wang, W.-J., Wang, C.-M., & Sun, S.-Y. (2010). Automated classification of multi-spectral MR images using Linear Discriminant Analysis. *Computerized Medical Imaging and Graphics: The Official Journal of the Computerized Medical Imaging Society*, *34*(4), 251–268. https://doi.org/10.1016/j.compmedimag.2009.11.001

Liu, B., Rasool, S., Yang, Z., Glabe, C. G., Schreiber, S. S., Ge, J., & Tan, Z. (2009). Amyloid-Peptide Vaccinations Reduce β-Amyloid Plaques but Exacerbate Vascular Deposition and Inflammation in the Retina of Alzheimer's Transgenic Mice. *The American Journal of Pathology*, *175*(5), 2099–2110. https://doi.org/10.2353/ajpath.2009.090159

Liu, G., Xu, D., & Wang, F. (2018). New insights into diabetic retinopathy by OCT angiography. *Diabetes Research and Clinical Practice*, *142*, 243–253. https://doi.org/10.1016/j.diabres.2018.05.043

London, A., Benhar, I., & Schwartz, M. (2013). The retina as a window to the brain-from eye research to CNS disorders. *Nature Reviews. Neurology*, *9*(1), 44–53. https://doi.org/10.1038/nrneurol.2012.227

Lorenz, M. W., Markus, H. S., Bots, M. L., Rosvall, M., & Sitzer, M. (2007). Prediction of clinical cardiovascular events with carotid intima-media thickness: A systematic review and meta-analysis. *Circulation*, *115*(4), 459–467. https://doi.org/10.1161/CIRCULATIONAHA.106.628875

Mandecka, A., Dawczynski, J., Blum, M., Müller, N., Kloos, C., Wolf, G., … Müller, U. A. (2007). Influence of flickering light on the retinal vessels in diabetic patients. *Diabetes Care*, *30*(12), 3048–3052. https://doi.org/10.2337/dc07-0927

Mantel, I. (2017). OCT in age related macular degeneration. *Acta Ophthalmologica*, *95*(S259). https://doi.org/10.1111/j.1755-3768.2017.03135

McGeechan, K., Liew, G., Macaskill, P., Irwig, L., Klein, R., Klein, B. E. K., … Wong, T. Y. (2009). Prediction of Incident Stroke Events Based on Retinal Vessel Caliber: A Systematic Review and Individual-Participant Meta-Analysis. *American Journal of Epidemiology*, *170*(11), 1323–1332. https://doi.org/10.1093/aje/kwp306

McKhann, G. M., Knopman, D. S., Chertkow, H., Hyman, B. T., Jack, C. R., Kawas, C. H., … Phelps, C. H. (2011). The diagnosis of dementia due to Alzheimer's disease: Recommendations from the National Institute on Aging-Alzheimer's Association

workgroups on diagnostic guidelines for Alzheimer's disease. *Alzheimer's & Dementia: The Journal of the Alzheimer's Association*, *7*(3), 263–269. https://doi.org/10.1016/j.jalz.2011.03.005

Mitchell, G. F., Hwang, S.-J., Vasan, R. S., Larson, M. G., Pencina, M. J., Hamburg, N. M., … Benjamin, E. J. (2010). Arterial stiffness and cardiovascular events: The Framingham Heart Study. *Circulation*, *121*(4), 505–511. https://doi.org/10.1161/CIRCULATIONAHA.109.886655

Mookiah, M. R. K., Acharya, U. R., Fujita, H., Tan, J. H., Chua, C. K., Bhandary, S. V., … Tong, L. (2015). Application of different imaging modalities for diagnosis of Diabetic Macular Edema: A review. *Computers in Biology and Medicine*, *66*, 295–315. https://doi.org/10.1016/j.compbiomed.2015.09.012

More, S. S., Beach, J. M., & Vince, R. (2016). Early Detection of Amyloidopathy in Alzheimer's Mice by Hyperspectral Endoscopy. *Investigative Ophthalmology & Visual Science*, *57*(7), 3231–3238. https://doi.org/10.1167/iovs.15-17406

More, S. S., & Vince, R. (2015). Hyperspectral Imaging Signatures Detect Amyloidopathy in Alzheimer's Mouse Retina Well before Onset of Cognitive Decline. *ACS Chemical Neuroscience*, *6*(2), 306–315. https://doi.org/10.1021/cn500242z

Nambi, V., Chambless, L., He, M., Folsom, A. R., Mosley, T., Boerwinkle, E., & Ballantyne, C. M. (2012). Common carotid artery intima-media thickness is as good as carotid intima-media thickness of all carotid artery segments in improving prediction of coronary heart disease risk in the Atherosclerosis Risk in Communities (ARIC) study. *European Heart Journal*, *33*(2), 183–190. https://doi.org/10.1093/eurheartj/ehr192

Niu, L., Zhang, Y., Meng, L., Xiao, Y., Wong, K. K. L., Abbott, D., … Qian, M. (2014). Detection of Subclinical Atherosclerosis in Asymptomatic Subjects Using Ultrasound Radiofrequency-Tracking Technology. *PLoS ONE*, *9*(11). https://doi.org/10.1371/journal.pone.0111926

Optina Diagnostics. (n.d.). Retrieved April 3, 2019, from http://optinadx.com/

Owen, C. G., Rudnicka, A. R., Mullen, R., Barman, S. A., Monekosso, D., Whincup, P. H., … Paterson, C. (2009). Measuring retinal vessel tortuosity in 10-year-old children: Validation of the Computer-Assisted Image Analysis of the Retina (CAIAR) program. *Investigative Ophthalmology & Visual Science*, *50*(5), 2004–2010. https://doi.org/10.1167/iovs.08-3018

Paquet, C., Boissonnot, M., Roger, F., Dighiero, P., Gil, R., & Hugon, J. (2007). Abnormal retinal thickness in patients with mild cognitive impairment and Alzheimer's disease. *Neuroscience Letters*, *420*(2), 97–99. https://doi.org/10.1016/j.neulet.2007.02.090

Parisi, V., Restuccia, R., Fattapposta, F., Mina, C., Bucci, M. G., & Pierelli, F. (2001). Morphological and functional retinal impairment in Alzheimer's disease patients. *Clinical Neurophysiology*, *112*(10), 1860–1867. https://doi.org/10.1016/S1388-2457(01)00620-4

Patasius, M., Marozas, V., Jegelevicius, D., & Lukosevicius, A. (2005). Evaluation of tortuosity of eye blood vessels using the integral of square of derivative of curvature. *IFMBE Proc. 3rd Eur. Med. Biol. Eng. Conf.(EMBEC05), 11*.

Patton, N., Aslam, T., Macgillivray, T., Pattie, A., Deary, I. J., & Dhillon, B. (2005). Retinal vascular image analysis as a potential screening tool for cerebrovascular disease: A rationale based on homology between cerebral and retinal microvasculatures. *Journal of Anatomy*, *206*(4), 319–348. https://doi.org/10.1111/j.1469-7580.2005.00395.x

Patton, N., Pattie, A., MacGillivray, T., Aslam, T., Dhillon, B., Gow, A., … Deary, I. J. (2007). The Association between Retinal Vascular Network Geometry and Cognitive Ability in an Elderly Population. *Investigative Opthalmology & Visual Science*, *48*(5), 1995. https://doi.org/10.1167/iovs.06-1123

Peña, A. S., Liew, G., Anderson, J., Giles, L. C., Gent, R., Wong, T. Y., & Couper, J. J. (2018). Early atherosclerosis is associated with retinal microvascular changes in adolescents with type 1 diabetes. *Pediatric Diabetes*, *19*(8), 1467–1470. https://doi.org/10.1111/pedi.12764

Peng, J., & Luo, T. (2016). Sparse matrix transform-based linear discriminant analysis for hyperspectral image classification. *Signal, Image and Video Processing*, *10*(4), 761–768. https://doi.org/10.1007/s11760-015-0808-y

Publishing, H. H. (n.d.). Atherosclerosis. Retrieved April 3, 2019, from Harvard Health website: https://www.health.harvard.edu/a_to_z/atherosclerosis-a-to-z

Querques, G., Borrelli, E., Sacconi, R., De Vitis, L., Leocani, L., Santangelo, R., … Bandello, F. (2019). Functional and morphological changes of the retinal vessels in Alzheimer's disease and mild cognitive impairment. *Scientific Reports*, *9*(1). https://doi.org/10.1038/s41598-018-37271-6

Ratnayaka, J. A., Serpell, L. C., & Lotery, A. J. (2015). Dementia of the eye: The role of amyloid beta in retinal degeneration. *Eye (London, England)*, *29*(8), 1013–1026. https://doi.org/10.1038/eye.2015.100

Reimann, M., Prieur, S., Lippold, B., Bornstein, S. R., Reichmann, H., Julius, U., & Ziemssen, T. (2009). Retinal vessel analysis in hypercholesterolemic patients before and after LDL

apheresis. *Atherosclerosis. Supplements*, *10*(5), 39–43. https://doi.org/10.1016/S1567-5688(09)71808-2

Ren, L., Cai, J., Liang, J., Li, W., & Sun, Z. (2015). Impact of Cardiovascular Risk Factors on Carotid Intima-Media Thickness and Degree of Severity: A Cross-Sectional Study. *PLOS ONE*, *10*(12), e0144182. https://doi.org/10.1371/journal.pone.0144182

Ritt Martin, & Schmieder Roland E. (2009). Wall-to-Lumen Ratio of Retinal Arterioles as a Tool to Assess Vascular Changes. *Hypertension*, *54*(2), 384–387. https://doi.org/10.1161/HYPERTENSIONAHA.109.133025

Rückstieß, T., Osendorfer, C., & van der Smagt, P. (2011). Sequential Feature Selection for Classification. In D. Wang & M. Reynolds (Eds.), *AI 2011: Advances in Artificial Intelligence* (pp. 132–141). Springer Berlin Heidelberg.

Sabri, O., Seibyl, J., Rowe, C., & Barthel, H. (2015). Beta-amyloid imaging with florbetaben. *Clinical and Translational Imaging*, *3*(1), 13–26. https://doi.org/10.1007/s40336-015-0102-6

Seidelmann, S. B., Claggett, B., Bravo, P. E., Gupta, A., Farhad, H., Klein, B. E., … Solomon, S. D. (2016). Retinal Vessel Calibers in Predicting Long-Term Cardiovascular Outcomes: The Atherosclerosis Risk in Communities Study. *Circulation*, *134*(18), 1328–1338. https://doi.org/10.1161/CIRCULATIONAHA.116.023425

Sharrett, A. R., Hubbard, L. D., Cooper, L. S., Sorlie, P. D., Brothers, R. J., Nieto, F. J., … Klein, R. (1999). Retinal Arteriolar Diameters and Elevated Blood Pressure: The Atherosclerosis Risk in Communities Study. *American Journal of Epidemiology*, *150*(3), 263–270. https://doi.org/10.1093/oxfordjournals.aje.a009997

Ţălu, Ş. (2013). *Characterization of retinal vessel networks in human retinal imagery using quantitative descriptors*. *5*(2), 6.

Tedeschi-Reiner, E., Strozzi, M., Skoric, B., & Reiner, Z. (2005a). Relation of Atherosclerotic Changes in Retinal Arteries to the Extent of Coronary Artery Disease. *The American Journal of Cardiology*, *96*(8), 1107–1109. https://doi.org/10.1016/j.amjcard.2005.05.070

Tedeschi-Reiner, E., Strozzi, M., Skoric, B., & Reiner, Z. (2005b). Relation of Atherosclerotic Changes in Retinal Arteries to the Extent of Coronary Artery Disease. *The American Journal of Cardiology*, *96*(8), 1107–1109. https://doi.org/10.1016/j.amjcard.2005.05.070

The Atherosclerosis Risk in Communities (ARIC) Study: Design and objectives. The ARIC investigators. (1989). *American Journal of Epidemiology*, *129*(4), 687–702.

Vaudaux, J. (2017). OCT in retinal and choroidal inflammatory disease. *Acta Ophthalmologica*, *95*(S259). https://doi.org/10.1111/j.1755-3768.2017.03136

Wang, L., Wong, T. Y., Sharrett, A. R., Klein, R., Folsom, A. R., & Jerosch-Herold, M. (2008). Relationship between retinal arteriolar narrowing and myocardial perfusion: Multi-ethnic study of atherosclerosis. *Hypertension (Dallas, Tex.: 1979)*, *51*(1), 119–126. https://doi.org/10.1161/HYPERTENSIONAHA.107.098343

Williams, M. A., McGowan, A. J., Cardwell, C. R., Cheung, C. Y., Craig, D., Passmore, P., … McKay, G. J. (2015). Retinal microvascular network attenuation in Alzheimer's disease. *Alzheimer's & Dementia: Diagnosis, Assessment & Disease Monitoring*, *1*(2), 229–235. https://doi.org/10.1016/j.dadm.2015.04.001

Wong, T., & Mitchell, P. (2007). The eye in hypertension. *The Lancet*, *369*(9559), 425–435. https://doi.org/10.1016/S0140-6736(07)60198-6

Wong, T. Y., Cheung, N., Islam, F. M. A., Klein, R., Criqui, M. H., Cotch, M. F., … Sharrett, A. R. (2007). Relation of Retinopathy to Coronary Artery Calcification: The Multi-Ethnic Study of Atherosclerosis. *American Journal of Epidemiology*, *167*(1), 51–58. https://doi.org/10.1093/aje/kwm256

Yang, J. Y., Yang, X., Li, Y., Xu, J., Zhou, Y., Wang, A. X., … Jonas, J. B. (2016). Carotid Atherosclerosis, Cerebrospinal Fluid Pressure, and Retinal Vessel Diameters: The Asymptomatic Polyvascular Abnormalities in Community Study. *PLOS ONE*, *11*(12), e0166993. https://doi.org/10.1371/journal.pone.0166993

APPENDIX A

A.1 Investigation of the retinal image features against cognitive status

In addition to cerebral amyloid status, we also investigated the features' differences between cognitively impaired patients (CI) and cognitively unimpaired subjects (CU). Figure A.1 shows the differences corresponding to features F1 to F7 listed in table 4.1 when cognitive test results were used as gold standard. One can observe that differences associated with venule tortuosity (a) and three texture measures (b, c, and d) remained significant. When compared to Figure 4.3 (comparisons using amyloid status as gold standard), feature F7 (A.1-d) shows a smaller p-value.

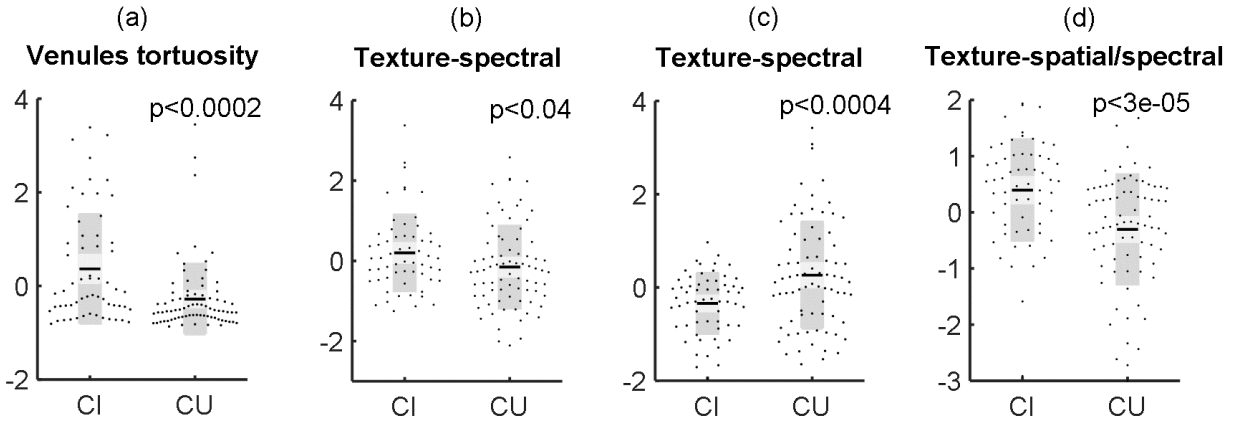

Figure A.1 Difference between cognitively impaired (CI) and cognitively unimpaired (CU) subjects corresponding to retinal image features: (a) tortuosity of venules , (b) texture-contrast of arterioles and around tissue at 450-550nm along spectral direction, (c) texture-energy of arterioles and around tissue at 450-550nm along spectral direction, and (d) texture-correlation of arterioles and around tissue at 450-550nm along spatial/spectral direction). Data points are shown as normalized values over both groups.

A.2 Results of using spatial textures in atherosclerosis study

As mentioned in Section 6.2, using a combination of spatial (instead of spatial/spectral) and spectral texture measures we could discriminate ATH from CTL subjects with an accuracy of 0.9 using a quadratic classifier. Features selected, cross validation losses and representation of data points in a 2D plane associated with this approach are given in Table A.2 and Figure A.2. The rational used for feature selection is the same as explained in Section 3.2.5 and Algorithm 3.1.

Table A.1 Vasculature and texture features including spatial and spectral texture measures

Feature code	Feature name	Feature Type	Anatomical region	Band(nm)	Direction
F1	diameter	Vasculature	arterioles – zone B	-	-
F2	diameter	"	arterioles – zone C	-	-
F3	Correlation	Texture	venules and adjacent regions	450-550	spatial
F4	Energy	"	venules and adjacent regions	450-550	spatial
F5	Energy	"	venules and adjacent regions	450-550	spectral
F6	Correlation	"	venules	700-900	spectral
F7	Correlation	"	arterioles	700-900	spatial
F8	Correlation	"	venules	450-550	spectral

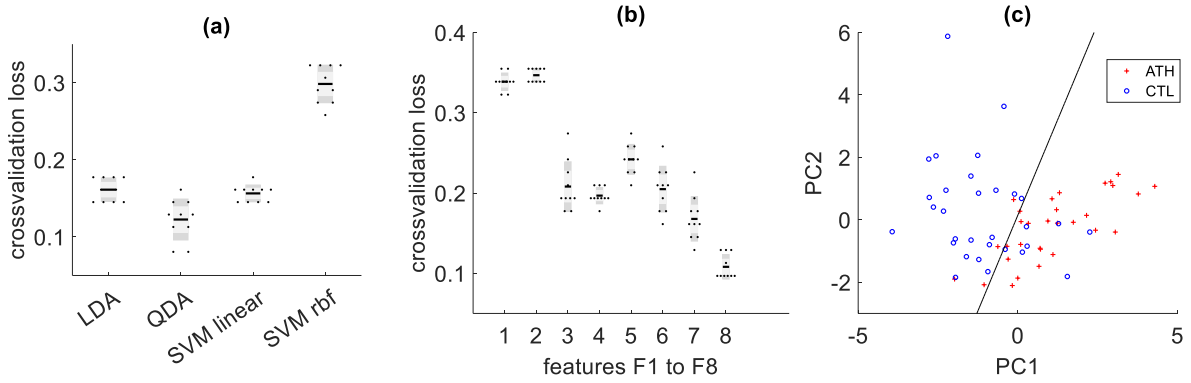

Figure A.2 (a) Classification loss of four classifiers using features F1 to F8; (b) QDA classification loss using features F1 to F8 inclusively (c) data points in a 2D plane projection using PC1 and PC2 of the selected features.